Universidad de Cantabria

Departamento de Física Moderna

CSIC - Universidad de Cantabria

Instituto de Física de Cantabria

Evidencia estadística de una no-Gaussianidad local en los Datos de WMAP

Memoria presentada por el Licenciado

Marcos Cruz Rodríguez

para optar al título de Doctor en Ciencias Físicas

2007

Enrique Martínez-González, Doctor en Ciencias Físicas y
Profesor de Investigación del Consejo Superior de Investigaciones Científicas,

y

Patricio Vielva Martínez, Doctor en Ciencias Físicas y
Contratado I3P del Consejo Superior de Investigaciones Científicas,

CERTIFICAN que la presente memoria

Evidencia estadística de una no-Gaussianidad local en los Datos de WMAP

ha sido realizada por **Marcos Cruz Rodríguez** bajo nuestra dirección.
Consideramos que esta memoria contiene aportaciones suficientes para construir la tesis Doctoral del interesado

En Santander, a 27 de Julio de 2007

Enrique Martínez-González Patricio Vielva Martínez

A mi abuelos,
a mis padres
y
a Aude

Agradecimientos

Hay una larga lista de personas a las que agradecer su apoyo para hacer posible este trabajo. Seguramente hay que empezar por mis padres ya que en primer lugar sin ellos no estaría aquí, y además siempre tuvieron el empeño en hacerme entender la importancia de la ciencia y en entrenarme para poder ser un buen estudiante. Ya desde muy corta edad mi padre me enseñaba a resolver ecuaciones sencillas o pegaba las tablas de multiplicar en los corn-flakes y mi madre me ayudaba con los deberes y me animaba con gran insistencia a estudiar. Si en vez de hacer esto me hubieran enseñado a dar patadas o tirado balones a la cabeza quizá ahora fuese un adinerado futbolista aunque casi prefiero que no haya sido así. Siguiendo con la familia le toca el turno a mis abuelos, tanto Engracia y José que siguen con interés mis últimas publicaciones, como Marina y Manolo que también me han animado siempre a estudiar. Aunque la conozco desde hace menos tiempo que a mis padres, también agradezco el apoyo de Aude durante los 4 años que he dedicado a esta tesis.

En cuanto al trabajo específico que desarrollo en esta tesis tengo que agradecer a mis directores de tesis, Enrique Martínez y Patricio Vielva, el esfuerzo y tiempo que han dedicado con mucho acierto. Gracias a ellos ha sido posible escribir esta tesis. Entre los dos se han complementado a la perfección para atender dudas de cualquier tipo, motivarme y ayudarme. A ellos hay que añadir excelentes colaboradores como Laura Cayón y Marco Tucci, así como Mike Hobson y Neil Turok que aunque estén muy ocupados han sido claves en el último artículo de esta tesis. Aunque no aparezcan en la lista de autores también han sido de gran ayuda mis compañeros de despacho Andrés, Carlos, Jacobo y Marcos; y los demás miembros del grupo como Belén, Chema, Diego, José Luis, ... es muy importante poder trabajar con buen ambiente.

Universidad de Cantabria

Departamento de Física Moderna

CSIC - Universidad de Cantabria

Instituto de Física de Cantabria

Statistical evidence of a local non-Gaussianity in the WMAP Data

A dissertation submited for the conferment of

the degree of Doctor of Philosophy in Physics by

Marcos Cruz Rodríguez

2007

Prologue

In this thesis the Gaussianity of the Cosmic Microwave Background (CMB) anisotropies is analysed. As explained in the introduction, the CMB is the most ancient image of the Universe and therefore it is a very useful tool to extend our knowledge about the early Universe. The tiny anisotropies present in the CMB give us information about the geometry, content and age of the Universe. The Gaussianity of these anisotropies is a key issue to discriminate between different cosmological models. The most precise all-sky experiment measuring the CMB anisotropies is the Wilkinson Microwave Anisotropy Probe (WMAP) satellite launched by the NASA in 2001. We analyse the WMAP data with a technique based on wavelets on the sphere. A blind, not model dependent approach is chosen and hence the main difficulty is in identifying the source of the non-Gaussianity.

The thesis is organised as follows. We start with an introduction explaining general issues related with the CMB, its anisotropies and the importance of studying the Gaussianity. In Chapter 2 the detection of a non-Gaussian spot in the 1-year data of the WMAP data is reported. The significance, morphology and foreground contribution of this spot are discussed in Chapter 3. The redetection of the spot in the 3-year WMAP data is presented in Chapter 4, and the possible interpretation of this spot as a topological defect, such as a texture is considered in Chapter 5. The general conclusions of all these chapters are presented in Chapter 6. At the end of the thesis, a summary in Spanish language is included.

Contents

List of Figures

List of Tables

CHAPTER 1

Introduction

1.1 The Cosmic Microwave Background Radiation

The Cosmic Microwave Background (CMB) is the most ancient electromagnetic radiation that can be observed. Therefore it is an unique tool for studying the early Universe and is considered as the best evidence for the Big Bang model of the Universe. The theory of the Big Bang was formulated by George Gamow and collaborators in 1948 [5]. According to this theory the Universe could have formed thousands of millions of years ago starting from a tremendously dense and hot state. The theory explains the production of nuclei (primordial nucleosynthesis), the abundance of light elements and the expansion of the Universe which had been observed by E. Hubble in 1929 [94]. In addition an isotropic background radiation of the order of 5 Kelvin was predicted. It would represent a relic radiation of the hot early Universe which cooled from around $3,000$K down to about 5K due to the expansion of the Universe. At the time this prediction was formulated this radiation had not been detected yet! More than a decade later, in 1965, Penzias and Wilson [145] detected the CMB radiation accidentally and R. Dicke, P.J.E. Peebles, P.G. Roll, & D.T. Wilkinson [53] interpreted this radiation as a signature of the Big Bang.

Since then, a large number of experiments have been built to measure the CMB radiation. The first satellite mission dedicated to it, the Cosmic Background Explorer (COBE), was launched in 1989. Two of their principal investigators, G. S. Smoot (Differential Microwave Radiometer, DMR) and J. Mather (Far Infrared Absolute Spectrophotometer, FIRAS), received the Nobel Prize in Physics in 2006. The COBE-FIRAS experiment showed that the CMB had an almost perfect black-body spectrum [125] corresponding to a temperature of $T_0 = 2.725$K.

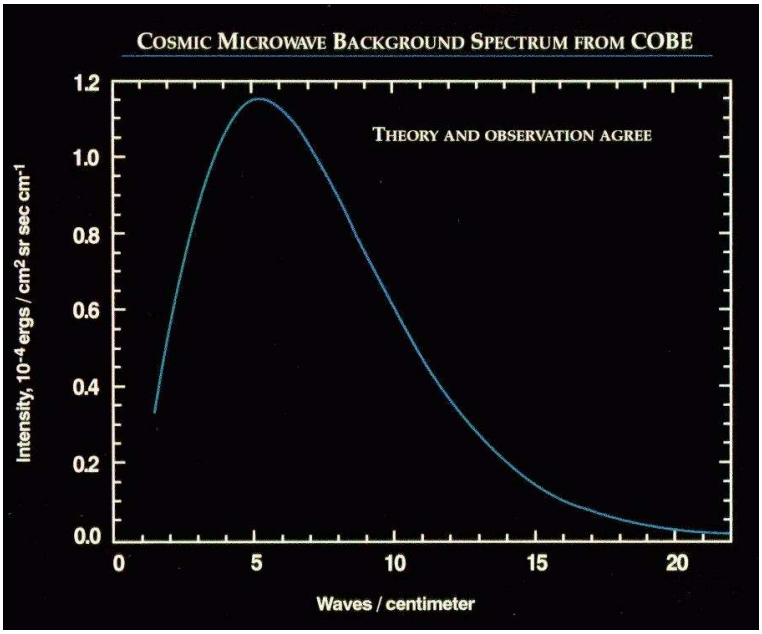

Figure 1.1 CMB black-body spectrum as measured by FIRAS.

COBE-DMR [167] measured the CMB radiation in all the sky. Subtracting the average temperature, T_0, and a dipole component due to our local movement from the COBE-DMR map, small temperature anisotropies of order $\Delta T/T_0 \sim 10^{-5}$ were measured (see Figures 1.1 and 1.2)[1]. One of the greatest successes of the Big Bang theory is the prediction of these findings. The early Universe is the ideal source of purely thermal radiation needed for observing a perfect black-body spectrum, and Harrison [85], Peebles & Yu [143], and Zel'dovich [195] had realized that the early Universe would have to have inhomogeneities at the level of 10^{-5} or 10^{-4}.

During the 1990's, the anisotropies were measured with increasing sensitivity by ground and balloon based experiments. By 2000 the BOOMERanG [48] and MAXIMA [79] balloon experiments reported that the highest angular power fluctuations occur at scales of approximately one degree. Together with other cosmological data, these results implied that the geometry of the Universe is flat. Over the next three years a number of ground-based interferometers provided measurements of the CMB anisotropies with higher accuracy, including for instance the Very Small Array (VSA) [71], Cosmic Background Imager (CBI) [163], Archeops [19], Arcminute Cosmology Bolometer Array Receiver

[1] http://lambda.gsfc.nasa.gov

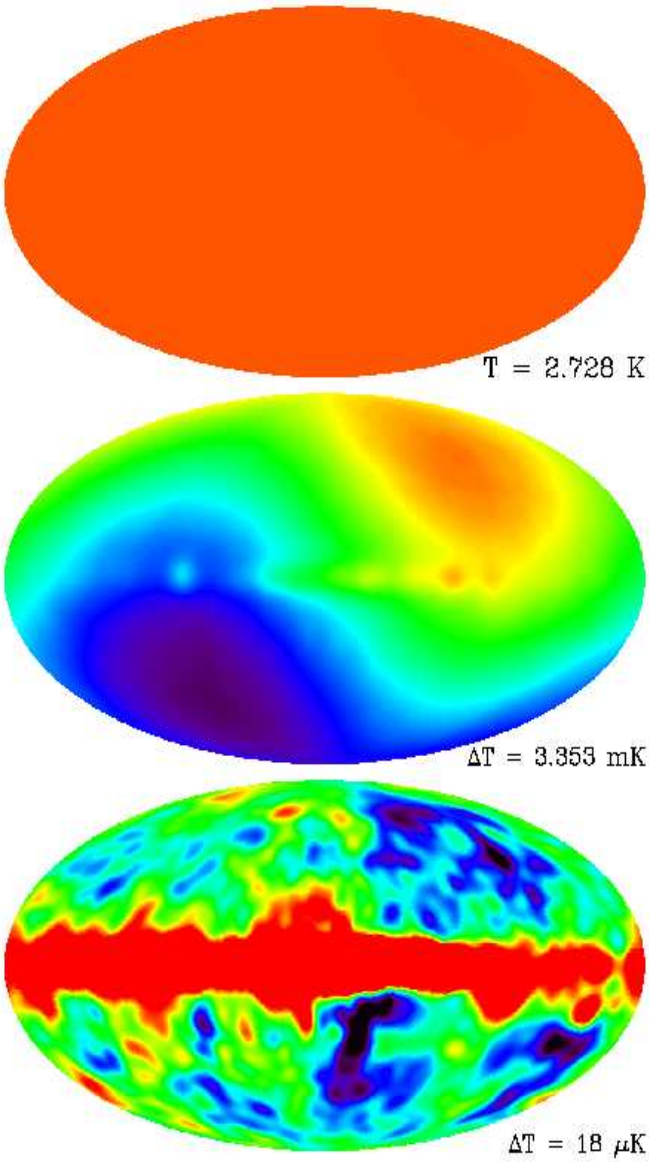

Figure 1.2 COBE-DMR data (top) on a scale from 0 - 4 K, showing the near-uniformity of the CMB brightness, (middle) on a scale intended to enhance the contrast due to the dipole due to our local movement, and (bottom) anisotropies after subtraction of the monopole and the dipole components. From the Legacy Archive for Microwave BAckground Data Analysis (LAMBDA) web site.

(ACBAR) [106], and Degree Angular Scale Interferometer (DASI) [78], which made the first detection of the polarization of the CMB.

Recently the NASA satellite mission, Wilkinson Microwave Anisotropy Probe, (WMAP) [17] measured with unprecedented accuracy the CMB anisotropies in all the sky. The detailed analysis of these anisotropies can be used to estimate the cosmological parameters which describe the age, geometry and composition of the Universe. The standard Λ-Cold Dark Matter (ΛCDM) model of the Big Bang provides the best fit to the WMAP data [171]. Large scale structure and supernovae observations also support this model, therefore it is frequently referred to as the concordance model. It assumes a Universe without spatial curvature and with an accelerated expansion, driven by the cosmological constant, Λ. The nature of this constant is unknown and therefore it is called *dark energy*. According to supernovae and CMB observations, dark energy represents around 74% of the energy density of the present Universe. Most of the remaining energy density, about 22%, is due to *Cold Dark Matter* (CDM), which is non-baryonic, not thermalized matter. It is of unknown composition and does neither emit nor reflect electromagnetic radiation. Although it has not been observed directly, its existence has been proven by gravitational effects. Only the remaining 4% of the energy density is due to ordinary baryonic matter.

However the early Universe was considerably different. Extrapolating the expansion backwards in time yields infinite density and temperature 14 thousand million years ago. This singularity at which the physical laws break down is called Big Bang. From that moment to approximately 10^{-43} seconds (one Planck time) after, the quantum effects of gravity were significant and the physics at this epoch are unclear and poorly understood. From the first second after the Big Bang until now, the physics are rather well known. The Universe was homogeneously and isotropically filled with radiation and matter. The temperature, density and pressure were enormously high, forcing the Universe to expand very rapidly. The expansion causes a cooling of the Universe. Some theories affirm [74], [9] that 10^{-35} seconds after the Big Bang a phase transition caused an exponential expansion called *inflation*. This would make the Universe to appear flat, homogeneous and isotropic at the largest observable scales. Moreover, the expansion amplified the tiny quantum fluctuations of the Universe which seed the formation of structure in the later Universe.

At the end of inflation, the Universe consisted of a quark-gluon plasma. As the

Universe continued to expand, the cooling allowed the formation of baryons.

However, atoms could not form until many years later. Radiation and matter were constantly interacting so that atoms could not form and photons could not escape. When the Universe cooled down to 3000K, 375,000 years after the Big Bang, the interaction rate was low enough to allow atom formation and photons could escape. Photons were scattered at all points and in all directions. These are the CMB photons measured today after traveling through the Universe for almost 14 thousand million years.

The density fluctuations at decoupling were imprinted in the CMB. Standard inflation predicts these fluctuations to represent a Gaussian and Isotropic random field (see Liddle & Lyth [114] for a detailed description), whereas non-standard inflation (see [13] for a review) or topological defect models [191] predict non-Gaussian features in the CMB.

Therefore studying the Gaussianity of the CMB anisotropies allows to discriminate between different cosmological models.

The PLANCK satellite which will be launched in 2008 by the ESA, will measure the CMB on smaller scales than WMAP and its increased sensitivity will provide more accurate polarization data. The wide frequency range (30 to 857 GHz) will allow to better separate the contaminant signals (see section 1.4). The PLANCK data are expected to confirm the above described scenario or perhaps open new possibilities.

1.2 Anisotropies of the CMB

As the early Universe was very homogeneous and isotropic, photons with the same energy were scattered in all directions. Hence we measure the same average CMB radiation in any direction of a sphere representing the observable sky. The photons we receive were emitted almost 14 thousand million years ago at the *Last Scattering Surface*. The density fluctuations present at that epoch are imprinted in the CMB producing small anisotropies.

The CMB anisotropies projected on the unit sphere can be seen as a function of the spherical coordinates θ and ϕ, and therefore they can be expressed as a sum

of spherical harmonics ($Y_{\ell m}(\theta,\phi)$) with coefficients $a_{\ell m}$:

$$\frac{\Delta T}{T}(\theta,\phi) = \frac{T(\theta,\phi) - T_0}{T_0} = \sum_{\ell=1}^{\infty} \sum_{m=-\ell}^{\ell} a_{\ell m} Y_{\ell m}(\theta,\phi). \tag{1.2.1}$$

Assuming the standard inflationary prediction, the anisotropies represent a Gaussian and isotropic random field. In this case the statistical properties are described by the two point correlation function:

$$C(\bar{\theta}) = \left\langle \frac{\Delta T}{T}(\vec{\Omega}_1) \frac{\Delta T}{T}(\vec{\Omega}_2) \right\rangle = \sum_{\ell m} \sum_{\ell' m'} \langle a_{\ell m} a^*_{\ell' m'} \rangle Y_{\ell m}(\theta_1,\phi_1) Y_{\ell' m'}(\theta_2,\phi_2), \tag{1.2.2}$$

where $\bar{\theta} = \cos^{-1}\left(\vec{\Omega}_1 \cdot \vec{\Omega}_2\right)$ and $\vec{\Omega}_1$ and $\vec{\Omega}_2$ denote two unit vectors pointing towards the two directions in the sky given by the coordinates (θ_1,ϕ_1) and (θ_2,ϕ_2). If the isotropy and homogeneity properties are verified, then the angular power spectrum C_ℓ can be written as

$$\langle a_{\ell m} a^*_{\ell' m'} \rangle = C_\ell \delta_{\ell \ell'} \delta_{m m'}, \tag{1.2.3}$$

where $\langle . \rangle$ denotes averaging over sufficiently large volumes.

The correlation function of the temperature fluctuations, $C(\bar{\theta})$, is related to the angular power spectrum C_ℓ through the Legendre transform

$$C(\bar{\theta}) = \sum_{\ell} \frac{2\ell+1}{4\pi} C_\ell P_\ell(\cos\bar{\theta}), \tag{1.2.4}$$

where P_ℓ are the Legendre polynomials of order ℓ. The angular power spectrum of a model can be calculated as a function of the cosmological parameters. The ΛCDM model provides the best fit to the WMAP data as can be seen in Figure 1.3.

There are different kinds of anisotropies depending on the moment when they were generated. They are usually divided into primary and secondary anisotropies:

- **Primary anisotropies**, are due to effects that occurred at the last scattering surface. The physics of the photon-baryon plasma determined the shape of the CMB angular power spectrum. The radiation pressure of the photons competing with the gravitational attraction of the baryons create acoustic oscillations which are responsible for the characteristic peak structure of the angular power spectrum. At large scales the Sachs-Wolfe

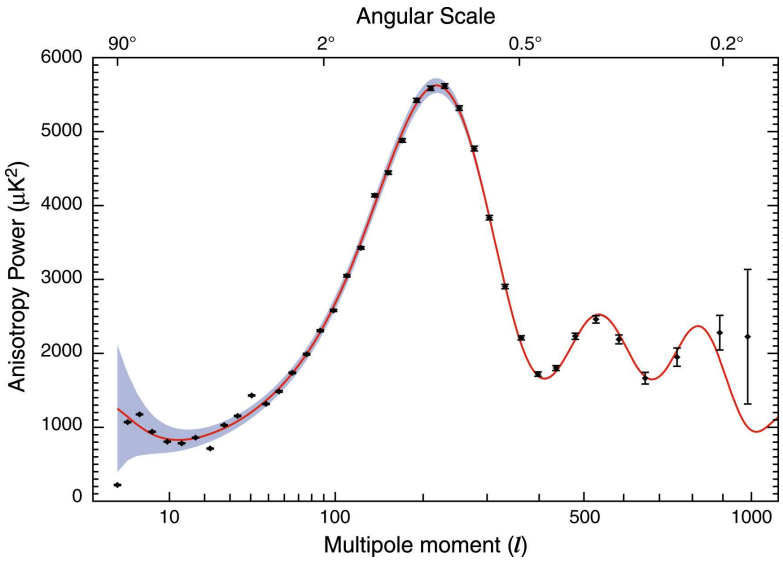

Figure 1.3 WMAP three-year binned angular power spectrum (in black) from $\ell = 2 - 1000$,[90]. The red line represents the best fit Λ-CDM model fit to the data and the band stands for the one sigma cosmic variance error. From the Legacy Archive for Microwave BAckground Data Analysis (LAMBDA) web site.

effect [151] due to variations in the gravitational potential dominates, whereas at small scales diffusion damping [164] and blurring effects due to the finite thickness of the last scattering surface prevail.

- **Secondary anisotropies**, are generated between the last scattering surface and the observer. They are due to interactions of the CMB photons with hot gas or gravitational potentials. Here the gravitational effect is called *Integrated Sachs-Wolfe* (ISW) effect. There are two kinds of ISW effect. The early ISW occurs shortly after photons leave the last scattering surface, and is due to the evolution of the potential wells as the Universe changes from being dominated by radiation to being dominated by matter. The late-time ISW arises much later, as the evolution starts to feel the effect of the cosmological constant. When the late-time ISW is due the non-linear evolution of a collapsing structure it is also called *Rees-Sciama* effect [149], [120].

  The *reionization* of the Universe after recombination produces free electrons that rescatter off the photons of the CMB radiation, producing secondary anisotropies. The first few generations of population III stars and quasars emitted radiation that reionized the Universe globally [72]. Local

reionization takes place in clusters of galaxies. Hot gas trapped in clusters contains high energy electrons which distort the (CMB) black-body spectrum through inverse Compton scattering [174]. This effect is called *thermal Sunyaev-Zeldovich* effect when the electrons have high energies due to their temperature and *kinematic Sunyaev-Zeldovich* effect if the high energies are due to their bulk motion.

Gravitational lensing of the CMB photons is a further effect that can produce secondary anisotropies [160], [121]. It is caused by massive superclusters that deviate the trajectory of the CMB photons.

1.2.1 Polarization

The CMB is polarized at the level of a few μK. There are two polarization modes, E-modes and B-modes. This is in analogy to electrostatics, in which the electric field (E-field) has a vanishing curl and the magnetic field (B-field) has a vanishing divergence. The E-modes arise from the Thomson scattering in an inhomogeneous plasma as the one present in the early Universe and hence they are correlated with the temperature anisotropies. The polarization of the CMB is a much weaker signal than the temperature anisotropies and thus it is more difficult to measure it accurately. The E mode and the TE correlation have been measured recently by DASI, [104] WMAP [138] and BOOMeranG [147]. Future experiments are focusing in more precise polarization measures. The primordial B-modes which have not been detected by now, are thought to have an amplitude of at most $0.1\mu K$ and are not produced from the plasma physics alone. They are a signal from cosmic inflation and are determined by the density of primordial gravitational waves. Detecting the B-modes will be extremely difficult, particularly given that the degree of foreground contamination is relatively much higher, and the weak gravitational lensing signal mixes the relatively strong E-mode signal with the B-mode signal.

1.3 WMAP data

The Wilkinson Microwave Anisotropy Probe (WMAP, [17]) is a NASA satellite mission. It was launched in 2001 and observes the sky from an orbit about the L2 Sun-Earth Lagrangian point, 1.5 million km from Earth. Its aim is to produce

$\Omega_m h^2$	$0.1277^{+0.0080}_{-0.0079}$
$10^2\Omega_b h^2$	2.229 ± 0.073
H_0	$73.2^{+0.031}_{-0.032}$ km/s/Mpc
σ_8	$0.761^{+0.049}_{-0.048}$
τ	0.089 ± 0.030
n_s	0.958 ± 0.016

Table 1.1 Cosmological parameters for the WMAP data, considering the Λ-CDM model.

a 13 arcminute FWHM resolution full sky map of the CMB anisotropies.

The WMAP radiometers, measure temperature differences at 5 frequency bands, namely K-band (22.8 GHz, 1 differencing assembly), Ka-Band (33.0 GHz, 1 differencing assembly), Q-Band (40.7 GHz, 2 differencing assemblies), V-Band (60.8 GHz, 2 differencing assemblies) and W-Band (93.5 GHz, 4 differencing assemblies).

The beam size ranges from 0.9 to 0.2 degrees and the sensitivity is around 1 mK $s^{1/2}$. The Hierarchical, Equal Area and iso-Latitude Pixelization (HEALPix, [73])[2], is used in all maps and the resolution parameter of this pixelization is called N_{side}.

The WMAP data give precise information about the content, age, evolution and geometry of the Universe [171]. A Λ-CDM model provides the best fit to the data with only six parameters: matter density, $\Omega_m h^2$, baryon density, $\Omega_b h^2$, Hubble constant, $H_0 \equiv 100h$ km/s/Mpc, amplitude of fluctuations, σ_8, optical depth, τ, and a slope for the scalar perturbation spectrum, n_s. The best fit values of these parameters are listed in Table 1.1.

The statistical analysis of the CMB maps can give us very valuable information which can not be deduced from the angular power spectrum. Testing the Gaussianity and the isotropy of the CMB and looking for cross-correlations between CMB and large scale structure are some of the analyses which can be performed on CMB maps. For these kind of cosmological analyses the WMAP team recommends the use of a combined map. It is a linear combination of the receivers

[2]http://www.eso.org/science/healpix/

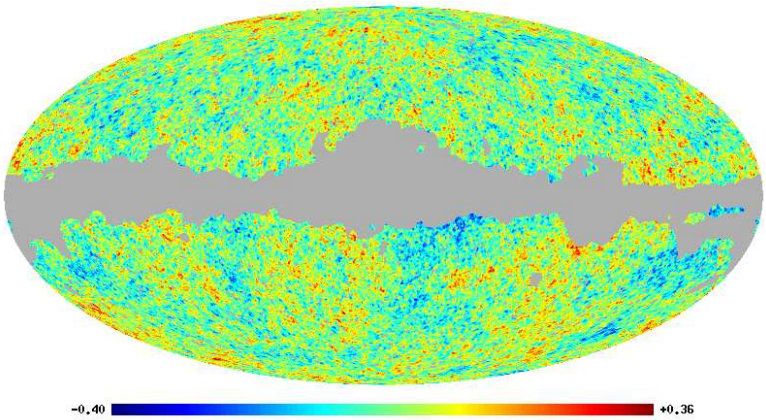

Figure 1.4 WMAP combined and foreground cleaned map.

where CMB is the dominant signal, namely Q, V, W radiometers:

$$T(\mathbf{x}) = \sum_{j=3}^{10} T_j(\mathbf{x})\, w_j(\mathbf{x}), \tag{1.3.1}$$

The Q-Band receivers are denoted with indices $j = 3, 4$, V-Band receivers with indices $j = 5, 6$, whereas indices $j = 7, 8, 9, 10$ correspond to the four W-Band receivers. Noise weights $w_j(\mathbf{x})$ are defined so that receivers with less noise have more weight:

$$w_j(\mathbf{x}) = \frac{\bar{w}_j(\mathbf{x})}{\sum_{j=3}^{10} \bar{w}_j(\mathbf{x})}, \qquad \bar{w}_j(\mathbf{x}) = \frac{N_j(\mathbf{x})}{{\sigma_{0_j}}^2} \tag{1.3.2}$$

where σ_{0j} is the noise dispersion per observation and $N_j(\mathbf{x})$ is the number of observations performed by the receiver j at position $\mathbf{x}$ (see [17]). The combined map, shown in Figure 1.4, increases the signal to noise ratio and does not use the K and Ka bands which are highly contaminated by Galactic radiation.

Unfortunately even at the Q, V and W bands, the CMB photons constitute not the only microwave signal we receive. In order to perform cosmological studies, the contaminating signals must be understood and removed from the CMB maps before combining them as explained above. There are several component separation techniques as presented in the following section. After removing the contaminating emissions which we describe below, the residual monopole and dipole have to be subtracted.

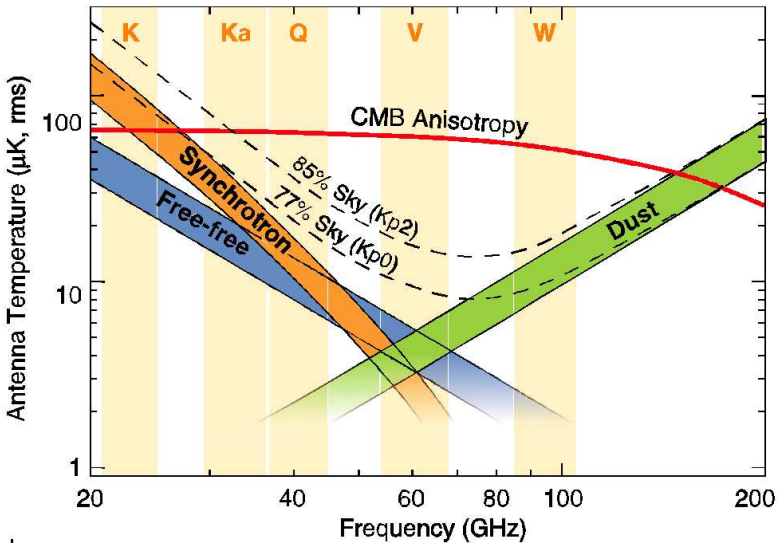

Figure 1.5 Foreground frequency dependence compared to CMB as calculated for WMAP [18]. From the Legacy Archive for Microwave BAckground Data Analysis (LAMBDA) web site.

1.4 Foregrounds

The CMB signal is contaminated by microwave emission from the Milky Way Galaxy and from extragalactic sources. These emissions are called *foregrounds*. They are usually expressed in antenna temperature T_A rather than thermodynamic temperature T which is used for the CMB. The relation between both temperatures is given by

$$\Delta T = \Delta T_A \frac{(e^x - 1)^2}{x^2 e^x}, \tag{1.4.1}$$

where $x = h\nu/kT_0$, h the Planck constant, ν the frequency and k Boltzmann's constant. The frequency dependence of the foregrounds in a certain range is usually expressed as $T_A \sim \nu^\beta$, where β is the spectral index. Figure 1.5[3] shows the frequency dependence of the Galactic foregrounds at WMAP frequencies compared to the CMB.

1.4.1 Synchrotron

Synchrotron emission arises from the acceleration of cosmic ray electrons in magnetic fields. Its signal is complex and the spectral index varies between

[3] http://lambda.gsfc.nasa.gov

$\beta_s \sim -2.6$ and $\beta_s \sim -3.1$ at the WMAP frequencies. Therefore great care must be taken when using low frequency maps as tracers of the synchrotron emission at microwave frequencies. In the first release of the WMAP data, the Haslam 408 MHz template [84] was used [18], but in the three year version they use the WMAP K- and Ka-bands to provide a synchrotron template [90].

1.4.2 Free-free

Free-free emission is due to electron-ion scattering which produces microwaves. At frequencies above 10 GHz the free-free spectral index is $\beta_{ff} = -2.15$. Free-free emission does not dominate the sky at any radio frequency and hence there are no free-free maps. High resolution large-scale maps of Hα emission can be used as an approximate template for free-free emission, except for regions with high interstellar dust optical depth $\tau > 1$ at the wavelength of Hα. For $\tau \leq 1$ the Hα can be approximately corrected for extinction. The WMAP team use the Hα map assembled by [68] corrected for extinction using the Galactic reddening map provided in [157].

1.4.3 Dust

Thermal dust emission is produced by small dust grains that absorb UV radiation, re-emitting at the far-infrared and microwave frequencies. The spectral index depends on the grain material and lies in the range $1.5 \leq \beta_d \leq 2.5$. It has been mapped over the full sky by the COBE and IRAS missions. In [157] both datasets are combined to provide a full sky dust template. The WMAP team uses the extrapolation of this map performed in [67].

1.4.4 Anomalous dust emission

In the last years some works seem to support the existence of spinning dust emission at frequencies around 10–20 GHz [49], [192] produced by rotational electric dipole emission and, thus, has been named *spinning dust*. This emission has a similar frequency dependence to that of free-free emission at a certain range of frequencies. However this emission could provide a significant contribution to the WMAP data only for the K and Ka bands, whereas it quickly decreases at higher frequencies, becoming negligible [58] for the V and W bands.

1.4.5 Extragalactic point sources

Extragalactic objects such as quasars, galaxies, active galactic nuclei, infrared galaxies, starbursts or spheroids can also emit microwave radiation. As they are distant objects they appear as punctual objects in the CMB maps. The WMAP team identified and masked out several hundreds of point sources. Recently [116] provided a new catalogue using wavelets. For the PLANCK satellite, due to its better resolution and sensitivity, thousands of point sources are expected to be identified and masked.

1.4.6 Component Separation

Several statistical methods have been developed in order to separate each of the above described components. They can be classified into methods for diffuse components, such as Galactic foreground emissions and methods to identify compact objects, such as point sources and Sunyaev-Zeldovich effect. In the first group we can list the Maximum Entropy Method (MEM) [12], [91], [172], [186], Fast Independent Component Analysis (FastICA) [7], [118], Spectral Matching Independent Component Analysis (SMICA), [52], [140], Expectation -Maximization [123], Wiener filtering [24], [176], [178], Correlated Component Analysis (CCA) [23], and template fitting [17], [83], which is the approach used by the WMAP team. In the point source detection the matched filter [177], and wavelet based methods [28], [185], [187], [70], [116], have proved to be optimal. Scale adaptive filters [155], [88], multifilters [87], [89], and wavelet transforms [127], have been proposed for the Sunyaev-Zeldovich component separation.

1.4.7 Foreground masks

Despite all the component separation methods it is not possible to remove the foreground emissions completely. As most of the contaminating emission comes from our own Galaxy, the region of the sky lying on the galactic plane is usually excluded from cosmological studies. The WMAP team proposed different exclusion masks [18], [90], being the *kp0-mask* the most conservative one. This mask excludes around 23% of the pixels including a few hundreds of known point sources.

1.5 Gaussianity

1.5.1 Introduction

The Gaussianity of the CMB anisotropies is a testable prediction of the simplest inflationary models [74], [9]. The quantum vacuum fluctuations of the inflationary field have a Gaussian distribution. As mentioned before, inflation boosts the tiny vacuum fluctuations which seed the formation of structure in the later Universe. CMB anisotropies are related to energy density fluctuations through the linearized Einstein-Boltzmann equations. Hence their distribution is Gaussian as well (see [114]). Even in this scenario small departures from Gaussianity can arise due to non-linear second order effects. In the standard inflationary model these deviations from Gaussianity are negligible, but in alternative non-standard inflationary models the departure from Gaussianity is significant [13]. The degree of non-Gaussianity in inflationary models is usually quantified phenomenologically by the non-linear parameter f_{NL} in the gravitational potential:

$$\Phi = \Phi_L + f_{NL}\Phi^2, \tag{1.5.1}$$

where Φ_L is the gravitational potential at linear order. Using the 1-year WMAP data, [103] constrained $-54 < f_{NL} < 134$ at the 95% confidence level.

Topological defect models also predict non-Gaussian features in the CMB [191]. Unified theories of high energy physics predict the production of topological defects during a symmetry-breaking phase transition in the early Universe. Different types of defects were predicted depending on the broken O(N) symmetry: domain walls are two-dimensional membranes that form when a discrete symmetry ($N = 1$) is broken; after an axial or cylindrical symmetry break ($N = 2$), one-dimensional lines called cosmic strings arise; monopoles are point-like defects that form when the broken symmetry is spherical ($N = 3$); and finally global textures are formed after an $N = 4$ broken symmetry. For the case when $N > 4$ we have non-topological textures. Topological defects are extremely high-energy phenomena which leave an imprint in the CMB photons. Each type of defect produces a characteristic CMB-pattern, for instance textures may produce hot or cold spots in the CMB.

Another prediction of inflation is the homogeneity, isotropy and flatness of the Universe due to the drastic inflationary expansion. Non-trivial topologies [107] or anisotropic models [14], would leave characteristic imprints in the CMB. For

instance homogeneous and anisotropic models can produce a spiral pattern due to global rotation. Non-trivial topologies can produce anisotropic patterns, matched circles or, more generally deviations from a Gaussian random field.

Since most of the non-Gaussianity analyses are blind (not model-dependent), a great effort has to be done to identify the origin of a deviation from Gaussianity and/or isotropy. In addition to hypothetical primordial non-Gaussianities, most of the secondary anisotropies are not linear in nature and hence produce non-Gaussian signatures. The same is true for contaminants such as galactic and extragalactic foregrounds and instrumental or astrophysical systematics. Non-Gaussianity tests what the distribution is not, not what it is.

1.5.2 Gaussianity analyses

The primary challenge in studies of non-Gaussianity is in choosing the statistic that quantifies it. Depending on the kind of features that are investigated some methods will be more efficient than others. Since the detection of the CMB anisotropies in 1992, many Gaussianity analyses have been performed (see [124] for a review). The first ones analysed the 4 year COBE-DMR data [16] using a wide ensemble of methods, namely 3-point correlation functions [102], extrema distribution and correlations [102], [146], Minkowski functionals [158], [137],[102], [146] partition functions [55],[131], Principal Component Analysis [26], bispectrum [66], [86], [8], trispectrum [105] and wavelets listed in the next section. Some of these analyses revealed deviations from Gaussianity that were found to be due to systematic effects.

Further analyses studied balloon-borne and ground based experiments such as QMASK [141],[162], MAXIMA-1 [194],[152], [30],[3], BOOMERanG [148], Archeops [47] and VSA [156],[166],[150] without finding any significant deviation from Gaussianity.

As already mentioned, the WMAP data measured the CMB anisotropies with unprecedented accuracy. The first Gaussianity analysis performed on the 1–year WMAP data [103] found the data to be compatible with Gaussianity using Minkowski functionals and the bispectrum. Further analyses found several asymmetries and/or non-Gaussian features in the 1–year data using different methods: low multipole alignment statistics [50], [39], [40], [159], [108], [109], [110], [22], [165]; phase correlations [34], [37], [135], [136]; hot and cold spot

analysis [112], [113]; local curvature methods [80], [27]; correlation functions [61], [64], [180]; structure alignment statistics [193], [190]; multivariate analysis [56]; Minkowski functionals [142], [63]; bipolar spectra [76],[77]; and several statistics applied in wavelet space which we describe more in detail below.

Some of these anomalies have been redetected in the 3–year WMAP data [111], [51], [41], [65], [190]. However, [171] repeated the analysis of [103] and found the data to be compatible with Gaussianity although they do not re-evaluate the other statistics showing asymmetries or non–Gaussian signatures in the 1–year data.

The most important anomalies are perhaps: the alignment and symmetry features among low-l multipoles; the apparent asymmetries in the distribution of fluctuation power in two opposing hemispheres; alignment of local CMB features; and the one presented in this thesis [43], [44], [45], [46], a very cold spot in the southern hemisphere, which we call *the Spot*. This anomaly was pointed out first by [188] and confirmed by [43], [32], [44] and [45], [46] in the 3–year WMAP data. The tool used in these analyses is the Spherical Mexican Hat Wavelet defined in the next section.

The alignment of low-ℓ multipoles, the asymmetries, and alignment of CMB features are related to the ecliptic plane and hence are suspect to be due to some undetermined systematic effect. The origin of *the Spot* is analysed in this thesis. As we discuss in Chapter 5, it could be the first detection of a topological defect.

1.5.3 Wavelets

In a Fourier transform signals are represented as a sum of sinusoids. Analogously, a wavelet transform is the representation of a function by wavelets, which are mathematical functions different from sinusoids. The main difference is that wavelets are localized in time (or space) and frequency whereas the standard Fourier transform is only localized in frequency.

Applying a wavelet transform allows to divide a given function into different components. Each component matches the scale of the wavelet which is a scaled and translated copy of a finite-length or fast-decaying oscillating waveform, known as the *mother wavelet*.

There are many different wavelet transforms which can be classified into dis-

crete wavelet transforms, such as the Haar wavelet [75] and continuous wavelet transforms such as the Mexican Hat one. We will focus on the latter type of wavelet transforms.

In continuous wavelet transforms, the mother wavelet, $\Psi(x)$, satisfies the compensation, normalization and admissibility properties, namely,

$$\int_{-\infty}^{\infty} \Psi(x)dx = 0, \tag{1.5.2}$$

$$\int_{-\infty}^{\infty} |\Psi(x)|^2 dx = 1, \tag{1.5.3}$$

$$C_\Psi \equiv \left(2\pi^2\right) \int_0^{\infty} k^{-1}\Psi^2(k)dk < \infty, \tag{1.5.4}$$

where $\Psi(k)$ is the Fourier transform of $\Psi(x)$.

The wavelet (or *daughter wavelet*), ψ, can be defined in terms of the mother wavelet, the scale parameter R and the position b, as:

$$\psi_{R,b}(x) = \frac{1}{R}\Psi\left(\frac{x-b}{R}\right). \tag{1.5.5}$$

The wavelet coefficients, $w_{R,b}$ of a given function, $f(x)$, are defined as its convolution with the wavelet:

$$w_{R,b} \equiv \int f(x)\psi_{R,b}(x)dx. \tag{1.5.6}$$

The above formulas for one dimensional signals, can easily be extended to higher dimensions.

Wavelet transforms can be used for data compression, image processing, acoustics, optics, seismic geophysics, ... and astrophysics.

Several works have been published in recent years concerning CMB studies based on wavelets. Wavelet transforms can be applied to separate the different components appearing in microwave observations [179], [28], [185],[186], [187],[70], [116], [133], in denoising techniques [153], [154], cross-correlation analyses [189], [130], and in Gaussianity studies [139], [92], [4], [10], [11], [126], [128], [193], [190] and references listed below for the spherical symmetry case. Wavelets increase the signal to noise ratio, allowing to detect weak non-Gaussian signals. Furthermore they preserve the spatial location and the angular scale R of a hypothetical non-Gaussian feature.

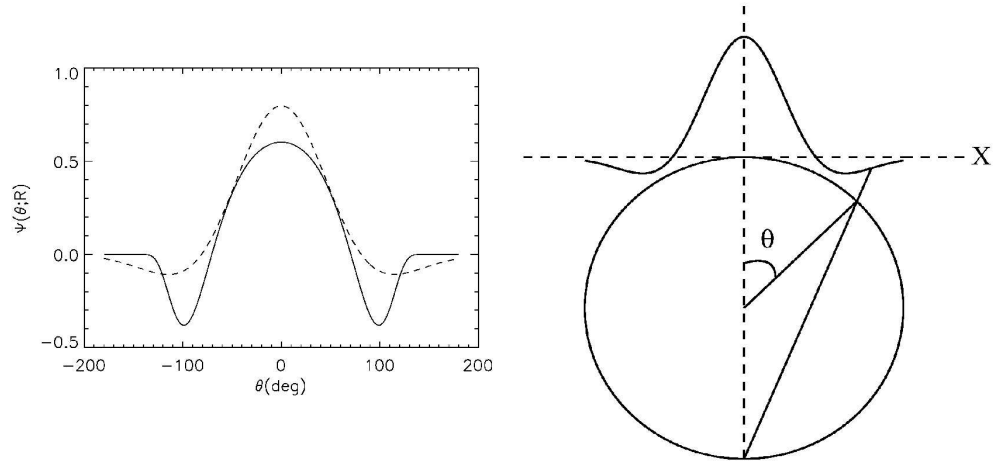

Figure 1.6 Left: Mexican Hat Wavelet on the plane (dashed line) and as deformed on the sphere (solid line). Right: Stereographic projection of the Mexican Hat Wavelet from the plane to the sphere. (From[122])

In our case, the chosen wavelet is the Spherical Mexican Hat Wavelet (SMHW) [6], which is the stereographic projection of the 2D Mexican Hat Wavelet defined by:

$$\Psi(x) = \frac{1}{\sqrt{2\pi}}\left[2 - \left(\frac{x}{R}\right)^2\right] e^{-x^2/2R^2}, \tag{1.5.7}$$

which is the Laplacian of a Gaussian and where $x \equiv |\vec{x}|$.

The SMHW efficiently enhances the non-Gaussian signatures on the sphere [122]. The expression of the SMHW mother wavelet is:

$$\Psi_S(y,R) = \frac{1}{\sqrt{2\pi}N(R)}\left[1 + \left(\frac{y}{2}\right)^2\right]^2 \left[2 - \left(\frac{y}{R}\right)^2\right] e^{-y^2/2R^2}, \tag{1.5.8}$$

where R is the scale and $N(R)$ is the normalization constant:

$$N(R) \equiv R\sqrt{1 + R^2/2 + R^4/4}. \tag{1.5.9}$$

The distance y on the tangent plane is related to the polar angle (θ) as: $y \equiv 2\tan\theta/2$. The MHW and SMHW functions can be seen in Figure 1.6.

The SMHW has been applied to non-Gaussian studies of the COBE-DMR data [29], [31].

This thesis presents an analysis of the WMAP data with the SMHW, written in [43], [44], [45], [46]. Several other analyses of the WMAP data [188], [134], [27], [82], [32] or [189] have been performed with the SMHW.

1.6 Outline

In this thesis we present a non-Gaussian analysis of the WMAP data, performed with spherical wavelets. In the next chapter the detection of a non-Gaussian spot in the 1–year data is described [43]. In Chapter 3 the morphology and foreground contribution to *the Spot* are analysed [44]. In Chapter 4 we show the redetection of the spot in the 3–year WMAP data [45]. Chapter 5 explores the possibility that *the Spot* is due to a cosmic texture [46]. Chapter 6 presents the conclusions and finally a summary in Spanish language can be found in the last chapter.

CHAPTER 2

Detection of a non-Gaussian Spot in the WMAP 1–year data

An extremely cold and big spot in the WMAP 1-year data is analysed. Our work is a continuation of a previous paper [188] where a deviation from Gaussianity was detected, with a method based on the Spherical Mexican Hat Wavelet (SMHW) technique. We study the spots at different thresholds on the SMHW coefficient maps, considering six estimators, namely number of maxima, number of minima, number of hot and cold spots, and number of pixels of the spots. At SMHW scales around 4° (10° on the sky), the data deviate from Gaussianity. The analysis is performed on all sky, the northern and southern hemispheres, and on four regions covering all the sky. A cold spot at ($b = -57^\circ, l = 209^\circ$) is found to be the source of this non-Gaussian signature. We compare the spots of our data with 10000 Gaussian simulations, and conclude that only around 0.2% of them present such a cold spot. Excluding this spot, the remaining map is compatible with Gaussianity and even the excess of kurtosis in [188], is found to be due to this spot. Finally, we study whether the spot causing the observed deviation from Gaussianity could be generated by systematics or foregrounds. None of them seem to be responsible for the non-Gaussian detection.

2.1 Introduction

The work carried out in this chapter is a continuation of a previous paper [188] where a non-Gaussian detection in the WMAP 1-year data was reported, using the Spherical Mexican Hat Wavelet (SMHW). Convolving the data with the

SMHW, an excess of kurtosis was found at scales around 4°, involving a size on the sky close to 10°. The deviation from Gaussianity presented an upper tail probability of 0.4%. This deviation was localised in the southern hemisphere and an extremely cold spot at $b = -57^\circ, l = 209^\circ$, was regarded as a possible source of the non-Gaussianity. Our aim is to localise the non-Gaussianity, specifying whether this spot (hereafter *the Spot*) alone is the origin of the detection, and to study all the spots of the data in order to quantify how atypical *the Spot* under a Gaussian model is.

Following the same procedure as in [188], we have produced 10000 Gaussian simulations with the purpose of checking the Gaussianity of the data. Starting with the cosmological parameters estimated by the WMAP team (Table 1 of [170]), we have calculated the C_ℓ using CMBFAST [161]. We have generated random Gaussian $a_{\ell m}$ of CMB realizations and convolved them with the adequate beam for each receiver. After transforming from harmonic to real space, uncorrelated Gaussian noise realizations have been added, taking into account the number of observations per pixel ($N_j(\mathbf{x})$) and the noise dispersion per observation (σ_{0_j}). At this point the simulations were degraded to $N_{side} = 256$ and the *Kp0* mask has been applied. Finally, monopole and dipole have been subtracted outside the mask

In the present work we have studied the spots above or below a given threshold ν, therefore we have normalised the data and the simulations, dividing each map by its dispersion, after subtracting the mean.

Data and simulations have been convolved with the SMHW at different scales, to obtain the SMHW coefficient maps analysed in this work. The study has also been performed in the data and simulations previous to the convolution with the SMHW. These maps are referred to as maps in real space, at scale R_o.

We have considered the following six estimators: number of maxima, number of minima, number of hot spots, number of cold spots, number of hot pixels (hot area) and number of cold pixels (cold area). All of them are referred to a particular threshold; thus maxima, hot spots and hot pixels lie above a threshold ν, whereas number of minima, cold spots and cold pixels lie below $-\nu$. The analysis has been done in seven regions: all sky, northern hemisphere, southern hemisphere, Northeast ($b > 0, l < 180$), Northwest ($b > 0, l > 180$), Southeast ($b < 0, l < 180$) and Southwest ($b < 0, l > 180$). Each region has its own dispersion and has to be normalised separately.

2.2 The analysis

The first step in our analysis is the convolution of data and simulations with the SMHW at 15 scales ($R_1 = 13.7$, $R_2 = 25$, $R_3 = 50$, $R_4 = 75$, $R_5 = 100$, $R_6 = 150$, $R_7 = 200$, $R_8 = 250$, $R_9 = 300$, $R_{10} = 400$, $R_{11} = 500$, $R_{12} = 600$, $R_{13} = 750$, $R_{14} = 900$ and $R_{15} = 1050$ arcmin). Since the convolution mixes up pixels of the masked region with unmasked pixels, the resulting map has many corrupted SMHW coefficients. This effect involves a loss of efficiency, so we applied an additional mask as explained in [188], extending the *Kp0* mask to 2.5 R. The results in [188] were shown to be quite independent of the definition of this extended mask. For each map we have calculated the estimators on the seven previously described regions. The chosen thresholds are ± 2.0, ± 2.5, ± 3.0, ± 3.5, ± 4.0 and ± 4.5. In the figures we have represented only absolute values for the thresholds, recalling that for cold spots and minima, values lie below a negative threshold, whereas hot spots and maxima values lie above a positive threshold.

Once the estimators were calculated for data and simulations, we proceeded to establish acceptance intervals at significance levels α (32%,5% and 1%). Therefore we have sorted the 10000 values of each estimator into ascending numbers and excluded $10000\alpha/2$ values from each tail of the distribution. The two limiting values, corresponding to simulations $1 + 10000\alpha/2$ and $10000(1 - \alpha/2)$ define the acceptance interval containing a probability of $1 - \alpha$. The remaining probability is $\alpha/2$ above and below the interval. In all figures this acceptance intervals are plotted, the 32% interval corresponds to the inner band, the 5% interval to the middle band and the 1% significance level, to the outer one.

The results for the different regions are presented in the next three subsections.

2.2.1 All sky, North and South

Deviations from Gaussianity have been detected at scales R_5, R_8 and R_9. For threshold 3.0, the results are represented in Figure 2.1. At scale R_5 the hot area lies outside the 1% acceptance interval. However we have studied this case carefully, noting that this threshold is the only one where data lie outside the intervals, whereas the number of hot spots and number of maxima do not depart from Gaussianity, even at this scale. Dividing the sky into two hemispheres we checked that this was not a localised effect either. Even contiguous scales were compatible with Gaussianity, hence we concluded that this non-Gaussian

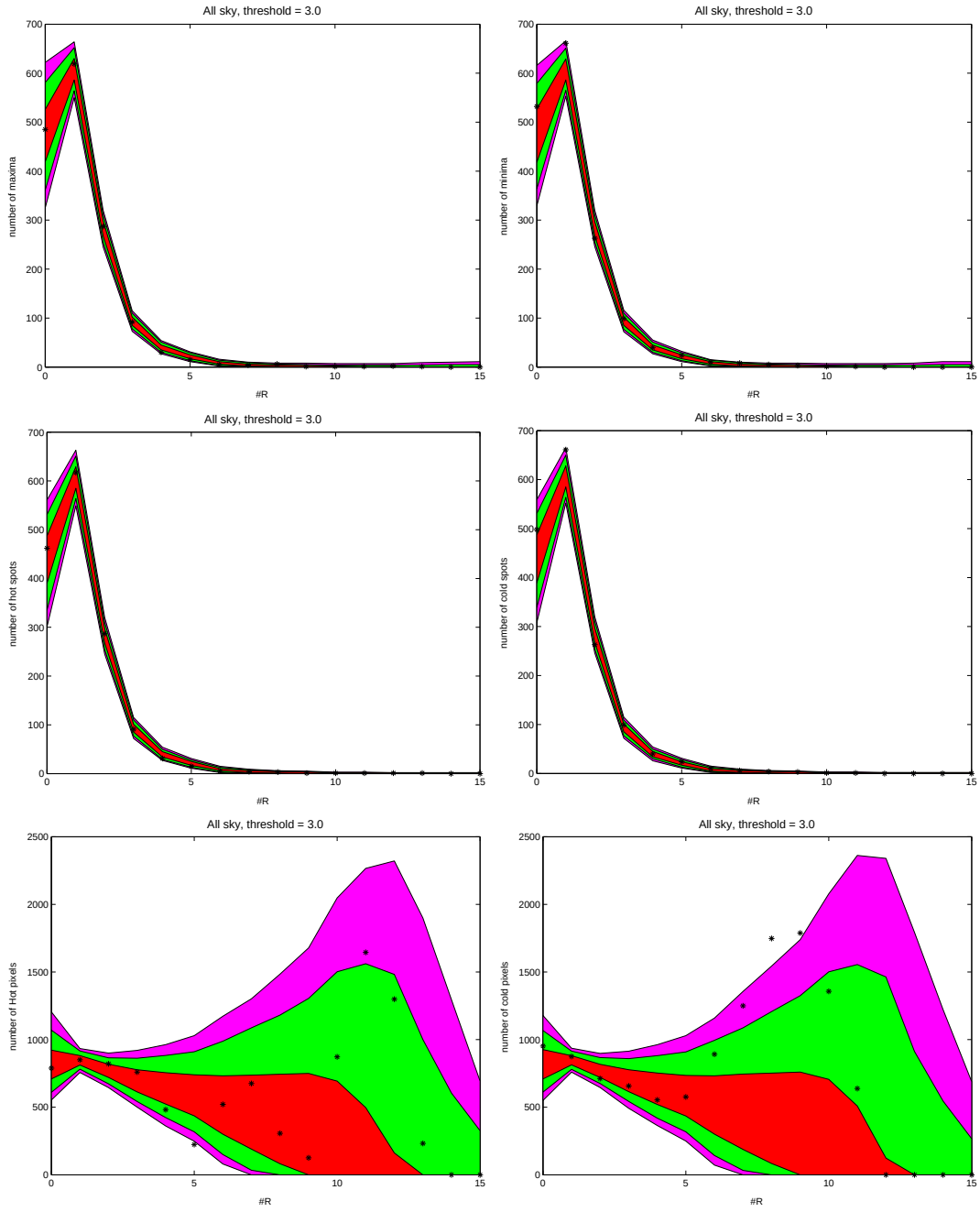

Figure 2.1 This figure shows from left to bottom and top to bottom, number of maxima, number of minima, number of hot spots, number of cold spots, hot and cold area for each of the considered scales at threshold 3.0. Scale R_0 corresponds to real space. The combined map values are plotted as asterisks. The acceptance intervals for the 32% (inner), 5% (middle) and 1% (outer) significance levels, given by the 10000 simulations are also plotted. Non-Gaussianity is found at scales R_5 in the hot area, R_8 and R_9 in the cold area. At other scales the data always lie at least within the 1% acceptance band. For scale R_5 the deviation occurs only for this threshold and scale whereas scales R_8 and R_9 show a more significant detection.

feature was not significant.

On the contrary, in the case of cold areas, deviations are observed at scales R_8 and R_9 at several thresholds as can be seen in Figure 2. We represent in Figure 2.2 the number of cold spots, cold area and number of minima, for all considered thresholds at scales R_8 and R_9, in order to observe what is happening there with more detail. The number of minima and cold spots was exactly one at thresholds 4.0 and 4.5, reaching the borderline of our 1% acceptance interval. For the number of cold spots, at threshold 4.0 for scale R_8 and thresholds 3.5 and 4.0 for scale R_9, the 5% and 1% acceptance intervals coincide. This can happen when the number of spots is very low. Consider for example a binomial distribution where the number of spots can only take values 0 or 1. The way we define the acceptance intervals determines that for such cases some of these intervals must coincide. The most striking non-Gaussian signature was found for the cold area at scales R_8 and R_9 where the data exhibited an extremely high number of cold pixels at thresholds over 3. The cold area lies outside the 1% acceptance interval at thresholds above 3.0 in the two scales presented in Figure 2.2.

At thresholds 4.0 and 4.5 the mentioned observations reveal that the deviation from Gaussianity is only due to one particular spot, which reaches a minimum value of -4.7σ at $(b = -57^\circ, l = 209^\circ)$ and scale R_9. At lower thresholds several spots contribute to the observed deviation. A precise analysis of *the Spot* is presented in the following sections. The data suggest that we are dealing with a very cold and big spot. These results agree with the results reported in [188], since the non-Gaussianity has been detected at the same scales. The hot spots did not show any non-Gaussian evidence. Furthermore, subtracting the cold pixels from the hot pixels, a strong hot-cold asymmetry was revealed at scales R_8, R_9 and R_{10}, see Figure 2.3. The lower tail probabilities displayed in Table 2.1 show non-Gaussian values of up to 99.85%.

Our purpose was to locate the non-Gaussian sources. We studied the northern and southern hemispheres separately, expecting to find non-Gaussian results in the southern hemisphere because *the Spot* is located there. Results presented in Figure 2.4 show that the northern hemisphere is compatible with the Gaussian simulations whereas the southern hemisphere shows a clear deviation from the acceptance intervals. To show the North-South asymmetry, the number of hot and cold pixels in the South were subtracted from the Northern

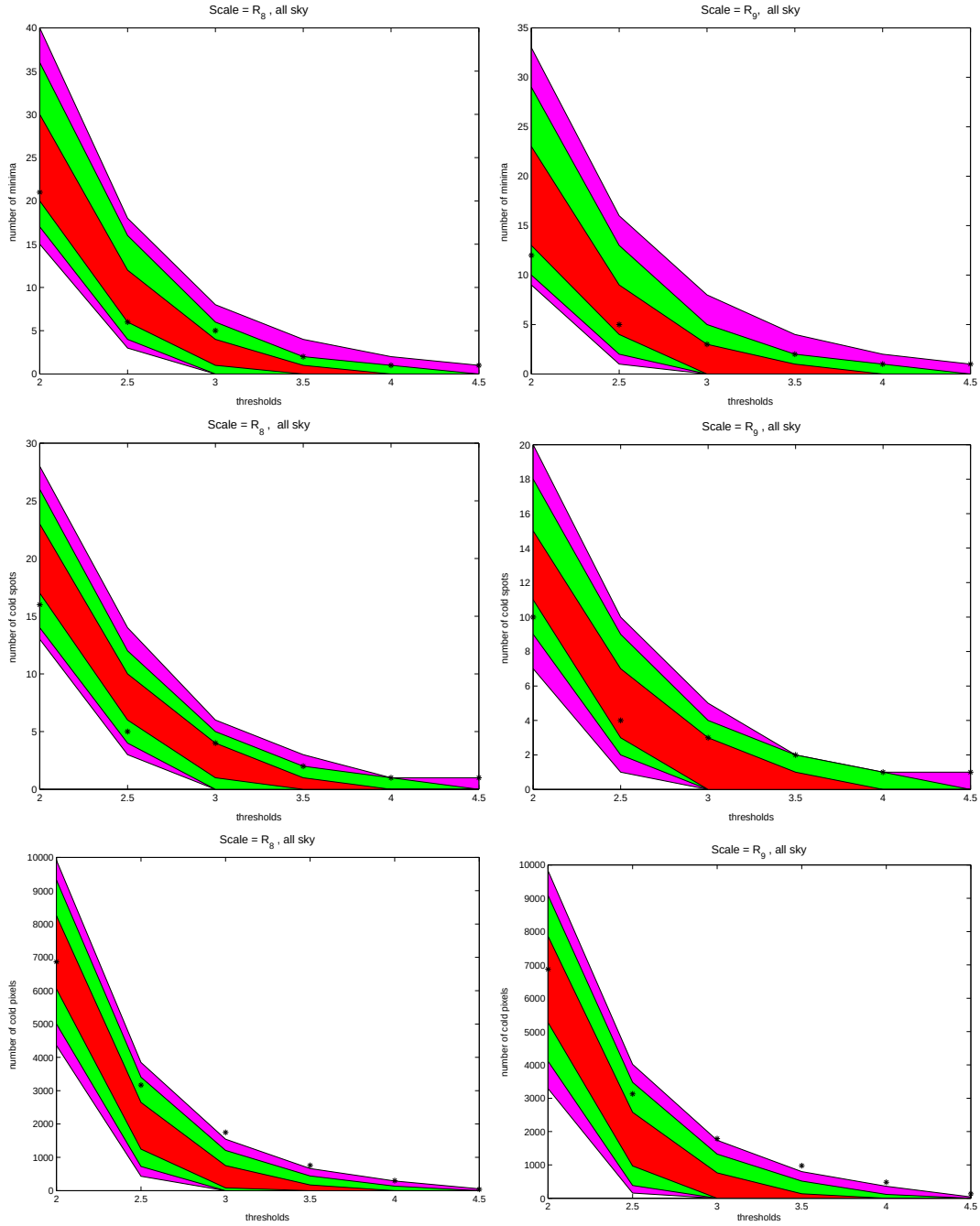

Figure 2.2 Number of minima, number of cold spots and cold area are shown for scale R_8 at the left column and scale R_9 at the right column. As in figure 2.1 the asterisks represent the combined WMAP data, and the acceptance intervals for the 32% (inner), 5% (middle) and 1% (outer) significance levels, given by the 10000 simulations are also shown. The data lie outside the acceptance intervals for the area, at thresholds over 3.0. The borderline of the 5% and 1% acceptance intervals coincide at some high thresholds for the number of spots, because at this scales the number of spots is very low.

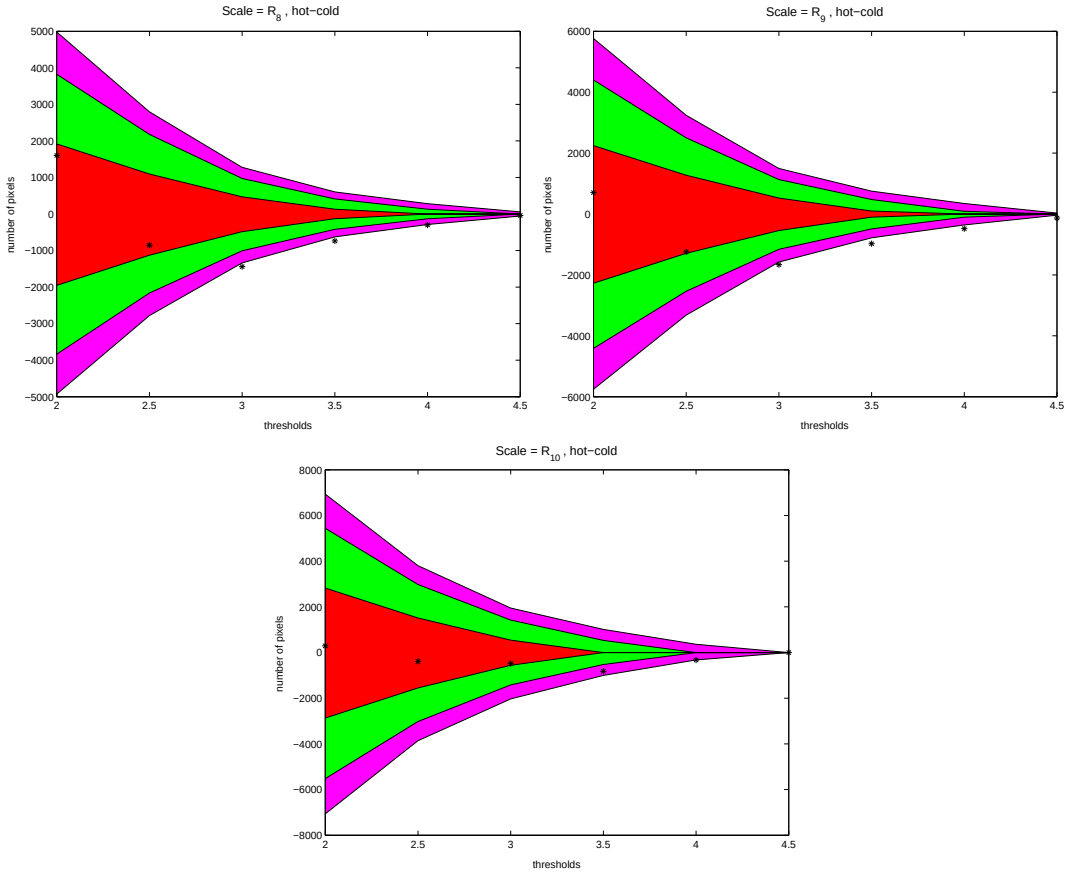

Figure 2.3 Hot-cold asymmetry, in the area. The excess of cold pixels at scales R_8, R_9 and R_{10} happens at high thresholds. Data and acceptance intervals are represented in the same manner as in previous figures.

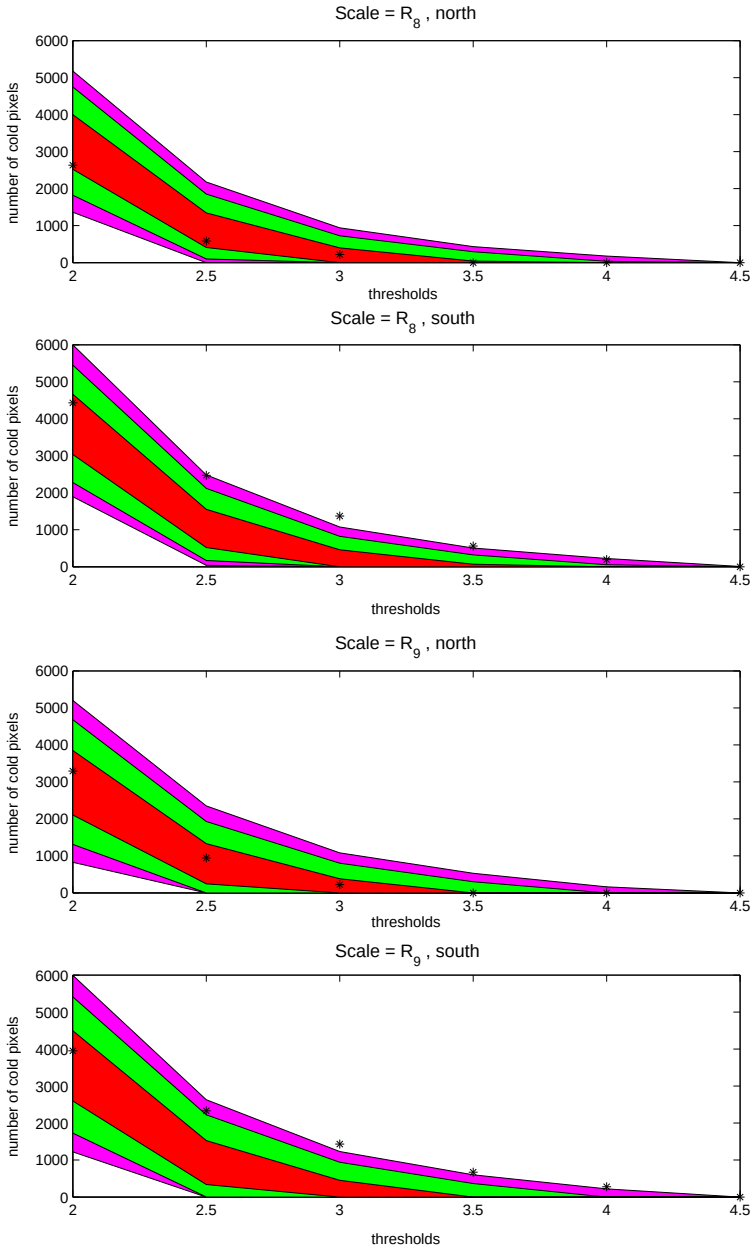

Figure 2.4 Cold area in the northern and southern hemispheres at scales R_8 and R_9. The southern hemisphere shows a non-Gaussian behaviour. Again we represent data and acceptance intervals as in Figure 2.1.

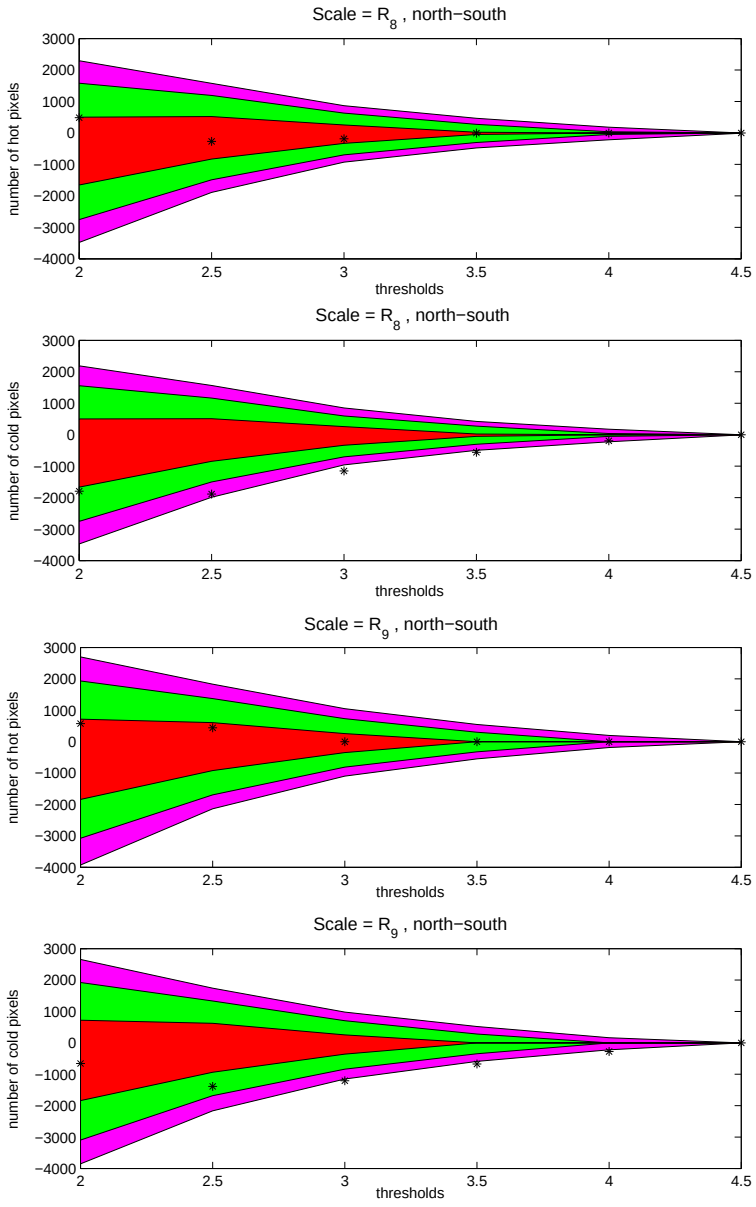

Figure 2.5 The two upper panels represent the North-South asymmetry for hot and cold area, at scale R_8 and the two panels below, the mentioned asymmetries at scale R_9. The southern hemisphere shows an excess of cold pixels. Acceptance intervals and data are represented as in previous figures.

Scale	threshold	probability
R_8	3.0	0.37%
	3.5	0.26%
	4.0	0.44%
	4.5	0.65%
R_9	3.0	0.39%
	3.5	0.15%
	4.0	0.19%
	4.5	0.22%
R_{10}	3.0	18.22%
	3.5	1.04%
	4.0	0.48%

Table 2.1 Lower tail probabilities of having the hot-cold asymmetry (in the number of pixels) of our data under a Gaussian model, at different scales and thresholds. Most of the values are below 1%. At scale R_{10} and threshold 4.5 the number of hot and cold pixels are both zero, because the threshold is too high and therefore we do not show this threshold for the mentioned scale.

ones. Results are presented in Figure 2.5. Deviations from Gaussianity can be clearly observed in the number of cold pixels at thresholds 3.0 and above. Previous works such as [188], [61] or [81] have already reported North-South asymmetries, which are confirmed here.

The marked observed asymmetry, prompted us to divide the sky into four regions with the purpose of studying a Southeast-Southwest asymmetry.

2.2.2 Four regions

We analysed four regions independently by splitting each hemisphere into two parts, $l < 180$ (East) and $l > 180$ (West). The results presented in Figure 2.6 clearly reveal the location of the non-Gaussian signatures. The Southwest is the only region where the data lie outside the acceptance intervals. As expected, the region containing *the Spot* is not compatible with Gaussianity, whereas the other three regions are compatible with a Gaussian behaviour. Note that although in [62] the ILC weights were found to have particular values in this region, this does not affect our results since we use the combined, cleaned Q-V-W map.

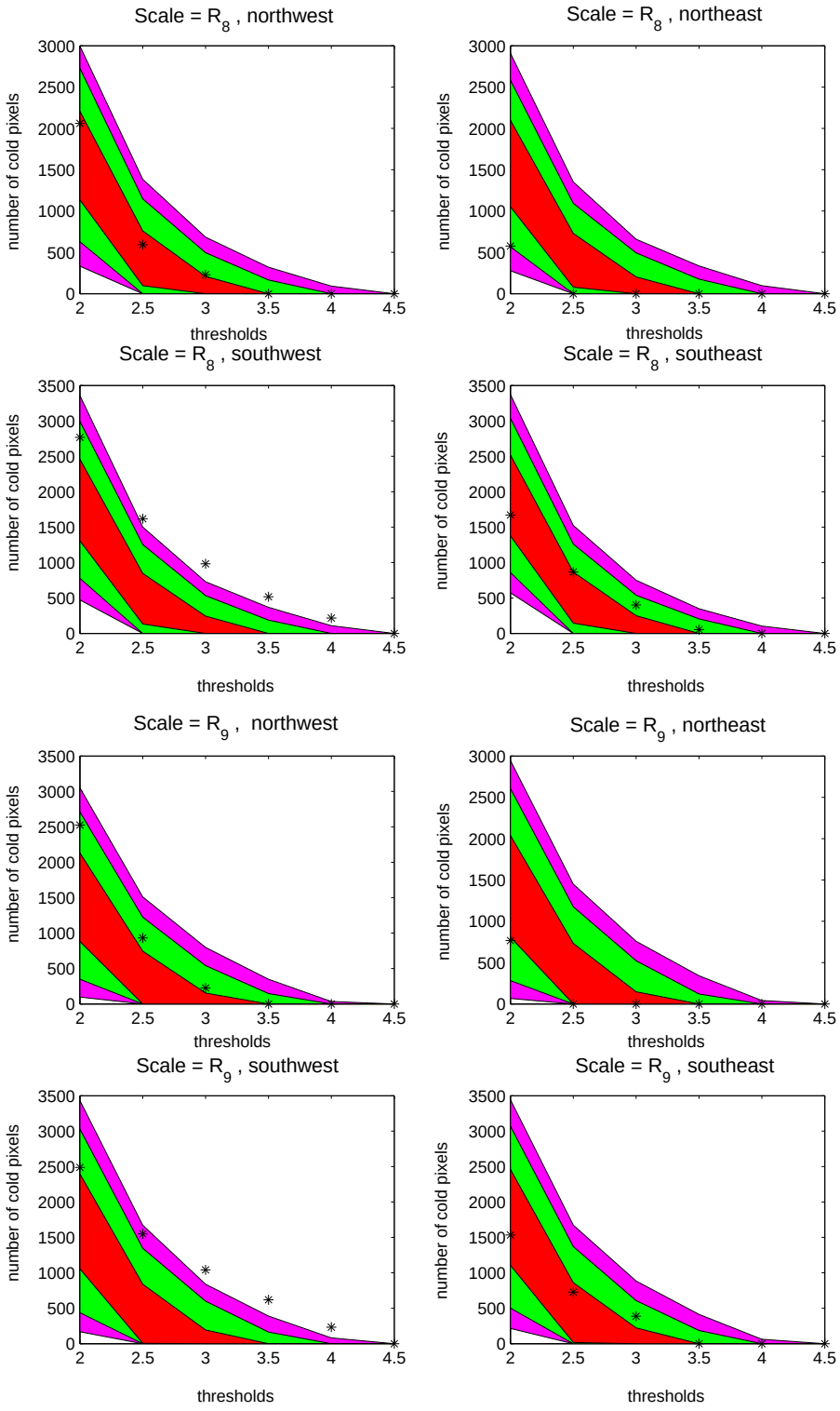

Figure 2.6 Cold area in four regions, scales R_8 and R_9. The only non-Gaussian region is the southwest. The acceptance intervals are plotted as in Figure 2.1.

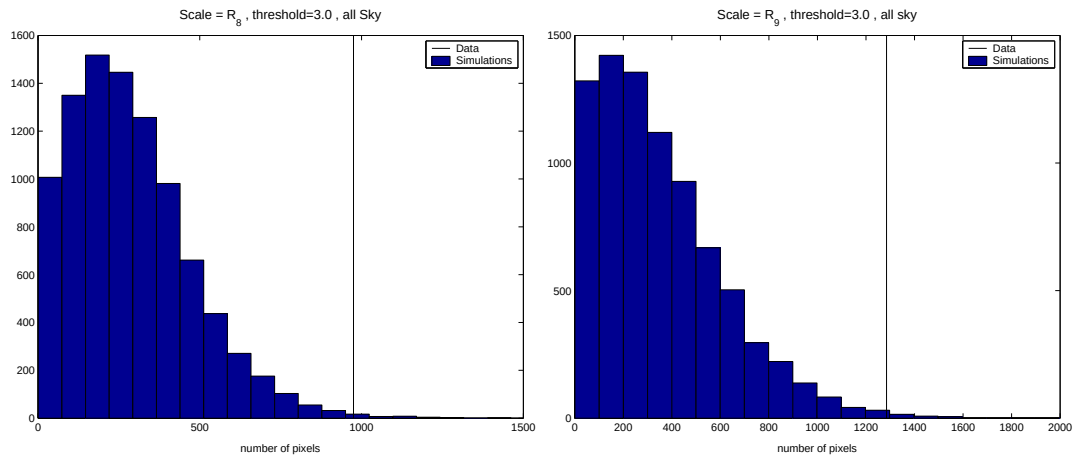

Figure 2.7 Histogram of all biggest cold spots, threshold 3.0, scales R_8 and R_9. The vertical line represents *the Spot*.

In the next section we quantify the significance of *the Spot*.

2.2.3 The Spot

Our aim in this section is to quantify the probability of finding a spot like the one found at ($b = -57°, l = 209°$) in a Gaussian, homogeneous and isotropic random field, and to check whether the map without *the Spot* is compatible with Gaussianity or not. Comparing *the Spot* with the biggest cold spot of each simulation we can estimate the probability of observing such a spot for the Gaussian model. We show the histograms with the biggest cold spot of each simulation at threshold 3.0 and scales R_8 and R_9 in Figure 2.7. The results for all thresholds are summarized in Table 2.2. Note that some simulations do not have any spots at high thresholds and hence they do not appear in the histograms but we take them into account to estimate the probabilities. All probabilities are below 0.7%. The lowest value is 0.18%.

At this point we can make the hypothesis that the data could be explained as the sum of a Gaussian, homogeneous and isotropic random field, plus a non-Gaussian spot which is not generated by this field. With the purpose of checking our hypothesis, we have compared the cold area of data and simulations, at scales R_8, R_9 and thresholds 3.0, 3.5 where the data present more than one spot. First we have estimated the upper tail probabilities of finding the total cold area (including all cold spots), counting how many simulations present

Scale	threshold	probability
R_8	3.0	0.34%
	3.5	0.32%
	4.0	0.41%
	4.5	0.65%
R_9	3.0	0.38%
	3.5	0.21%
	4.0	0.18%
	4.5	0.22%

Table 2.2 Upper tail probabilities of having *the Spot* under a Gaussian model, at different scales and thresholds. All probabilities are smaller than 1%.

Scale	threshold	P with Spot	P without Spot
R_8	3.0	0.18%	14.79%
	3.5	0.28%	18.28%
	4.0	0.45%	-
	4.5	0.65%	-
R_9	3.0	0.39%	30.53%
	3.5	0.18%	17.68%
	4.0	0.19%	-
	4.5	0.22%	-

Table 2.3 Upper tail probabilities of having the cold area measured in the data, under a Gaussian model The third column displays the probabilities considering *the Spot* and the right column shows the probabilities subtracting *the Spot* from the data. At thresholds 4.0 an 4.5 only *the Spot* is present, hence it makes no sense considering probabilities without *the Spot*.

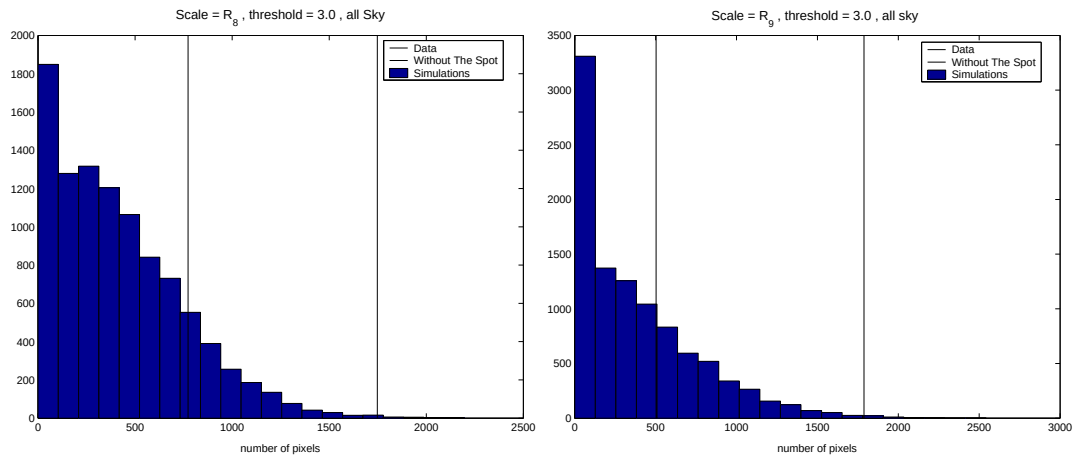

Figure 2.8 Histogram of all cold areas, threshold 3.0, scales R_8 and R_9. The data without *the Spot* (line on the left) are compatible with Gaussianity, whereas the data with *the Spot* (line on the right), are non-Gaussian with probabilities 99.82% and 99.61% at this threshold.

a greater or equal cold area, obtaining very low values (see Table 2.3). If we subtract *the Spot* from the cold area in the data, and calculate again the probabilities, we appreciate how the remaining area is compatible with Gaussianity, since the upper tail probabilities grow in a factor of 100. This result is represented in Figure 2.8. The line on the right hand side is the total cold area of the data whereas the one on the left hand side is the area remaining after subtracting *the Spot*. The increase in probability can easily be appreciated. Here we should have considered that we were using fewer pixels in the data than in the simulations because *the Spot* has been subtracted only in the data. But since these pixels represent only about 0.5% of the total pixels at scales R_8 and R_9, we can neglect them, without modifying substantially the results. Hence regarding *the Spot* as a non-Gaussian outlier, the remaining data are compatible with Gaussianity.

To finish this section, we want to remark some characteristics of *the Spot*. Before convolving the combined map, *the Spot* appears as several smaller, resolved spots with a minimum temperature of $-398\mu K$ at $(b = -56°, l = 210°)$. The average value of the four most prominent spots, listed in table 2.4 is $-348\mu K$. However, these four spots are not exclusively responsible for *the Spot*, since removing them, the mean value of the remaining pixels forming *the Spot*, is close to -1σ. We have filtered the combined map with a Gaussian of scale 4°,

	Combined WMAP	
Amplitude (μK)	Position (b, l)	area ($\nu = -2$)
-346	$(-60°, 213°)$	46
-398	$(-56°, 210°)$	67
-331	$(-54°, 211°)$	42
-317	$(-56°, 203°)$	88
	Gaussian (4°)	
Amplitude (μK)	Position (b, l)	area ($\nu = -2$)
-73	$(-57°, 209°)$	699

Table 2.4 Before filtering the combined map, *the Spot* appears resolved in several spots. At the top we show three characteristic values of the most prominent spots, namely the area below threshold -2, amplitude and position of the minimum. Filtering with a Gaussian of 4° all these spots are convolved, becoming one big spot. The characteristics of this spot are shown at the bottom.

the characteristic scale given by the SMHW analysis. *the Spot* appears with an amplitude of $-78\mu K$ at $(b = -56°, l = 210°)$ as summarized in Table 2.4.

2.2.4 Skewness and kurtosis

At scales R_8 and R_9, the kurtosis presented non-Gaussian values in [188]. We have repeated the analysis of [188], masking *the Spot* in the wavelet coefficient maps, to show to which extent *the Spot* is responsible for the excess of kurtosis. The masked pixels, were the pixels of *the Spot* lying above threshold 3.0 at scale R_8. The results are presented in Figure 2.9. The stars represent the data and the circles, the data without the Spot. By subtracting *the Spot*, the decrease of the kurtosis is clearly observed, being now compatible with Gaussianity. The acceptance intervals are the same as in [188], and they were not recalculated masking the pixels of *the Spot* in the simulations, since the number of masked pixels is negligible with respect to the total number of pixels. However the decrease in the kurtosis is so huge, that a slight modification of the intervals would not affect our conclusions. The skewness is still compatible with Gaussianity. Note that *the Spot* was masked after convolving with the wavelets. Masking *the Spot* before convolving, the decrement of the kurtosis is even higher. This results show again the Gaussian behaviour of the data without *the Spot*. Hence

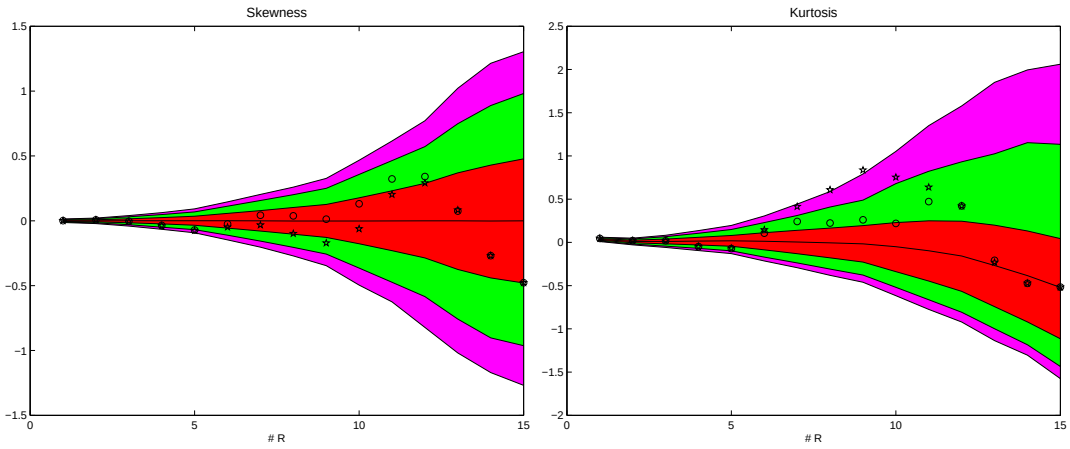

Figure 2.9 This figure shows the values of skewness (left) and kurtosis (right) for all the considered scales. The combined map values are plotted as stars and as written in [188], at scales R_8 and R_9 they lie outside the three acceptance intervals, which are represented as in previous figures. Masking those pixels of *the Spot* which are above threshold 3.0 at scale R_8, we obtain the results represented by circles. The huge decrement of the kurtosis makes the data compatible with Gaussianity.

we can conclude that the excess of kurtosis is due to *the Spot*.

2.3 Sources of non-Gaussianity

Although the analysis of [188] showed that systematics, foregrounds and variations of the power spectrum were not responsible for the non-Gaussian effect shown in the kurtosis, we wanted to check again their influence in the non-Gaussian results obtained in the present analysis.

2.3.1 Systematics

First we studied the effects of systematics related to instrumental features (noise and beam), generating four sets of 10 simulations. The first two sets are normal simulations with noise and beams. In the third set we made the same simulations as in the first set but without noise, and in the fourth set we took the simulations of the second but without beam. Comparing the first and the third set, we can see how the noise affects the number of pixels in a spot or the total cold area, and comparing sets two and four, we check the influence of the

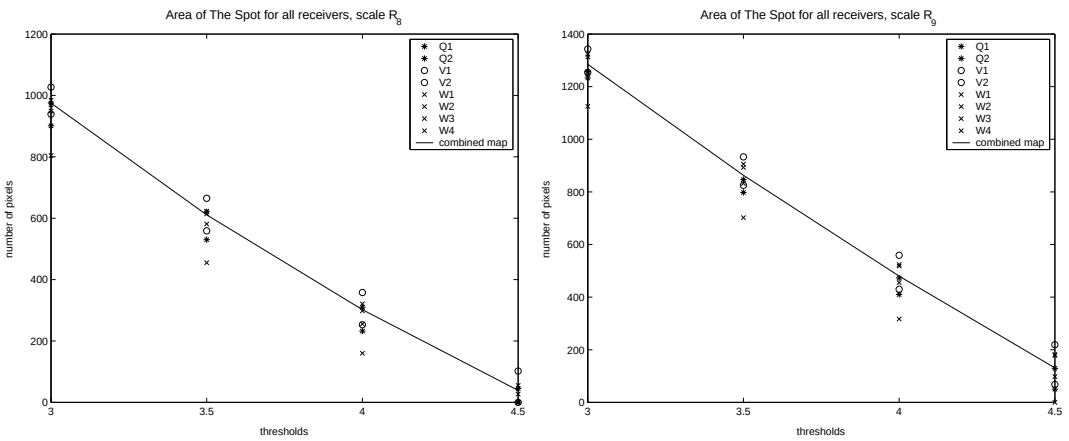

Figure 2.10 Area of *the Spot* for all receivers, at threshold 3.0 and scales R_8 and R_9. The line represents the combined map values whereas the other symbols denote the different receivers. *The Spot* is detected in all receivers, hence no rare receiver is generating the non-Gaussian signal.

beams. We have compared the spots and the total area of these sets at scales R_8 and R_9, and threshold 3.0. In all cases the mean relative variation of the area of one spot was around 2% and the mean relative variation of the total area in a simulation around 1%. This values are negligible and confirm that noise and beams do not play a significant role in our results, although the number of considered simulations is not very high. The previous results in [188] support our conclusions.

Another possible source of non-Gaussianity could be the influence of any rare receiver. We have analysed the spots detected by the 8 Q-V-W receivers, Q1, Q2, V1, V2, W1, W2, W3 and W4, independently. The results for scales R_8 and R_9 are plotted in Figure 2.10. Although W2 detects less pixels than the other receivers, all of them detect *the Spot*, and are close to the line representing the values of the combined map. Hence we verify that our detection is not due to any deficient receiver.

2.3.2 Foregrounds

Non-Gaussianity can be generated by foregrounds due to synchrotron, free-free and thermal dust emissions. All foregrounds show a clear frequency dependence and hence if our spot is generated by foregrounds its area should also be frequency dependent. Therefore, in Figure 2.11 we have compared the area

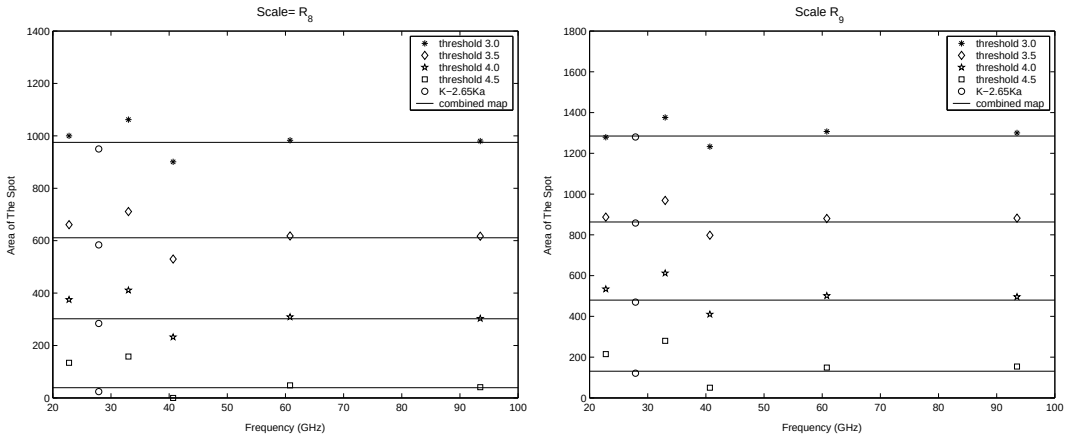

Figure 2.11 Frequency dependence of the area of *the Spot*, at thresholds over 3.0 and scales R_8 and R_9. The lines represent the combined map values. From top to bottom thresholds 3.0 (asterisks), 3.5 (diamonds), 4.0 (stars) and 4.5 (squares) are plotted. The circles are the values for the map $K - 2.65Ka$, where the synchrotron emission should be canceled. These circles are close to the combined map values, hence synchrotron emission is not the cause of *the Spot*.

of *the Spot* for each channel, namely K(22.8 GHz), Ka(33.0 GHz), Q(40.7 GHz), V(60.8 GHz) and W(93.5 GHz) at scales R_8 and R_9 and thresholds over 3. The horizontal lines denote the combined map values, whereas the other symbols correspond to the area of *the Spot* at different thresholds for each channel.

The first two channels are not foreground corrected and so they may not match the results of the other channels and of the combined map. In fact as can be seen in Figure 2.11 both channels deviate slightly from the horizontal lines, representing the combined map values. Since these channels are not foreground corrected, we can attribute the deviation to the synchrotron radiation, which dominates at these frequencies. The synchrotron emission is expected to grow a factor 2.65 from 33 GHz to 23 GHz,[1] hence if we subtract 2.65 times the Ka-map from the K one, we get rid of the contaminating emission. Considering Figure 2.11, we confirm that the circles corresponding to K-2.65Ka are very close to the combined map values.

These results support the conclusions reached in [188] regarding the influence of foregrounds in the non-Gaussian detection The independence of the ampli-

[1] A power law is assumed for the frequency dependence of the synchrotron emission: $T_{syn}(\nu) \propto T_{syn}(\nu_0)\left(\nu/\nu_0\right)^{-2.7}$, as proposed in [18].

tude of *the Spot* with frequency, was already shown in the mentioned paper.

2.3.3 Power spectrum dependence

Since several anomalies and asymmetries have been found in the low multipoles of the power spectrum, we should discuss to which extent the result depends on the power spectrum. We have used the best fit WMAP power spectrum to perform the 10000 Gaussian simulations, but the uncertainties in the cosmological parameters and hence in the power spectrum could affect our results. We have performed three sets of 50 simulations. The first set corresponds to the best fit WMAP power spectrum. The other two sets were generated with power spectra differing by $\pm 1\sigma$ from the best fit WMAP power spectrum. One corresponds to the 'lower limit' power spectrum, obtained subtracting the 1σ error estimated by the WMAP team, and the other one to the 'upper limit' power spectrum, adding the mentioned 1σ error to the best fit spectrum. Comparing the first set with the two others, we can study how the spots are affected by the choice of different power spectra.

At scales R_8 and R_9, and threshold 3.0 the mean relative variation of the area of a particular cold spot is much lower than 1%. Therefore, after these negligible variations, the significance of *the Spot* remains unchanged. Also in [188] a negligible power spectrum dependence of the acceptance intervals was found for the kurtosis. Hence the choice of different power spectra does not affect significantly our results.

2.3.4 Intrinsic anisotropies

Once we have discarded systematics and foregrounds as the cause of our detection, other sources have to be considered. For instance the Sunyaev-Zeldovich effect could produce a cold spot. This effect occurs in clusters, when high energetic electrons collide with CMB photons originating a decrement of the temperature in our range of frequencies. Here arise two problems, namely the angular scale and the amplitude of *the Spot*. The non-Gaussianity is found at scales around 4° implying a size of about 10° on the sky. Observing in real space this region, *the Spot* appears resolved in several smaller very cold spots with a minimum temperature around $-398\mu K$. We have looked for any extragalactic object which could cover this angular scale at coordinates near ($b = -57^\circ, l = 209^\circ$).

We found a group of galaxies belonging to the local supercluster at a distance of about 20 Mpc subtending a similar angle on the sky. Some of these galaxies match the resolved spots observed in the data. However the mass and temperature of the gas necessary to reach the amplitude of our spot, are similar to the values found in rich clusters and therefore much higher than the amounts estimated for groups of galaxies (see [175]). We would need a big cluster, such as the Coma one, to reach such an amplitude and it should be near enough to cover 10 degrees on the sky. In the neighborhood of ($b = -57^\circ, l = 209^\circ$) no such object is found. This is in agreement with the WMAP results on foregrounds [18] where the Sunyaev-Zeldovich effect was found to be negligible except for the most prominent nearby cluster, Coma, observed with a signal to noise ratio of ≈ 2. Even more, we have also considered the ACO catalogue [1] and the All-Sky ROSAT maps [168] at 0.1, 1.2 and 2 keV and neither any ACO cluster nor any special X-ray emission was found at position of *the Spot*. However, the ROSAT maps present some particular problems: the brightest point sources, as well as a large fraction of clusters, have been removed from it. In addition, some small fractions of the sky were not observed and, unfortunately, one of them is very close to our object.

Another possible source is the Rees-Sciama effect, [120], [119]. An extremely massive and distant superstructure would be a clear candidate to cause a cold and big secondary anisotropy. Even topological defects like global monopoles or textures [183] could have cooled the CMB photons, to produce such spot. Cosmic strings have characteristic scales around arcminutes, hence we do not expect them to be behind this non-Gaussian detection.

CHAPTER 3

Significance, morphology and foreground contribution

The non–Gaussian cold spot in the 1–year WMAP data, described in the previous chapter, is analysed in detail in the present one. First of all, we perform a more rigorous calculation of the significance of the non–zero kurtosis detected in WMAP maps [188] in wavelet space, mainly generated by *the Spot*. We confirm the robustness of that detection, since the probability of obtaining this deviation by chance is 0.69%. Afterwards, the morphology of *the Spot* is studied by applying Spherical Mexican Hat Wavelets with different ellipticities. The shape of *the Spot* is found to be almost circular. Finally, we discuss if the observed non–Gaussianity in wavelet space can arise from bad subtracted foreground residues in the WMAP maps. We show that the flat frequency dependence of *the Spot* cannot be explained by a thermal Sunyaev–Zeldovich effect. Based on our present knowledge of Galactic foreground emissions, we conclude that the significance of our detection is not affected by Galactic residues in the region of *the Spot*. Considering different Galactic foreground estimates, the probability of finding such a big cold spot in Gaussian simulations is always below 1%.

3.1 Introduction

In this chapter we focus on the Gaussianity studies provided in [188] and [43]. These are based on the Spherical Mexican Hat Wavelet (SMHW) technique previously described in this thesis. In [188] an excess of kurtosis was detected convolving the data with the SMHW at scales between 3° and 5°. The deviation

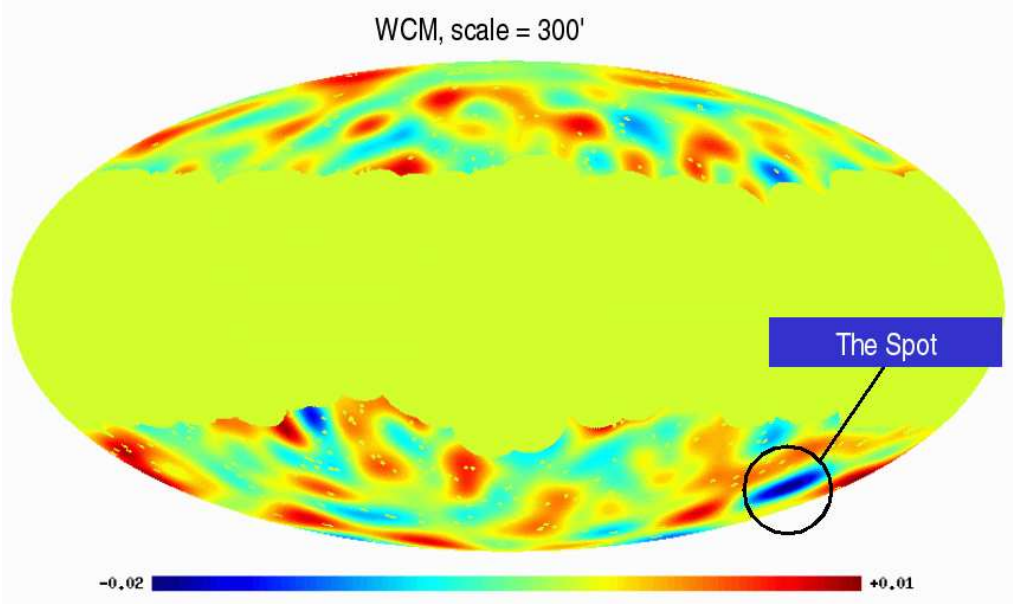

Figure 3.1 The combined and foreground cleaned Q–V–W WMAP map after convolution with the SMHW at scale R_9. The position of *the Spot* is marked.

from Gaussianity presented an upper tail probability of 0.38% considering all the sky and 0.11% in the southern hemisphere, analysing both Galactic hemispheres independently. Performing an analysis of the spots [43], this deviation was found to be due to a cold spot at galactic coordinates ($b = -57°, l = 209°$), called *the Spot* (see Fig. 3.1). Assuming the Gaussian hypothesis, the upper tail probability of having such a spot at a wavelet scale of 5° is 0.18%. These detections were confirmed by other papers, also based on wavelets. The kurtosis analysis of [188] was recalculated in [134] and [126] obtaining similar results. In [32] higher criticism statistics were applied to maps in wavelet space. They detect a deviation from Gaussianity, finding that some pixels of *the Spot* are responsible for it.

One of the aims of this chapter is to re–analyse carefully the robustness of the results in [188]. In this chapter 15 different wavelet scales and two estimators, kurtosis and skewness were considered. Could it be that looking at that many estimators, the deviation from Gaussianity just happened by chance?

Anyway, the origin of non-Gaussian signatures is in general still not clear and controversial. Many scientists just believe that their findings are due to a deficient subtraction of the Galactic foreground emissions, e.g. [35], [180]). Some

others, e.g. [64], argue that foregrounds are unlikely to explain their results.

Considering the non–Gaussianity in wavelet space and related to the very big and cold spot, several possibilities were discussed in [188] and [43], namely systematics, Galactic foregrounds, thermal Sunyaev–Zeldovich effect [173] (hereafter SZ effect), topological defects or gravitational effects [149], [119], [120].

A better knowledge of *the Spot*'s shape can help us to find out its origin. For example, *the Spot* could be explained by considering topological defect models, as suggested in [43]. In this context, if *the Spot* presents circular symmetry, it could have been generated by a texture. Finding out the shape of *the Spot*, can also inform us about a hypothetical gravitational potential that could be generating the non-Gaussian emission. A local second–order gravitational effect was suggested in [181] as a possible origin of *the Spot*. These possibilities will be discussed in future papers.

The easiest explanation assuming the widely accepted Gaussian hypothesis would be a bad foreground subtraction of the data. Hence it should be the first one to be tested. In [188] and [43] several tests were performed to discard the foregrounds as a cause of the detection. The most important test is the frequency dependence of *the Spot*, since the Galactic foregrounds have a strong frequency dependence. The amplitude and the number of pixels of *the Spot* have been shown to have a constant frequency dependence, as expected from a cosmological origin. Nevertheless, some recent works seem to contradict these conclusions. Recently, the non–Gaussianity results obtained with spherical wavelets were analysed in [115], concluding that the most possible source of the non–Gaussian departures, are residual foregrounds. These conclusions do not agree with the results presented in [188] and [43]. Also in [38] was suggested that Galactic foregrounds could be behind our and other non-Gaussian features.

Other different explanations are suggested for the large scale asymmetries and the non-Gaussian behaviour found in wavelet space. In [97] an anisotropic cosmological model, namely the Bianchi type VII_h is assumed. The best fit Bianchi model introduces an additional CMB component, which presents a swirl pattern. Looking at this pattern, a hot and a cold spot can be seen close to the center of the swirl. The cold spot of the best fit model matches *the Spot*. Subtracting the swirl pattern, the significance of the kurtosis deviation and other large scale anomalies are largely reduced. Nevertheless a later work, [98], indicates the incompatibility of the WMAP data with extended Bianchi models including a

dark energy term. A possible incorrect dipole correction is pointed out in [69] as a plausible explanation for some of the observed asymmetries. This hypothesis is under examination but since *the Spot* has a much lower scale than the dipole, we do not expect to be able to explain it in this way.

Considering the relevance of the issue and the present controversial debate, the main part of this work is dedicated to investigate the origin of non–Gaussianity found in wavelet space and, in particular a possible foreground contribution to *the Spot*. Different techniques of foreground subtraction are taken into account.

Data and simulations are described in the previous chapter. In this chapter, the study of the robustness of the non–Gaussian detection in wavelet space is discussed in Section 3.2; the morphology of *the Spot* in Section 3.3; the foreground tests are presented in Section 3.4.

3.2 Robustness of the non–Gaussian detection in wavelet space

It is not trivial at all to determine how significant the non–Gaussian detections are. Almost all analyses define *the Spot* as a highly significant deviation from Gaussianity, but the given significance differs. Our aim in this section is to find the probability of obtaining our observation by chance, assuming that the Gaussian hypothesis is true. This probability is called p–value and will give us the robustness of our findings. The p–value should not be confused with the upper tail probability, which is the cumulated probability above the observed value. Before entering in the discussion, let us summarise the obtained results in previous works.

In the first work, [188] the skewness and the kurtosis of the data were compared with those of 10000 Gaussian simulations, at 15 wavelet scales, between 13.7 and 1050 arcmin.

The deviation of the kurtosis with respect to the Gaussian hypothesis was found to have an upper tail probability of 0.38% at wavelet scale $R_9 = 5^\circ$. Considering the Galactic hemispheres separately, the lowest upper tail probability appears in the southern one and is 0.11% at scale $R_7 = 3.33^\circ$, whereas the northern hemisphere is compatible with Gaussianity.

Afterwards a spot analysis was performed in [43], using the same scales and simulations as in [188]. The considered estimators were: number of spots,

number of maxima and minima, and number of pixels above or below a given threshold (hot or cold area). At the same scales where the kurtosis excess was found in [188] and at high thresholds, the cold area shows up very low upper tail probabilities and the number of cold spots was just one. The lowest probability, 0.18%, was obtained at scale $R_8 = 4.17^\circ$. In this way the cold spot located at ($b = -57^\circ, l = 209^\circ$) was discovered to be the one responsible for the deviation from Gaussianity.

In [43] the area of *the Spot* was compared to the biggest spot of each simulation, but only for scales R_8 and R_9. At these scales all the calculated probabilities were lower than 0.65% (see Table 2 of [43]), being the lowest one 0.18% at scale R_9.

All these upper tail probabilities have been calculated counting how many simulations have higher or equal values of our estimator than the data at *one particular scale*. Since several scales and estimators were considered, these upper tail probabilities do not tell us the p–value, i.e. probability of obtaining our observation by chance assuming that the Gaussian hypothesis is true. We have to bear in mind that considering a large enough number of estimators and scales, the probability of finding non–Gaussian features in any Gaussian simulation would increase significantly.

We should therefore review our calculations. As for the area of *the Spot* only two scales were considered, one could think that this would be the best estimator to calculate the p–value. In all other cases we considered 15 scales and several estimators However in the analyses after the detection of the non-zero kurtosis, the choice of the scales was conditioned by this first finding. In [43] only two scales were considered for the area of *the Spot* because there the kurtosis deviation was the largest. Hence we have to test the robustness with the first detection, the deviation of the kurtosis. This deviation occurs mainly at 3 scales considering all the sky, and at 4 scales considering only the southern hemisphere.

The p–value for the all–sky case, was calculated in [126] using a very conservative approach. They search through 1000 Gaussian simulations to determine the number of maps that have an equivalent or greater deviation than the maximum deviation found in the data. The obtained p–value was 4.97%.

This approach does not take into account that the deviation from Gaussianity occurs at several consecutive scales. As already mentioned, in the all–sky case

scales R_7, R_8 and R_9 present a significant deviation from Gaussianity. The highest upper tail probability of these three scales is 0.67%.

In order to know how likely it is to find such a detection by chance, we have to answer the following question: How many of the 10000 Gaussian simulations, show up a higher or equal deviation in any three consecutive scales, and in any of the two estimators, kurtosis and skewness? This number will give us the p–value. In other words, we have to find how many simulations show skewness or kurtosis values with upper or lower tail probabilities lower than 0.67% in any three consecutive scales. The p–value we obtain is much lower than the previous one and turns out to be 1.91%.

Anyway the most significant upper tail probability of the kurtosis was not obtained in the all–sky case. Considering the northern and southern hemispheres separately the deviation is highly significant at 4 scales, namely $R_6 = 2.5^\circ$, R_7, R_8 and R_9. The highest upper tail probability of these four scales is 0.55%. Now we search through the Gaussian simulations to find how many simulations show skewness or kurtosis values with upper or lower tail probabilities lower than 0.55% in any four consecutive scales and in any of the two hemispheres. The p–value is now 0.69% proving that the kurtosis deviation from Gaussianity is robust.

Dividing the sky into two hemispheres the significance is higher, since the deviation in the kurtosis is due to a localised spot. Anyway we cannot continue dividing the sky in an unlimited number of regions, as the sample variance increases. In our case we are still far away from this limit because each hemisphere contains a large enough number of pixels.

However we should remind that calculating the exact significance of any non-Gaussian analysis is not easy. In our present approach the calculation is more rigorous but with an a-posteriori interpretation, i.e. given the fact that the data deviate from Gaussianity at three consecutive scales, we calculate the probability of obtaining a similar deviation in the simulations. The most important conclusion is that *the Spot* remains statistically robust, independently of the chosen significance test.

orientation	$\rho =$	0.125	0.250	0.375	0.500	0.625	0.750	0.875	1.000
1		-8.14	-9.77	-11.04	-12.89	-14.55	-15.62	-16.09	-16.06
2		-5.49	-8.95	-11.07	-12.62	-13.90	-14.93	-15.65	-16.06
3		-3.60	-6.50	-8.38	-10.59	-12.56	-14.19	-15.37	-16.06
4		-2.37	-4.42	-7.28	-10.44	-12.91	-14.61	-15.62	-16.06
5		-5.67	-8.45	-11.18	-13.38	-15.00	-15.86	-16.16	-16.06
6		-3.35	-5.82	-9.46	-12.63	-14.83	-16.04	-16.33	-16.06

Table 3.1 Minimum temperature (μK) of *the Spot* after convolution of the WCM with the ESMHW at scale $R_8 = 4.17^\circ$.

3.3 Morphology of the Spot

As our detection was performed using the SMHW, which has axial symmetry, *the Spot* is expected to be almost circularly symmetric when observed in wavelet space. By convolving the map with the SMHW, we are in fact amplifying all those underlying signals whose shape is similar to that of the SMHW, whereas other signals are lowered. In particular the zero level is removed with the SMHW since it is a compensated wavelet.

However the shape of *the Spot* could be not completely symmetric. In order to characterise *the Spot*, we should construct an Elliptical Mexican Hat Wavelet on the Sphere (ESMHW) to find out if there is any preferred direction which amplifies even more *the Spot*. Information about the shape of *the Spot* would help us to determine its possible origin. The ESMHW should have the same properties as the SMHW but with an elliptic section instead of a circular one.

The Elliptical Mexican Hat Wavelet on the plane, is a generalisation of the symmetric 2D Mexican Hat Wavelet and therefore is proportional to the Laplacian of an *elliptical* Gaussian function,

$$\begin{aligned} \Psi(x_1, x_2, a, b) &\propto \Delta \exp\left[-\left(\frac{x_1^2}{2a^2} + \frac{x_2^2}{2b^2}\right)\right] \\ &\propto \left[a^2 + b^2 - \left(\frac{b^2}{a^2}{x_1}^2 + \frac{a^2}{b^2}{x_2}^2\right)\right] \\ &\quad \times \exp\left[-\left(\frac{x_1^2}{2a^2} + \frac{x_2^2}{2b^2}\right)\right] \end{aligned} \tag{3.3.1}$$

with two different scales a and b, $0 < b \leq a < \infty$. In order to compare with the

SMHW, we define the scale R, and the axial ratio ρ, as follows

$$R \equiv \sqrt{ab} \tag{3.3.2}$$

$$\rho \equiv \frac{b}{a}, (0 \leq \rho \leq 1). \tag{3.3.3}$$

To obtain the Ellpitical Mexican Hat on the Sphere, we perform the stereographic projection [122] defined by $(\mathbf{x}) \mapsto (\theta, \phi)$

$$x_1 = 2 \tan \frac{\theta}{2} \cos \phi \tag{3.3.4}$$

$$x_2 = 2 \tan \frac{\theta}{2} \sin \phi, \tag{3.3.5}$$

where (θ, ϕ) are the polar coordinates on the sphere. The distance on the tangent plane is given by y that is related to the polar angle (θ) through:

$$y \equiv \sqrt{x_1^2 + x_2^2} = 2 \tan \frac{\theta}{2}. \tag{3.3.6}$$

The Jacobian of the transformation is

$$J = \cos^{-4} \frac{\theta}{2} = \left[1 + \left(\frac{y}{2}\right)^2\right]^2. \tag{3.3.7}$$

Hence we obtain

$$\Psi_S(\theta, \phi, a, b) = \frac{16J}{\sqrt{2\pi N}} \left[a^2 + b^2 - k^2 y^2\right] \exp\left(-r^2 y^2/2\right), \tag{3.3.8}$$

where k, r are defined as follows

$$k = \rho \sqrt{1 - \left(1 - \rho^4\right) \sin^2 \phi} \tag{3.3.9}$$

$$r = b^{-1} \sqrt{1 - (1 - \rho^2) \cos^2 \phi}, \tag{3.3.10}$$

and N is the normalisation constant which has been chosen such that

$$\int d\theta d\phi \sin \theta \Psi_S^2(\theta, \phi, a, b) = 1. \tag{3.3.11}$$

Then we have convolved the ESMHW defined in Eq. (3.3.8) with the combined and foreground cleaned map (WCM). We have chosen eight axial ratios ρ for scale $R_8 = 4.17^\circ$, and six equally spaced orientations of the ESMHW centered on *the Spot*. In Table 3.1 we report the minimum temperature of *the Spot* after the convolution with the different ESMHW.

The value of the minimum temperature depends on how much the underlying signal is amplified. If the spatial distribution of the signal matches the shape of the considered wavelet, the amplification is higher. From Table 3.1 we see that the minimum temperatures for low axial ratios are much lower than the others, for all orientations. The minimum temperature of *the Spot* is reached at axial ratios 1 or 0.875, being the differences between the six orientations small. These results indicate that *the Spot* is essentially circular. Similar conclusions can be obtained for scales R_7 and R_9.

3.4 Foreground contribution to the Non–Gaussian Spot

Our aim in this section is to study possible foreground contributions to the non–Gaussian cold spot. In particular, we will focus on SZ and Galactic foregrounds. Because of their different spectral behaviour respect to CMB, we expect to obtain relevant information from a frequency analysis of *the Spot*.

It is important to remind that, since the convolution with a wavelet is a linear operation, the frequency dependence of a component with no spatial variation in its spectrum, is the same in wavelet space as in real space. Considering that we will perform our analysis in a a small patch of the sky, we assume that there are no significant variations in the spectral index even for synchrotron emission.

3.4.1 The Sunyaev–Zeldovich effect

The SZ effect causes a decrement in the temperature, for frequencies lower than 217 GHz. This effect occurs when CMB photons cross hot electron gas inside a galaxy cluster, suffering inverse Compton scattering, where the electrons transfer energy to the CMB photons. Hence several low frequency photons are promoted to higher frequencies. For the WMAP frequencies, the SZ effect has a negative contribution and has to be considered as a possible source for a very cold spot as the one we are studying.

We already know that the huge size and very low temperature of *the Spot* are very difficult to explain with the SZ effect [43]. In addition there are no observed clusters in this region according to the ACO catalogue [1]. However it is worth checking if the frequency dependence of the SZ effect is compatible with the data, since an unobserved or dark cluster could be present in the mentioned

region of the sky.

In Fig. 3.2 we plot the temperature at the center of *the Spot* ($b = -57^\circ, l = 209^\circ$) at wavelet scale R_8. Since the convolution with wavelets involves many pixels in this region, only one pixel is representative for the entire spot. In the plot we consider the values corresponding to the eight foreground cleaned, individual assembly data: two for the Q and V bands and four for the W–band. We estimate the error bars for these temperatures performing 1000 noise simulations for each of the eight receivers, and convolving them with the SMHW at scale R_8. The standard deviation of the 1000 wavelet coefficients at the chosen pixel plus the corresponding calibration error is the error bar for each receiver.

Fig. 3.2 does not show any evidence for a frequency dependence of the temperature (the same is observed with the area of *the Spot*). In fact, assuming no Galactic contamination in *the Spot*, we find that the CMB fit of the data, i.e. $\Delta T_{CMB} = -16.09 \pm 0.16 \mu$K, has a reduced chi–square of 1.00. In the figure, we also represent the frequency spectrum for thermal SZ effect, that is in thermodynamic temperature

$$\Delta T_{SZ}(\nu) = \left[\frac{h\nu}{k_B} \coth\left(\frac{h\nu}{2k_B T_0}\right) - 4T_0\right] y_c, \tag{3.4.1}$$

where T_0 is the CMB temperature and y_c the Compton parameter. It can be clearly seen that the SZ alone does not fit the data (the reduced chi–square is 9.12). If we perform a CMB+SZ fit, the Compton parameter and hence the SZ effect are compatible with zero. We can conclude that these results strongly discard the SZ hypothesis, whereas the data fit very well to a constant CMB value.

3.4.2 Relevance of Galactic foregrounds in the region of the Spot

In this section we discuss in detail the contribution of Galactic foregrounds in the region of *the Spot*, both in real and in wavelet space. Some authors have suggested that residues of Galactic foregrounds are supposed to be the most likely source for the non–Gaussian behaviour observed in CMB maps obtained from the WMAP data [35]; [115]; [180]. This is because their intensity distribution in the sky is strongly non–Gaussian, and there are still big uncertainties on the Galactic emission at microwave wavelengths. Hence, our aim is to check if this hypothesis is reliable. We focus only on *the Spot* region because, as pointed

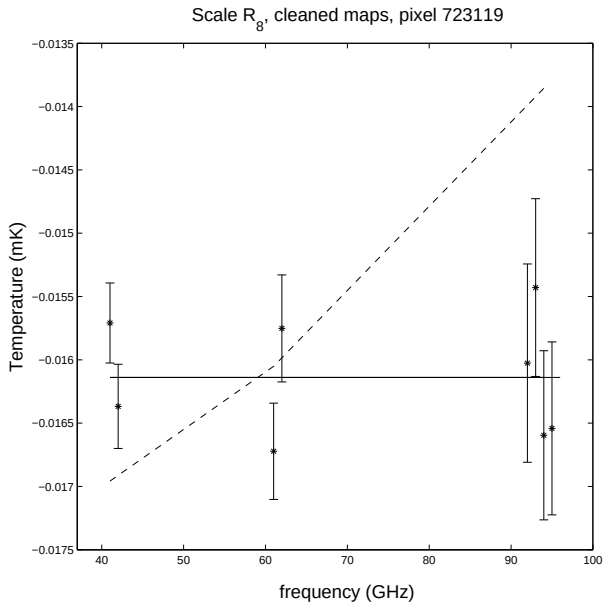

Figure 3.2 The temperature at the center of *the Spot* for channels Q, V and W at Scale R_8. CMB (solid line) and SZ (dashed line) are fitted to the data. The data at the same frequency have been slightly offset in abscissa for readability.

out in [43], deviations from Gaussianity detected by all–sky statistics in wavelet space (like kurtosis, number and area of cold spots) are mainly produced by this region. Excluding *the Spot* area from those analyses makes the WMAP data fully consistent with Gaussianity. The individual peculiarity of *the Spot* is stressed in [43] for its dimension in the sky and for its very "cold" temperature.

To this purpose, we use templates of the different Galactic components in *the Spot* region, extrapolated to the WMAP frequencies. For the **free–free** emission we consider the Hα map of [68], with magnitudes corrected by the Galactic reddening E(B–V) map provided in [157]. The data are converted from Rayleigh to antenna temperature using Eq. 11 of [54], assuming an electron temperature of 7000K. As **synchrotron** template we use the Rhodes/HartRAO 2326–MHz radio survey [99]. At this frequency the contribution of free–free is expected to be low but not negligible and it is subtracted using the Hα map appropriately scaled. Then, the Rhodes survey is extrapolated to higher frequencies by a power law with spectral index -3. This value is in agreement with the average synchrotron spectral index observed in WMAP maps [18], [20]. It is also the average spectral index found between 0.408 and 2.326 GHz in *the Spot* region. Respect to the Haslam map, used by WMAP team, the Rhodes survey

has the advantage of a higher resolution and frequency, providing a more reliable template for synchrotron at cosmological frequencies. Finally we consider the full–sky map of **thermal dust** at 100μK generated in [157], extrapolated to microwaves by the best two–component dust model (model 8) found in [67], hereafter referred as FDS model.

In the last years some works seem to support the existence of spinning dust emission at frequencies around 10–20 GHz [49], [192]. However this emission could provide a significant contribution to the WMAP data only for the K and Ka bands, whereas it quickly decreases at higher frequencies, becoming negligible for the V and W bands [58]. Therefore, we neglect this emission because, even if a contribution of spinning dust was present in the Spot region at K and Ka bands, it would not affect the following analysis.

At the moment, the non–Gaussianity tests have been performed on the combined and foreground cleaned Q–V–W map (WCM). In this map the Galactic signal is removed by fitting simultaneously a set of external foreground templates to the residual Q–V–W maps [18]. However, in the literature, other techniques have been employed to subtract Galactic foregrounds from WMAP maps and to produce clean CMB maps. Therefore, using different and independent maps can give us a further test to verify that the non–Gaussian deviations observed in [188] and [43] are not dependent on the foreground–subtraction technique. For example, in [18] a clean map was produced by a weighted internal linear combination (ILC) of the five frequency WMAP maps. In this way, the resulting CMB map does not rely on external foreground templates, but assumes that there are no spatial variations in the frequency spectrum of each component and introduces complex noise properties. Following the same idea, in [178] a CMB map is provided by an internal linear combination with weights depending on frequency, latitude and angular scales. They found a good agreement with the ILC map at large angular scales and no excess of power at $\ell < 100$ due to foregrounds. However also the TCM map presents complex noise properties [62]. [178] derived also a Wiener filtered map. This map was built for visualization purposes, as a best guess of how CMB looks like, and is not an unbiased map.

Finally, a description of how to build MEM foreground estimates is given in [18], even if they suggest not to apply the MEM solutions directly to CMB analyses because of their complicated noise and signal correlations. We obtain a

MEM cleaned map, adding the eight not cleaned individual assembly maps, for channels Q, V and W, and subtracting the MEM foreground estimates for all these channels.

The WCM and ILC maps are not completely independent, as the latter has been used in the foreground subtraction of the WCM map. Therefore, we shall focus on WCM and TCM maps, i.e. the two independent and most reliable CMB maps (leaving the ILC, Wiener and MEM solutions only as complementary test in wavelet space, where the signal to noise ratio is higher).

The Spot in real space

Although the non–Gaussian deviations described in [188] and [43] are only observed in wavelet space, our starting point is to study foreground behaviours of *the Spot* region in real space. In [43] most important features found in real space were four prominent cold spots with an amplitude higher than 2 times the dispersion of the map. Their size, amplitude and position can be found in Table 4 of [43]. Several tests have been performed in order to find non–Gaussian features of *the Spot*, considering the total cold area in the region and the four resolved spots. However, all the tests give results compatible with Gaussianity. Neither the total area in the region nor the four resolved spots are particularly cold or big, compared to the simulations.

Fig. 3.3 shows a $22^\circ \times 22^\circ$ area of the WCM centered at *the Spot*, as well as the foreground templates scaled to the Q band. In the foreground templates we do not observe any significant correlation with the WCM. What can be noticed is that all three foreground emissions are low in the region of *the Spot*. This means that after the convolution with the SMHW the foreground contribution will be negative in this region.

In Fig. 3.4 we plot the expected mean and rms contribution of Galactic foregrounds at the five WMAP frequencies in *the Spot* region (extrapolating the templates as described above), compared to the WCM and TCM CMB estimates. The values in Fig. 3.4 are in antenna temperature and the region of *the Spot* is defined by a circle of 10° radius. If we focus on the total intensity (left plot), the synchrotron emission (dot–dashed lines) is clearly the dominant Galactic component at K and Ka bands, and it is still higher than the free–free emission (dashed lines) in the Q band. On the contrary, when the rms amplitude of the

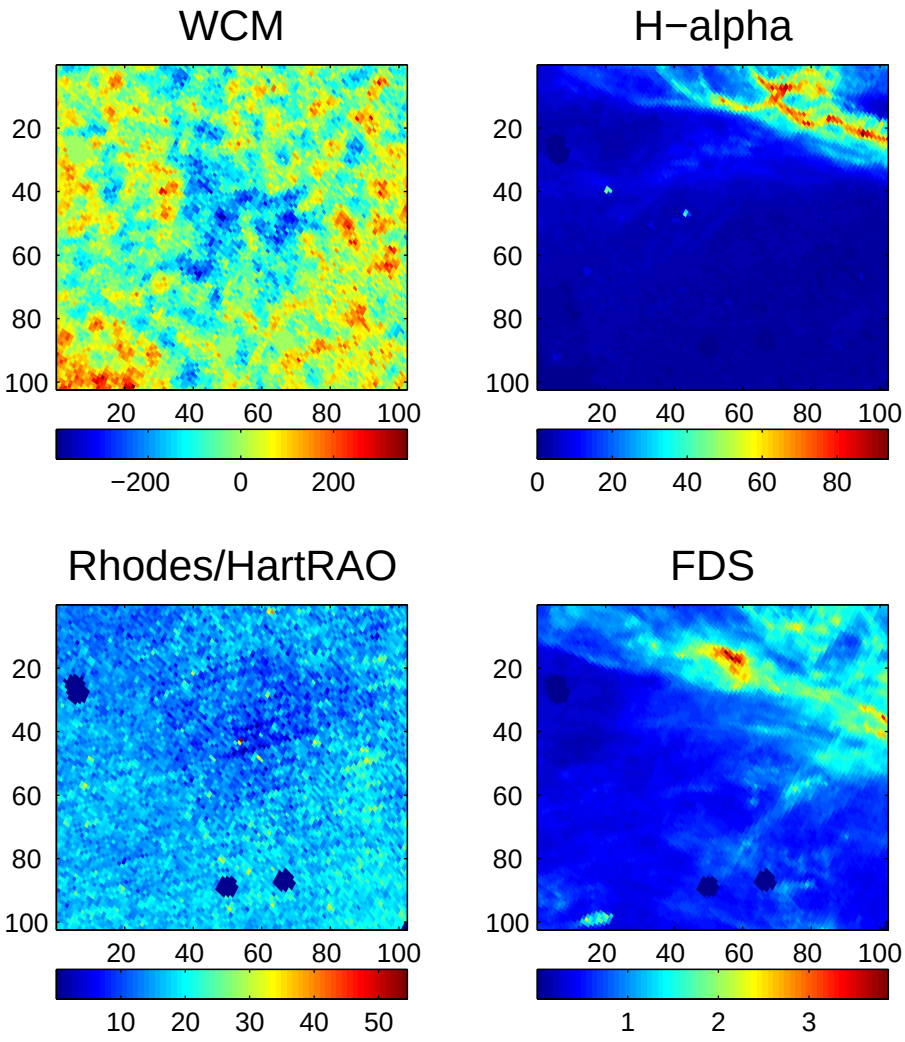

Figure 3.3 Image showing an azimuthal projection of a $22^\circ \times 22^\circ$ patch from HEALPix maps with resolution nside = 256, in the region of *the Spot*. From top to bottom and left to right, we have: the WCM map where *the Spot* can be seen; the H-alpha map; the Rhodes/HartRAO 2326–MHz radio survey; and the FDS dust template. The three foreground templates are scaled to channel Q, where the foreground contribution is higher than in the V and W bands. The maps are in μK units and the labels on the axes are in pixels of size 13.3 $\times$ 13.3 arcmin and the y–axis is oriented in the Galactic North-South direction.

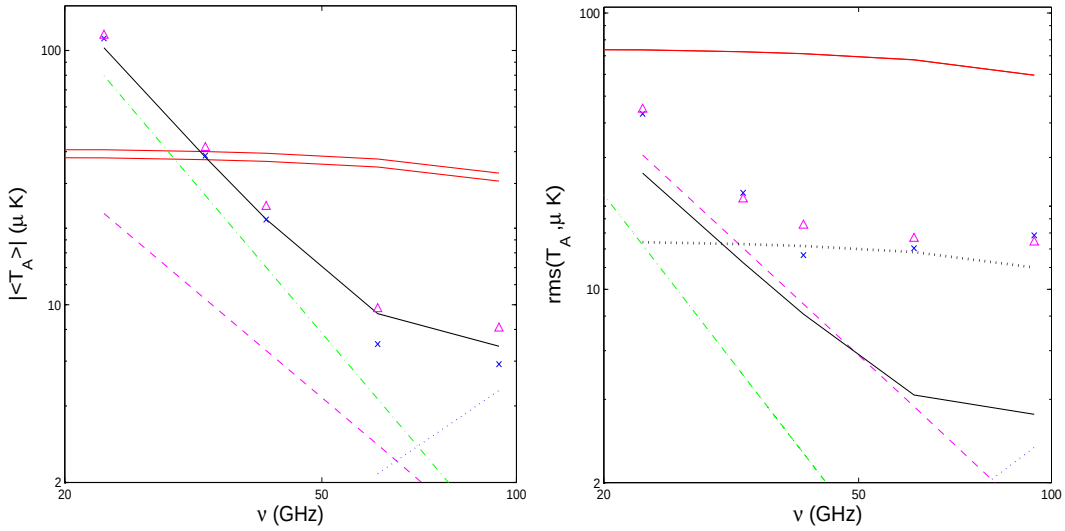

Figure 3.4 Average temperature (left plot) and rms (right plot) in *the Spot* region, as function of frequency. **Foregrounds**: synchrotron (dot–dashed line), free–free (long–dashed line), dust (small dots), total Galactic signal (solid dark line). **CMB** (solid light lines). **Residual maps**: WCM (crosses), TCM (triangles). **Noise** (big dots).

signal is taken into account, the free–free emission becomes dominant respect to the synchrotron at all the WMAP frequencies. This means that in *the Spot* region, synchrotron emission is brighter than free–free but much more uniformly distributed. Since in wavelet space uniform components are erased, we expect the free–free radiation to be the dominant foreground in wavelet space. Anyway, compared to the total rms signal in WMAP maps, the Galactic foreground contribution seems to be relevant only at K and Ka bands, whereas at higher frequencies its rms amplitude is always lower than the WMAP rms noise and at least one order of magnitude lower than CMB. The contribution of dust emission, according to the FDS model, is very small, also at 94 GHz where it is the most relevant Galactic foreground.

In order to compare with the CMB maps, we subtract the WCM and the TCM from the not–cleaned WMAP data at each channel: the resulting maps should include only foregrounds plus noise. The two residual maps provide nearly the same average and rms value at all the frequencies, in a very good agreement with our foregrounds (or foregrounds+noise) estimate. This is particularly evident at the low bands K and Ka, where Galactic foregrounds are more relevant. This is not surprising for the WCM case, because it is based on the same templates for the dust and free–free emission as our estimation (although the syn-

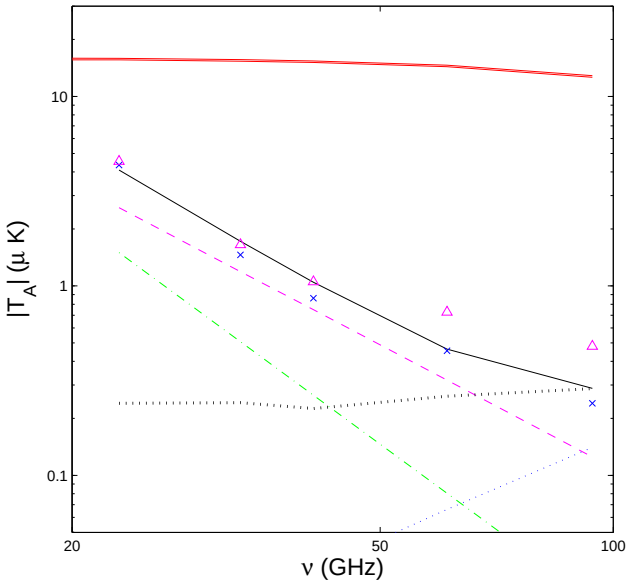

Figure 3.5 As in Fig. 3.4 but for the temperature at the center of *the Spot* in wavelet space.

chrotron template is different). On the other hand, the agreement with the TCM map confirms that the extrapolation of foreground templates is quite reliable. Therefore, WCM and TCM methods seem to provide a good estimate of CMB in *the Spot* region in spite of their completely different technique to subtract foregrounds.

The Spot in wavelet space

We know that wavelets are able to amplify hidden non–Gaussian features, lowering the noise and removing constants. What can be deduced from the results in [188] and [43] is that there is a spatial temperature variation in this region which matches surprisingly well the shape of the SMHW, increasing its relative signal respect to foregrounds and noise in wavelet space.

The contribution of foregrounds, already very low in the real space, is still reduced in wavelet space: it can be appreciated in Fig. 3.5, where we plot the antenna temperature at the center of *the Spot* at scale R_8.

Note that we plot absolute values because the CMB and foregrounds temperatures are negative at the center of *the Spot*. In wavelet space the foregrounds can show negative temperatures since the convolution with compensated wavelets

removes the zero level. This means that also the foreground emissions at the center of this region are lower than their average emission in the region (see Fig. 3.3). Comparing the mean temperature in real space with the temperature at the center of *the Spot* in wavelet space, we find that, while the CMB value is reduced by a factor ~ 5, the foreground signal is now a factor between 7 and 12 lower. This is a confirmation of goodness of an analysis in wavelet space. Also the noise is strongly reduced and is always lower than the expected foreground signal, which is clearly dominated by free–free emission. Finally, as in previous figures, we show the residual temperature after subtraction of different CMB maps from WMAP data. They are in a good agreement with our foregrounds estimation.

The region of *the Spot* in the WCM is shown in Fig. 3.6 as it appears in wavelet space at scale R_8. Moreover, we report also the images of foreground templates, scaled to the Q band. The distribution of foregrounds temperature in wavelet space does not show any correlation with *the Spot* in CMB maps, although the center of this region corresponds always to a negative value. The only foreground whose spatial distribution resembles in some way the CMB spot is the synchrotron emission. However it is very unlikely that a residue of a signal which is two orders of magnitude lower than the total signal could be responsible for the observed deviation from Gaussianity.

Can Galactic residues explain the non–Gaussian Spot in wavelet space?

Even if it seems unlikely from the previous sections, we investigate now the possibility that a foreground residue in CMB maps could explain the non–Gaussian signal found in wavelet space [188] and [43]. These papers performed several tests in order to investigate if foregrounds can affect the results, but no evidence of it has been found out. On the contrary, different arguments seem to discard foregrounds as sources of the non–Gaussian signal in WMAP CMB data: 1) the most significant one is probably the lack of frequency dependence both in the kurtosis and in properties of *the Spot*; 2) *the Spot* is located in a region with very low foreground emission, and their relative contribution is reduced when we go from real space (where no deviations from Gaussianity are found) to wavelet space; 3) similar results are found using totally independent techniques to subtract foregrounds (e.g., WCM and TCM maps; see next paragraphs). Let us see now more details for the different involved estimators.

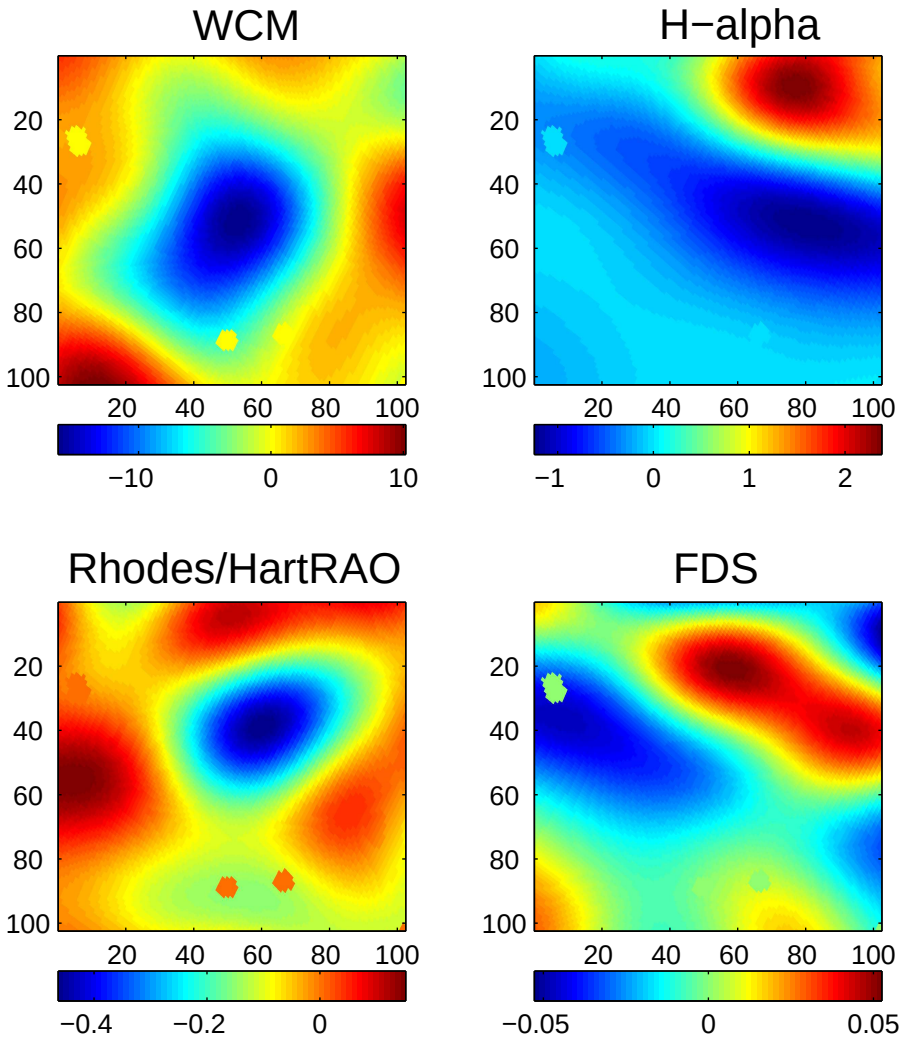

Figure 3.6 In this figure we show a $22^\circ \times 22^\circ$ square centered at the minimum of *the Spot*, for different maps at scale $R_8 = 4.17^\circ$. The same maps as in Fig.3.3 are shown, again scaled to channel Q, in the same units. Only the weak synchrotron emission shows some correlation with *the Spot*, but its amplitude is two orders of magnitude lower than *the Spot*. Therefore we do not expect it to be responsible for the observed deviation from Gaussianity. Note that in all figures we see three small spots which correspond to masked point sources.

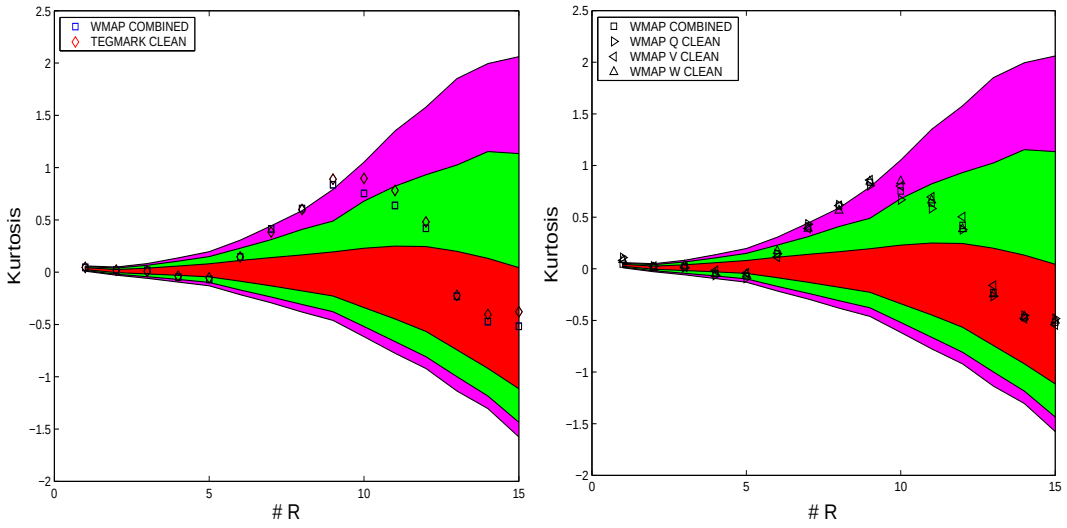

Figure 3.7 Comparison between kurtosis found in WCM and TCM clean maps (left plot). In the right plot we compare the kurtosis values of the Q, V and W bands with the WCM. The acceptance intervals for the 32% (inner), 5% (middle) and 1% (outer) significance levels, given by the 10000 simulations are also plotted. Note that the figure on the right is similar to Fig. 7 in [188], but the Q map values have been corrected since they were slightly different due to an error in the construction of the Q map.

Kurtosis: this statistic has been deeply investigated in [188]. Here we want only to stress some points. Contrary to what is expected if foregrounds contamination is relevant, the distribution of kurtosis as function of wavelet scales has the same pattern and amplitude in the WCM as well as in each single band Q, V and W (see Fig.3.7, right plot). Moreover, a similar shape for the kurtosis distribution has been obtained from the TCM map (see Fig. 3.7, left plot). The only relevant difference is noticed at the peak of the distribution, where the amplitude of the kurtosis is higher, meaning an even more significant deviation from Gaussianity.

Temperature at the center of the Spot: in wavelet space at scale R_8, *the Spot* presents an extremely negative temperature in its minimum. Considering the WCM, the minimum has a temperature of $\sim -16.1\mu$K, nearly 4.6 times the dispersion of that map. Considering 10000 Gaussian CMB simulations, the probability of finding a minimum of such amplitude or less at scale R_8, is 0.75%. No particular frequency dependence has been observed. In Table 3.2 the temperature at the center of *the Spot* is also reported for the combined not–cleaned WMAP map, (hereafter WNCM), and for maps cleaned by different techniques.

Map	$T(\mu K)$	$\sigma(\mu K)$	$n_\sigma = T/\sigma$	upper tail probability
1% limit			-4.52	1.00%
WNCM	-16.39	3.55	-4.62	0.61%
WCM	-16.12	3.52	-4.58	0.75%
TCM	-15.84	3.47	-4.56	0.82%
ILC	-16.30	3.54	-4.61	0.63%
WFM	-13.87	3.01	-4.61	0.61%
MEM map	-16.48	3.53	-4.67	0.44%
Local subtraction	-15.63	3.52	-4.44	1.32%

Table 3.2 Temperature at the center of *the Spot* for different maps at scale R_8. The values are expressed in thermodynamic temperature and in terms of the dispersion of the corresponding map. The last column gives the probability of having a lower or equal minimum temperature under the Gaussian hypothesis. The "1% limit" is given by the simulation whose minimum temperature has 1% upper tail probability compared to the 10000 Gaussian simulations.

The WNCM is obtained by combining the not cleaned data in the same way as the WCM. We estimate the significance of the deviation from Gaussianity and we find that it is always below the 1% upper tail probability, independently of the technique used to subtract Galactic foregrounds.

Nevertheless, the difference in temperatures between the observed temperature and the one giving an upper tail probability of 1% are $\approx 0.2\mu$K for TCM and WCM maps, lower or of the same order than noise and foregrounds contribution (see Fig. 3.5). We can conclude that this test gives a less robust non–Gaussian detection compared to kurtosis and area tests. For example, subtracting our Galactic signal estimate in *the Spot* region, from the WNCM, we see that the upper tail probability is slightly above 1%. As in this case we do not know the σ of the cleaned map, since our estimation is local, we use the σ of the WCM map (see the last row of Table 3.2).

Area of the Spot: a stronger deviation from Gaussianity is observed from the dimension of *the Spot* area. Considering only pixels with lower temperatures than 3 times the dispersion of the map, *the Spot* covers a region of the sky of diameter $\approx 8^\circ$ at wavelet scale R_8. Based on the WCM map, the analysis in [43] showed that the probability of having a spot as big as this one in Gaussian

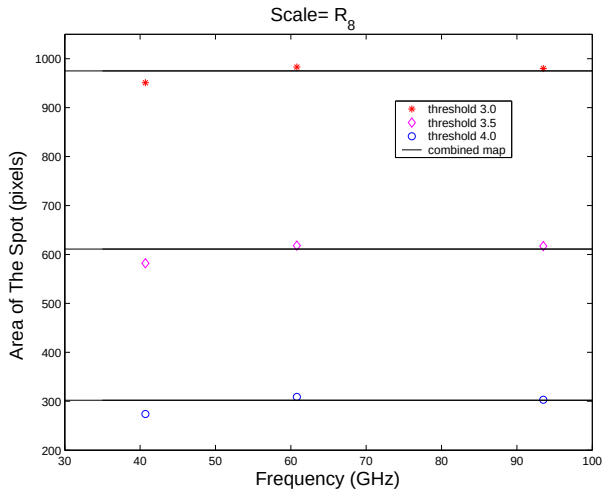

Figure 3.8 Frequency dependence of the area of *the Spot*, at thresholds 3.0 (asterisks), 3.5 (diamonds) and 4.0 (circles), at scale R_8. The horizontal lines represent the combined map values. The area is almost frequency independent. Note that this figure is similar to Fig. 11 in [43], but the Q map values have been corrected since they were slightly lower due to an error in the construction of the Q map.

simulations is always smaller than 0.65% for thresholds between 3 and 4.5σ. Moreover, the area of *the Spot* has a similar dimension at all the WMAP frequencies. This can be observed in Fig. 3.8. We report in Table 3.3 the dimension in pixels of *the Spot* area in the different clean maps with the corresponding upper tail probability: for all the considered maps, this probability is around 0.2–0.4%. Contrary to the minimum temperature estimator, if we subtract our local foreground estimate from the not cleaned maps, the upper tail probability of the detection still remains widely below 1%. Even if two times the estimate is subtracted, the upper tail probability is still around 1%. However the strong frequency dependence of this map in Q–V–W bands is incompatible with the observations (see Table 3.4). If we try to explain *the Spot* as a combination of CMB plus bad subtracted foregrounds, the frequency dependence must be flat once the contaminating foregrounds are subtracted.

Finally, we discuss the possibility of having a residual foreground contamination in the clean WMAP maps that is constant at the Q, V and W bands. Because of their opposite spectral behaviour, we can find a linear combination of free–free and dust emission with a small variation between 40 and 94 GHz. We consider the possibility that the foreground amplitude estimated from the

Map	$\sigma(\mu K)$	$N_{pixels}(T > 3\sigma)$	upper tail probability
1% limit		831	1.00%
WNCM	3.55	990	0.32%
WCM	3.52	975	0.34%
TCM	3.48	970	0.36%
ILC	3.54	1023	0.22%
WFM	3.01	984	0.33%
MEM	3.53	1011	0.26%
Local subtr.	3.519	924	0.45%

Table 3.3 Area and significance of *the Spot* for different maps at scale R_8. The areas are the number of pixels colder than three times the standard deviation of the corresponding map. The first row of the table stands for the simulation whose biggest spot presents a 1% upper tail probability compared to the biggest spot of each of the 10000 simulations.

templates is significantly underestimated. Assuming free–free to be underestimated by a 20% and dust by a 120%, we obtain a nearly constant residue. In this case, the total residue would be 0.19, 0.14 and 0.20μK at 41, 61 and 94 GHz respectively. These values are not incompatible with possible errors in templates and in their extrapolation to microwave frequencies [54]; [67]. Now, our local foregrounds estimate plus the constant residue is subtracted from the unclean spot region. Results are reported in Table 3.4. Even subtracting two times the flat residue, we do not obtain any relevant reduction in the significance of the non–Gaussian detection(see last two rows in Table 3.4).

Map/Band	Q	V	W
Local subtraction	909	947	949
2×Local subtraction	763	886	909
Local + flat residue subtr.	878	926	923
Local +2×flat residue subtr.	860	915	903

Table 3.4 Area of *the Spot* (in pixels) after local subtraction of foregrounds. The only time where the significance of the area can be reduced below the 1% limit (831 pixels) occurs subtracting two times the local foreground estimation at the Q band. However the remaining spot shows a clear frequency dependence which can not correspond to a clean CMB spot. The other three cases show an almost flat cleaned spot, but its size is higher than the 1% limit given by the Gaussian simulations.

CHAPTER 4

The non-Gaussian Cold Spot in the 3-year WMAP data

The non-Gaussian cold spot detected in wavelet space in the WMAP 1–year data, is detected again in the coadded WMAP 3–year data at the same position ($b = -57^\circ, l = 209^\circ$) and size in the sky ($\approx 10^\circ$). The present analysis is based on several statistical methods: kurtosis, maximum absolute temperature, number of pixels below a given threshold, volume and Higher Criticism. All these methods detect deviations from Gaussianity in the 3–year data set at a slightly higher confidence level than in the WMAP 1–year data. These small differences are mainly due to the new foreground reduction technique and not to the reduction of the noise level, which is negligible at the scale of the spot. In order to avoid *a posteriori* analyses, we recalculate for the WMAP 3–year data the significance of the deviation in the kurtosis. The skewness and kurtosis tests were the first tests performed with wavelets for the WMAP data. We obtain that the probability of finding an at least as high deviation in Gaussian simulations is 1.85%. The frequency dependence of the spot is shown to be extremely flat. Galactic foreground emissions are not likely to be responsible for the detected deviation from Gaussianity.

4.1 Introduction

The recently released 3–year WMAP data with higher signal to noise ratio is key to confirm or disprove the anomalies found in the 1-year WMAP data.

In the 3–year papers, the WMAP team [90] re-evaluates potential sources of

systematic errors and concludes that the 3–year maps are consistent with the 1–year maps. The exhaustive polarization analysis enhances the confidence on the accuracy of the temperature maps. The ΛCDM model continues to provide the best fit to the data.

A Gaussianity analysis of the 3–year data is performed in [171]. No departure from Gaussianity is detected based on the one point distribution function, Minkowski functionals, the bispectrum and the trispectrum of the maps. The authors do not re-evaluate the other statistics showing asymmetries or non–Gaussian signatures in the 1–year data.

The aim of this chapter is to check the results of the previous chapters and [188], [43], [32], [44]. All these analyses were based on wavelet space. In particular the data were convolved with the Spherical Mexican Hat Wavelet (SMHW). Convolution of a CMB map with the SMHW at a particular wavelet scale increases the signal to noise ratio at that scale. Moreover, the spatial location of the different features of a map is preserved.

An excess of kurtosis was detected in the 1–year WMAP data [188] compared to 10000 Gaussian simulations. This excess occurred at wavelet scales around 5° (angular size in the sky of $\approx 10^\circ$). The excess was found to be localized in the southern Galactic hemisphere. A very cold spot, called *the Spot*, at galactic coordinates ($b = -57^\circ, l = 209^\circ$), was pointed out as the possible source of this deviation.

In chapter 2 we showed that indeed *the Spot* was responsible for the detection. The number of cold pixels below several thresholds (cold Area) of *the Spot* was unusually high compared to the spots appearing in the simulations. Compatibility with Gaussianity was found when masking this spot in the data. The minimum temperature of *the Spot* was as well highly significant.

In chapter 3 we confirmed the robustness of the detection and analysed the morphology and the foreground contribution to *the Spot*. *The Spot* appeared statistically robust in all the performed tests, being the probability of finding a similar or bigger spot in the Gaussian simulations less than 1%. The shape of *the Spot* was shown to be roughly circular, using Elliptical Mexican Hat Wavelets on the sphere. Moreover the foreground contribution in the region of *the Spot* was found to be very low. *The Spot* remained highly significant independently of the used foreground reduction technique. In addition the frequency dependence of *the Spot* was shown to be extremely flat. Even considering large errors

in the foreground estimation it was not possible to explain the non-Gaussian properties of *the Spot*.

Higher Criticism statistics (hereafter HC) were applied to the 1–year maps [32] after convolving them with the SMHW. This method provided a direct detection of *the Spot*. The HC values appeared to be higher than 99% of the Gaussian simulations.

Note that although *the Spot* has not been detected in real space, this structure exists but is hidden by structures at different scales. The convolution with the SMHW at the appropriate scale, amplifies *the Spot*, making it more prominent.

Several attempts have been made in order to explain the non-Gaussian nature of this cold spot. According to [181] local second–order gravitational effects could produce *the Spot*. In [95] the possibility of explaining *the Spot* and other large scale anomalies by local compensated voids was considered. In [97] and [33] an anisotropic Bianchi VII_h model was assumed, showing that it could explain the excess of kurtosis and the HC detection as well as several large scale anomalies. On the other hand, A further work [129] still detects non-Gaussianity in the Bianchi corrected maps. The analysis in [98] proved the incompatibility of the extended Bianchi models including the dark energy term with the 1–year data. A finite cosmology model which would explain *the Spot* and the low multipoles in the angular power spectrum has been developed in [2]. Up to date there are no further evidences of the validity of any of the above suggested explanations.

Our paper is organized as follows. We discuss the changes in the new WMAP data release and the simulations in Section 4.2. The analysis using all the mentioned estimators is described in Section 4.3. In Section 4.4, the significance of our findings is discussed. We analyse the frequency dependence of *the Spot* in Section 4.5, and our discussion is presented in Section 4.6.

4.2 WMAP 3–year data and simulations

Most of the 1–year Gaussianity analyses were performed using the WMAP combined, foreground cleaned Q–V–W map (hereafter WCM) described in the introduction of this thesis. CMB is the dominant signal at these bands and noise properties are well defined for this map. The de-biased Internal Linear

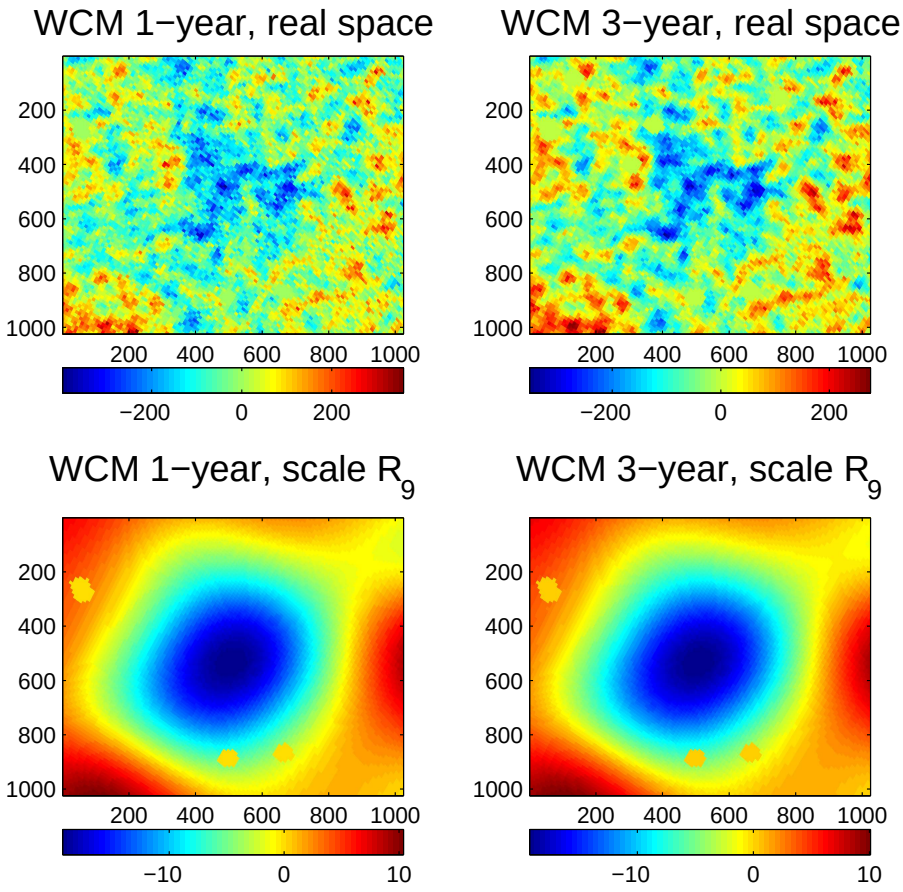

Figure 4.1 Image showing an azimuthal projection of a $22^\circ \times 22^\circ$ patch from the WCM HEALPix map with resolution nside = 256, centered on *the Spot* and in μK. In the first row we have the 1–year and 3–year images of *the Spot* in real space, whereas in the second row *the Spot* is shown at wavelet scale R_9. The image is divided in 1024×1024 pixels and the y-axis is oriented in the Galactic north-south direction.

Combination map, (DILC) proposed by the WMAP team, estimates the CMB on the whole sky. However its noise properties are complicated and regions close to the Galactic plane will be highly contaminated by foregrounds. Furthermore, evidences for the foreground contamination of the DILC are found in [36]. Therefore we will still use the more reliable WCM in the 3–year data analysis. Some changes of the 3–year temperature analysis with respect to the 1–year one are described in [90]. Coadding the three years of observations reduces the instrumental noise. The 3–year maps have ≈ 3 times lower variance. Refinements in gain calibration and beam response models have been implemented and a new foreground reduction technique has been used. The latter

seems to provide a better correction than the one applied to the first year data. As discussed in [44] the Galactic foreground estimation is a very important issue in Gaussianity analyses. The exclusion masks defined in [18] have not been modified, except for the inclusion of 81 new point sources in the kp0 mask. This mask excludes the highly contaminated pixels close to the Galactic plane.

Despite these changes the 3–year maps have been found to be consistent with the 1–year maps by the WMAP team.

A very careful analysis was perfomed [188], [43] in order to study the power spectrum and noise dependence of the kurtosis and cold Area estimators. Considering different power spectra within the 1σ error band of the 1–year data, the differences in the significance of the kurtosis were found to be negligible (see Figure 11 in [188]). The Area of a particular spot was neither affected by the power spectrum (see section 5.3 in [43]). The results were almost noise independent. The convolution with the SMHW reduces considerably the noise contribution. Even if similar results are expected, we perform 10000 Gaussian simulations of the 3–year coadded data following the same steps as for the 1–year simulations. The only differences between the 3–year and the 1–year simulations are a lower noise contribution and a very slight variation in the power spectrum used to generate the simulations. For a detailed description of the simulation pipeline, see section 2 of [188].

4.3 Analysis

Our aim in this section is to repeat the same tests performed in [188], [43], [32] and [44] but with the 3–year data. Then we will compare the new results to the old ones. One can see the region of *the Spot* in real and wavelet space at scale 5° for both releases of the WMAP data in Figure 4.1. In real space the 3–year data image appears clearly less noisy, whereas the wavelet space images present only very small differences.

In [188], data and simulations were convolved with the SMHW at 15 scales, namely ($R_1 = 13.7$, $R_2 = 25$, $R_3 = 50$, $R_4 = 75$, $R_5 = 100$, $R_6 = 150$, $R_7 = 200$, $R_8 = 250$, $R_9 = 300$, $R_{10} = 400$, $R_{11} = 500$, $R_{12} = 600$, $R_{13} = 750$, $R_{14} = 900$ and $R_{15} = 1050$ arcmin). We will use the same 15 scales in our present analysis, considering those estimators where non-Gaussianity was found in the 1–year data, namely kurtosis, Area, *Max*, HC and a new one, the volume. The defi-

nitions of each estimator will be given in the following subsections. Analyses were also performed in real space, which will be referred as wavelet scale zero. In real space, the data are found to be compatible with Gaussian predictions

In the following subsections we will give the upper tail probabilities of the data at one particular scale. The upper tail probability is the probability that the relevant statistic takes a value at least as large as the one observed, when the null hypothesis is true.

In section 4.4 we will give a more rigorous measure of the significance, considering the total number of performed tests to calculate the p-value of *the Spot*. The p-value is the probability that the relevant statistic takes a value at least as extreme as the one observed, when the null hypothesis is true. In our case, the null hypothesis is the Gaussianity of the temperature fluctuations.

4.3.1 Kurtosis

Given a random variable X, the kurtosis κ is defined as $\kappa(X) = \frac{E[X^4]}{(E[X^2])^2} - 3$. In [188] the kurtosis of the wavelet coefficients was compared to the acceptance intervals given by the simulations. In Figure 4.2 the kurtosis of the 1–year data are represented by asterisks and the 3–year data by circles. Hereafter we will use these symbols to represent 1–year and 3–year data. Both are plotted versus the 15 wavelet scales. Scale 0 corresponds to real space. The acceptance intervals given by the simulations will be plotted in the same way in all figures: the 32% interval corresponds to the inner band, the 5% interval to the middle band and the 1% acceptance interval, to the outer one. As expected, the acceptance intervals remain almost unchanged with respect to those obtained from 1–year simulations. This will happen as well for all the other estimators. The 3–year kurtosis values follow the same pattern as the 1–year ones, confirming the initial results. However there are slight differences at the scales where the deviation is detected, being the kurtosis even higher in the 3–year data. The most significant deviation from the Gaussian values, occurs at scale $R_9 = 5^\circ$. In Table 4.1 we list the kurtosis values at scale R_9, considering the 1–year data as published in 2003, the 1–year data release applying the changes in the data analysis described in [90], and the coadded 3–year data. The biggest difference is found between both releases of the 1–year data. The kurtosis value of the 1–year data increases $\approx 7\%$. This may be due to the new foreground reduction technique. As expected the noise reduction due to coadding the three years

Data	kurtosis	probability
1–year data (2003)	0.836	0.38%
1–year data (2006)	0.895	0.28%
3–year data	0.915	0.23%

Table 4.1 Middle column: kurtosis values at scale R_9 for different maps. Right column: probability of obtaining a higher or equal kurtosis value in Gaussian simulations.

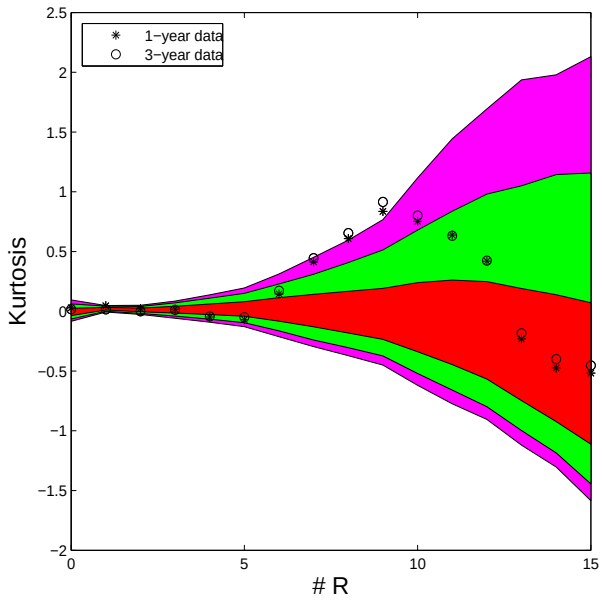

Figure 4.2 WCM kurtosis values for the 1–year (asterisks) and the 3–year data (circles). The acceptance intervals for the 32% (inner), 5% (middle) and 1% (outer) significance levels, given by the 10000 simulations are also plotted.

of observations, implies a much lower increase in the kurtosis, since the noise contribution in wavelet space is very small. The upper tail probabilities (i.e. the probabilities of obtaining higher or equal values assuming the Gaussian hypothesis) are given in the right column of Table 4.1. Hereafter we will compare the first release of the 1–year data with the 3–year data.

Analysing both Galactic hemispheres separately, we obtain the results presented in Figure 4.3. Again the kurtosis follows the same pattern as in the 1–year results. As expected, the deviation appears only in the southern hemisphere and it is slightly higher in the 3–year data. The upper tail probability obtained in [188] was 0.11% at scale R_7 in the southern hemisphere, whereas now we have 0.08% again at scale R_7. The deviation from Gaussianity is localised in the

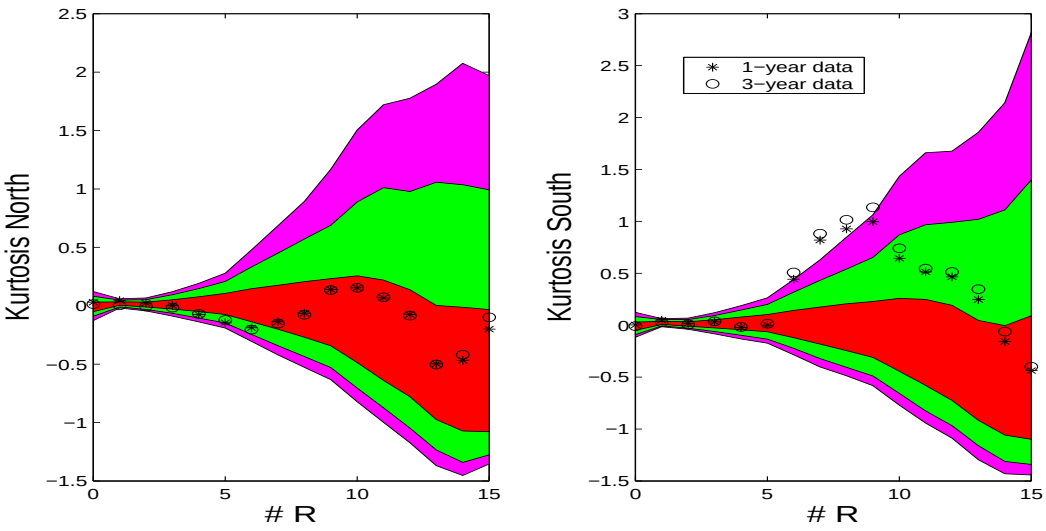

Figure 4.3 As in Figure 4.2 but for the northern (left plot) and southern (right plot) Galactic hemispheres.

southern hemisphere because *the Spot* is responsible for it (see [43]).

4.3.2 Maximum statistic

Given n individual observations X_i, Max is defined as the largest (absolute) observation :

$$Max_n = max\{|X_1|, |X_2|, \ldots, |X_n|\}.$$

The very cold minimum temperature of *the Spot*, was shown to deviate from the Gaussian behaviour in [188]. In this work and in [43], [44] the minimum temperature estimator was used to characterise *the Spot* whereas in [32] the chosen estimator was Max. As Max is a classical and more conservative estimator, we will use it in the present paper instead of the minimum temperature. Our n observations correspond to values in real or wavelet space (normalized to zero mean and dispersion one). *The Spot* appears to be the maximum absolute observation of the data at scales between 200 and 400 arcmin. In Figure 4.4, the 1–year and 3–year WMAP data values of Max are compared to those obtained from the simulations. As for the kurtosis, both data releases show very similar results. The data lie outside the 1% acceptance interval at scales R_9 and R_{10}. The 3–year data show slightly higher values than the 1–year data at these scales. In particular, the upper tail probability for the 1–year data was 0.56%, whereas for the 3–year data we obtain 0.38% at scale R_9.

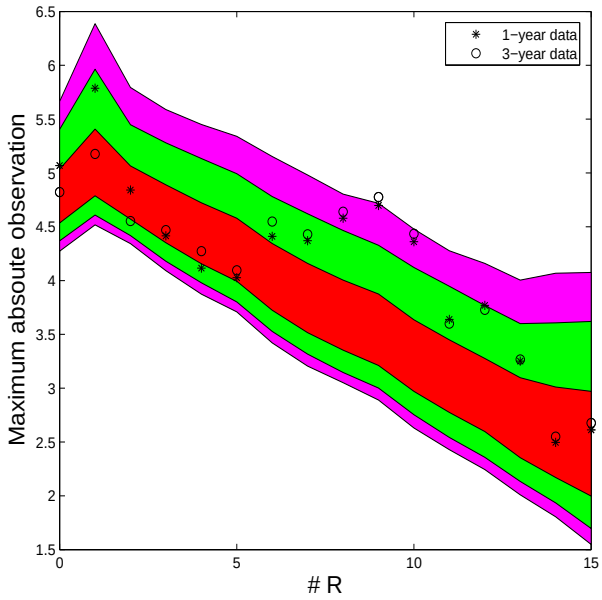

Figure 4.4 Maximum absolute observation versus the 15 wavelet scales. Again the circles represent the 3–year data and the asterisks the 1–year data. The bands represent the acceptance intervals as in previous figures.

4.3.3 Area

We define the hot Area as the number of pixels above a given threshold ν and the cold Area as the number of pixels below a given threshold $-\nu$. The threshold is given in units of the dispersion of the considered map.

In [43] the total cold Area of the 1–year data was found to deviate from the Gaussian behaviour at scales R_8 and R_9 and thresholds above 3.0 (see Figures 1 and 2 in [43]).

The large cold Area of *the Spot* was found to be responsible for this deviation [43]. Such a big spot was very unlikely to be found under the Gaussian model at several thresholds (see Table 2 of [43]).

In the present paper we will define the Area as the maximum between hot and cold Area at a given threshold and scale. As for the *Max* estimator, we obtain in this way a more conservative estimator since *the Spot* will be compared to the biggest spot in each simulation no matter if it is a cold or a hot spot.

However the Area still deviates from the Gaussian behaviour as can be seen in Figure 4.5. The most significant deviation is again found at scale R_9 and thresholds above 3.0.

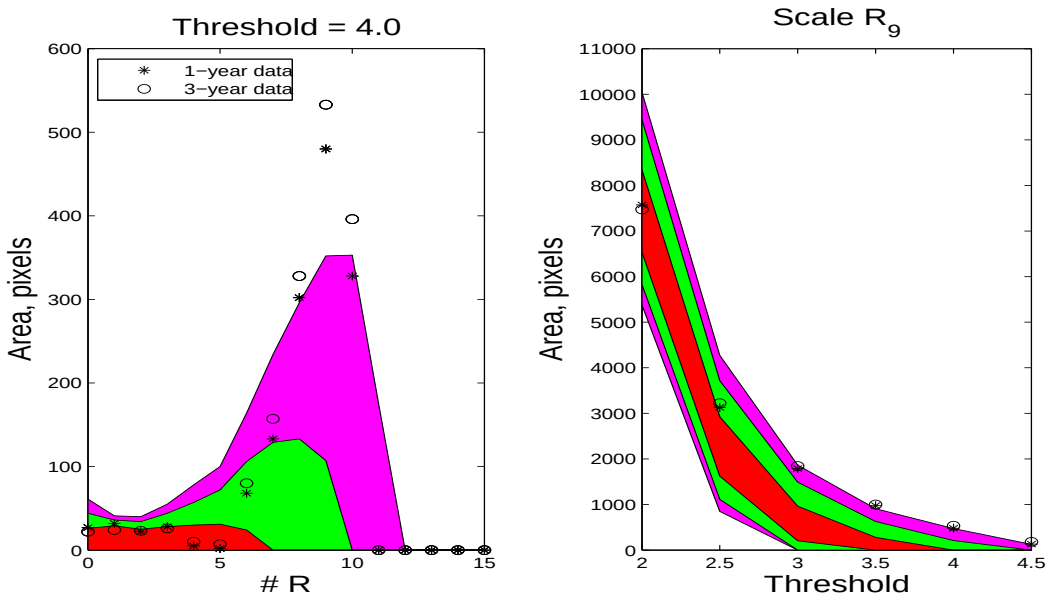

Figure 4.5 The left panel shows the cold Area in pixels, at threshold 4.0 versus the number of the scale. In the right panel the cold Area is represented versus the thresholds, while the scale is fixed at R_9. As in previous figures the asterisks represent the 1–year and the circles the 3–year data. The bands represent the acceptance intervals as in Figure 4.2

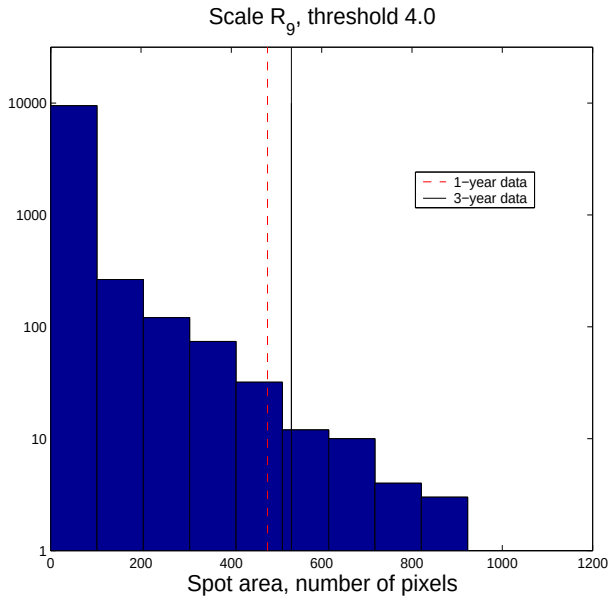

Figure 4.6 Histogram of all biggest spots of the simulations at threshold 3.0 and scale R_9. The dashed vertical line represents *the Spot* in the 1–year data and the solid one represents *the Spot* in the 3–year data.

Figure 4.6 shows the histogram of the biggest spot of each simulation compared to the 1–year and 3–year Area of *the Spot* at scale R_9 and threshold 4.0. *The Spot* is more prominent in the 3–year data and only very few simulations show bigger spots. The upper tail probabilities obtained at scale R_9 for 1–year and 3–year data are presented in table 4.2. As in the previous estimators, the 3–year data are in general slightly more significant. The new and more conservative definition of the Area estimator reduces the upper tail probability of *the Spot* although it is still widely below 1%.

threshold	probability 1–year data	probability 3–year data
3.0	0.68%	0.63%
3.5	0.36%	0.37%
4.0	0.34%	0.27%
4.5	0.44%	0.35%

Table 4.2 Upper tail probabilities of having a spot with higher or equal Area as *the Spot* assuming the Gaussian model, at scale R_9 and different thresholds.

threshold	probability 1–year data	probability 3–year data
3.0	0.51%	0.45%
3.5	0.33%	0.38%
4.0	0.32%	0.27%
4.5	0.44%	0.35%

Table 4.3 As Table 4.2, but for the Volume.

4.3.4 Volume

From the previous subsections we know that *the Spot* is extremely cold and it has a large Area at thresholds above 3.0. The best estimator to characterise *the Spot* would be therefore the volume. Hence we define the volume referred to a particular threshold as the sum of the temperatures of the pixels conforming a spot at this threshold. In Table 4.3 we compare the probability of finding a spot with higher or equal Volume as the data, assuming the Gaussian hypothesis. The values are very similar to those obtained for the Area estimator. Values for the Volume are slightly more significant and they show less variations with the threshold.

4.3.5 Higher Criticism

The HC statistic proposed in [57] was designed to detect deviations from Gaussianity that are caused by either a few extreme observations or a small proportion of moderately extreme observations. Moreover, the statistic provides a direct method to locate these extreme observations by means of HC values calculated at every individual data point.

For a set of n individual observations X_i from a certain distribution (X_i normalized to zero mean and dispersion one), HC is defined as follows. The X_i observed values are first converted into p-values: $p_{(i)} = P\{|N(0,1)| > |X_i|\}$. After sorting the p-values in ascending order $p_{(1)} < p_{(2)} < \ldots < p_{(n)}$, we define the HC at each pixel with p-value p_i, by:

$$HC_{n,i} = \sqrt{n}\left|\frac{i/n - p_{(i)}}{\sqrt{p_{(i)}(1-p_{(i)})}}\right|,$$

We compute the values of the HC statistic of the 3–year WCM in real and in wavelet space. The obtained values of the HC statistic are presented in Fig-

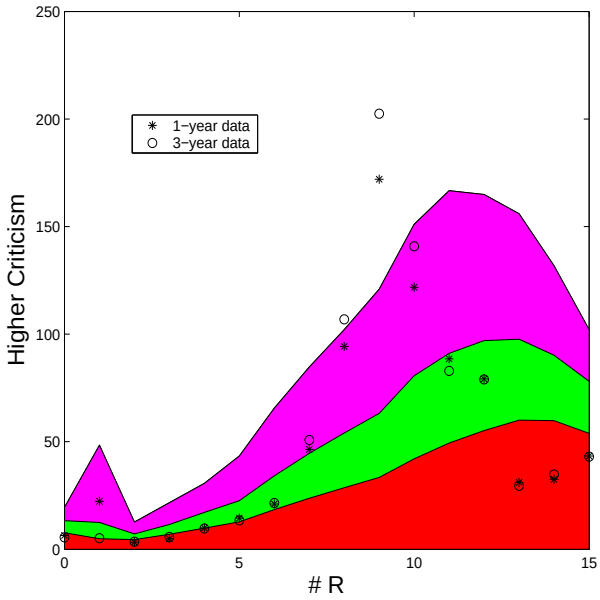

Figure 4.7 Higher Criticism values of the 1–year WCM (asterisks) and the 3–year WCM (circles). The acceptance intervals are plotted as in previous figures.

ure 4.7. These values correspond to the maximum of the HC values found at the individual pixels. As in previous figures, circles denote the results obtained from the 3–year WCM, asterisks those from the 1–year WCM and the bands represent the acceptance intervals. As one can see in the Figure, the data in wavelet space are not compatible with Gaussian predictions at scales R_8 and R_9 at the 99% c.l. This is in agreement with the result obtained in [32] for the 1–year WMAP data although there the HC values at scale R_8 were just below the 99% c.l. The upper tail probabilities for the 1–year and 3–year maximum HC values at scale R_9, are 0.56% and 0.36% respectively. The map of HC values at scale R_9 is presented in Figure 4.8. It is clear that the pixels responsible for the detected deviation from Gaussianity are located at the position of *the Spot*. Convolution with the wavelet causes the observed ring structure in the HC map. Figure 4.9 shows a blowout image of *the Spot* as it appears at scale R_9 in the wavelet map and in the HC map.

4.4 Significance

In the previous section, the upper tail probabilities of each estimator at scale R_9 were given. All the considered estimators showed the lowest upper tail proba-

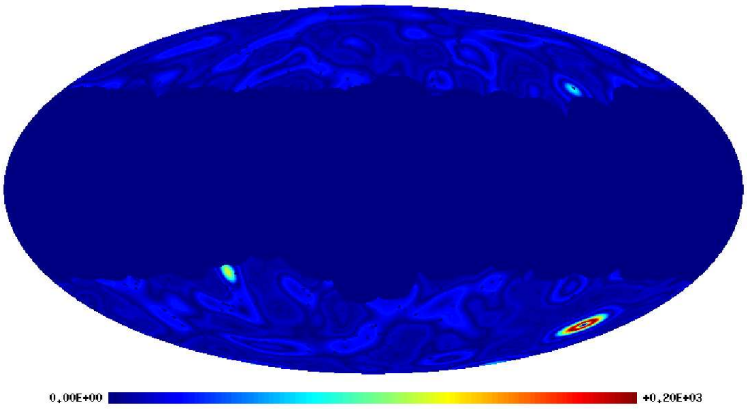

Figure 4.8 Higher Criticism of the 3–year WCM at scale R_9.

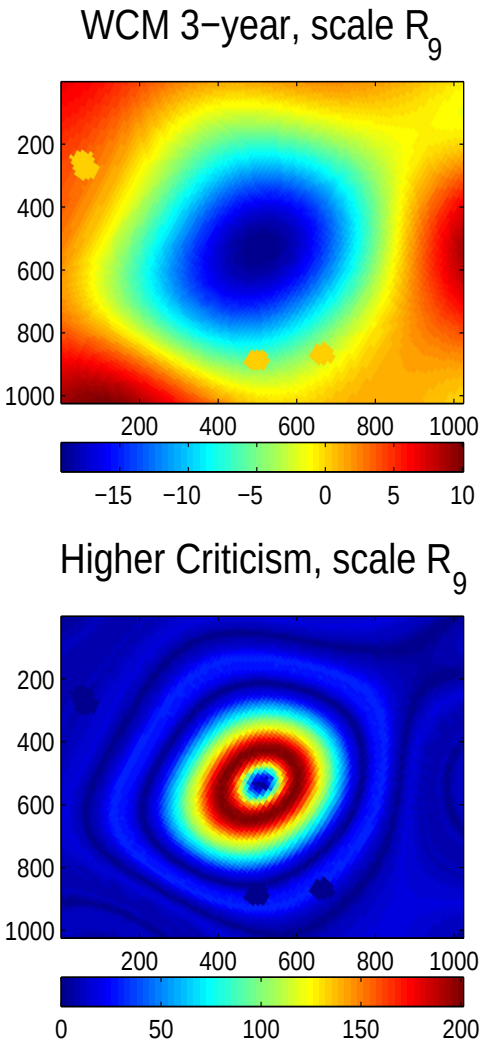

Figure 4.9 Image projected as in Figure 4.1, showing the 3–year WCM map (upper panel) and the Higher Criticism map (lower panel), both at scale R_9.

bility at scale R_9. However these are not rigorous measures of the significance of *the Spot*, since the number of performed tests is not taken into account. In this section we will recalculate the p-value of the deviation in the kurtosis found in [188] and discuss the issue of *a posteriori* significances.

When an anomaly is detected in a data set following a blind approach, usually several additional tests are performed afterwards to further characterize the anomaly. In most of these cases, the only reason these tests have been performed is the previous finding of the initial anomaly. If another anomaly would have been detected, other followup tests would have been performed. Hence these followup tests have not been performed blindly and should not be taken into account to calculate the significance of the initial detection.

This issue was already discussed in [44] and [126]. Both papers recalculated the significance of the excess of kurtosis in the 1–year WCM found in [188]. The excess of kurtosis was found performing a blind test, since no model was used and no previous findings conditioned the choice of the scales. Since 15 wavelet scales and two estimators (skewness and kurtosis) were considered, a total sum of 30 tests were performed. Three of these tests detected a strong deviation from Gaussianity. Scales R_7, R_8 and R_9 presented upper tail probabilities 0.67%, 0.40% and 0.38% in the 1–year data. This fact was taken into account in [44], but it was not in [126]. The latter searched through the simulations in order to find how many of them showed a higher or equal deviation than the maximum deviation of the data, ignoring that the data showed a high deviation at two adjacent scales. The p-value found in this way was 4.97% whereas in [44] 1.91% was obtained taking into account that the data deviate at three consecutive scales. It is also interesting to note that, when both Galactic hemispheres were considered independently, a p-value of 0.69% was found [44], although this could be considered as a followup test.

Some readers could find that the three-consecutive-scales criterion is an *a posteriori* choice since we look first at the data and given that they deviate at three consecutive scales, we then calculate from the simulations how probable this is. Therefore we should consider a new test which eliminates this *a posteriori* choice. We fix *a priori* a significance level which is the 1% acceptance interval given in all figures, and count for each estimator (skewness and kurtosis) how many scales lie outside, no matter if they are consecutive or not. Then we search through the simulations how many show at least that many scales outside the

Estimators	p-value
kurtosis	0.86%
skewness + kurtosis	1.85%
Max	11.64%
Area 3.0	3.27%
Area 4.0	1.09%
Higher Criticism	3.48%

Table 4.4 p-values for different estimators.

1% acceptance interval as the data.

Applying this test to the 3–year WCM, we find that scales R_8 and R_9 lie outside the 1% acceptance interval and scale R_7 lies on the border for the kurtosis estimator as can be seen in Figure 4.2. Searching through the simulations how many deviate in three scales either in the skewness or in the kurtosis estimator, we find a p-value of 1.85%, which is still below the p-value obtained for the 1–year data with the three-consecutive-scales criterion.

As already discussed we should not include the followup tests in a rigorous significance analysis. However it is difficult to assess if some of these tests would have been performed or not without the first finding [188]. In fact, the area and maxima analyses are very intuitive and simple. If the blind analysis in [188] had been performed on those estimators instead of using skewness and kurtosis, then the significance would be different. We should distinguish between those tests which are clearly followup tests, because the only reason they have been performed is the initial detection, and other tests which just have been performed after the initial detection, but could have been performed before.

Hence we apply our new robustness test to kurtosis, Max, Area at thresholds 3.0 and 4.0 and Higher Criticism separately. Note that whereas the first two estimators are two-sided, the Area and Higher Criticism are one sided estimators. The p-values obtained in this way are listed in Table 4.4. The kurtosis and Area at threshold 4.0 show p-values around 1%, Higher Criticism and Area at threshold 3.0 around 3%. On the contrary the Max estimator does not show a significant deviation from Gaussianity according to this robustness test.

The most conservative and reliable value is the 1.85% figure since it is not

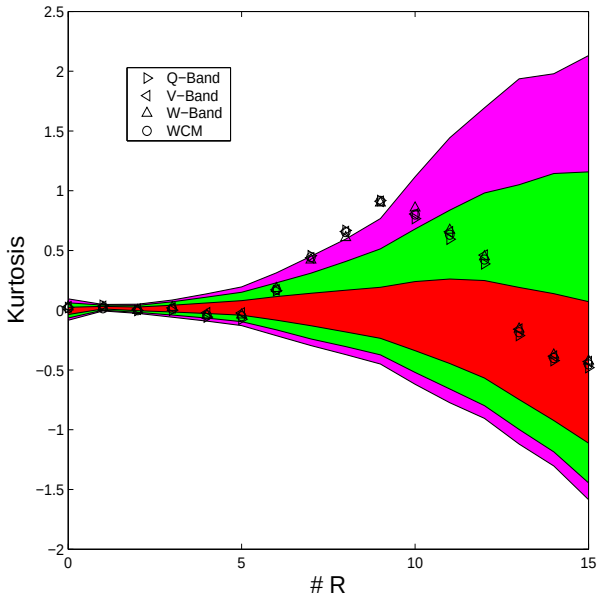

Figure 4.10 Kurtosis values for the Q, V and W bands, compared to the 3–year WCM values.

suspicious of being obtained through *a posteriori* analyses. Nevertheless it is still noticeable that the followup tests performed in [43], [44], [32] and in the present paper, confirm the initial finding with a very similar significance. Even if strictly speaking these should not be taken into account for establishing the significance of *the Spot*, they confirm the robustness of the detection.

4.5 Frequency dependence

In this section we will analyse the frequency dependence of the previously analysed estimators. A flat frequency dependence is characteristic of CMB, whereas other emissions such as Galactic foregrounds show a strong frequency dependence. Figure 4.10 shows that the kurtosis has almost identical values at the three foreground cleaned channels, namely Q,V and W. Same behaviour was observed in the 1–year data (see Figure 7 in [44]). Strong frequency dependent foreground emissions are unlikely to produce the detected excess of kurtosis.

The frequency dependence of the temperature at the center of *the Spot*, i.e. at the pixel where the temperature of *the Spot* is minimum in the WCM map, is presented in Figure 4.11. The error bars of the 1–year data have been estimated performing 1000 noise simulations as explained in section 5.1 of [44]. As the

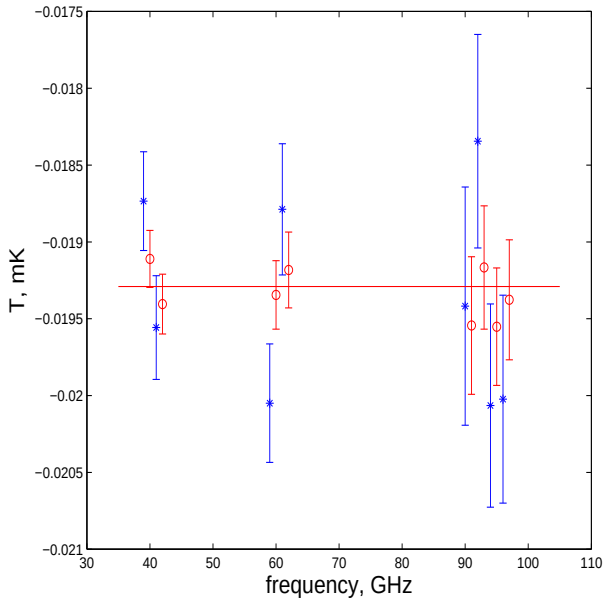

Figure 4.11 Frequency dependence of the temperature at the center of *the Spot* at scale R_9. Again the asterisks represent the 1–year data and the circles the 3–year data. The horizontal line shows the value of the 3–year WCM. The data at the same frequency have been slightly offset in abscissa for readability.

noise variance is ≈ 3 times lower in the 3–year data, we estimate the new error bars simply by dividing the old ones by $\sqrt{3}$. No frequency dependence is found for the new data set in agreement with the results for the 1–year data. *Max*, Area and HC values at different frequencies (see Figure 4.12, Figure 4.13 and Figure 4.14) show a very low relative variation compared to the 3–year WCM.

All these results confirm the analysis performed in section 5 of [44] where the data were found to fit a flat CMB spectrum. The present analysis confirms the disagreement between the conclusions in [44] and those in [115] where Galactic foregrounds were considered to be the most likely source for non-Gaussian features found with spherical wavelets.

4.6 Discussion

In [171] several reasons are enumerated to be cautious about the different anomalies found in the WMAP data: Galactic foregrounds or noise could be generating the non-Gaussianity, and in addition most of the claimed detections are based on *a posteriori* statistics. Also spatial variations of the noise variance and

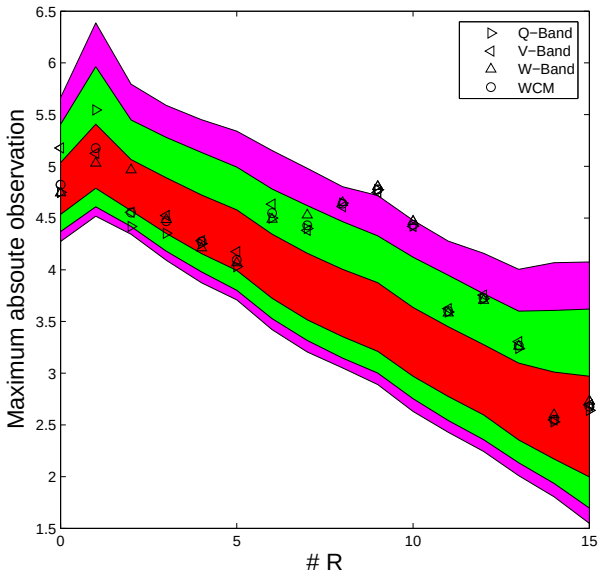

Figure 4.12 Maximum absolute observation for the Q, V and W bands, compared to the 3–year WCM values.

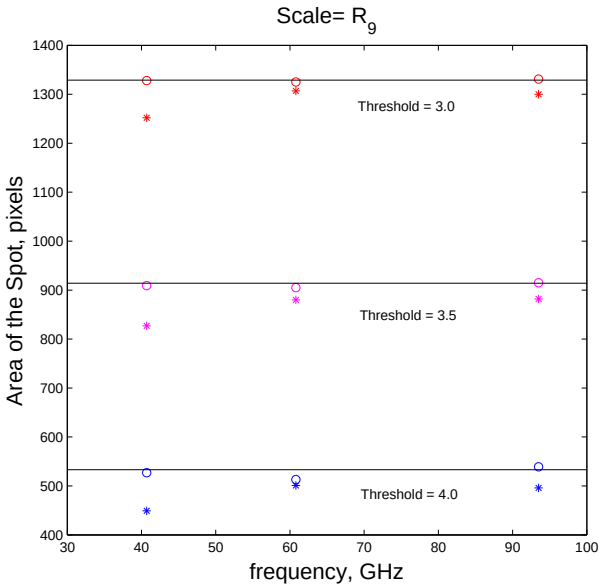

Figure 4.13 Frequency dependence of the Area of *the Spot* at scale R_9 and several thresholds. The 3–year WCM values are represented by horizontal lines.

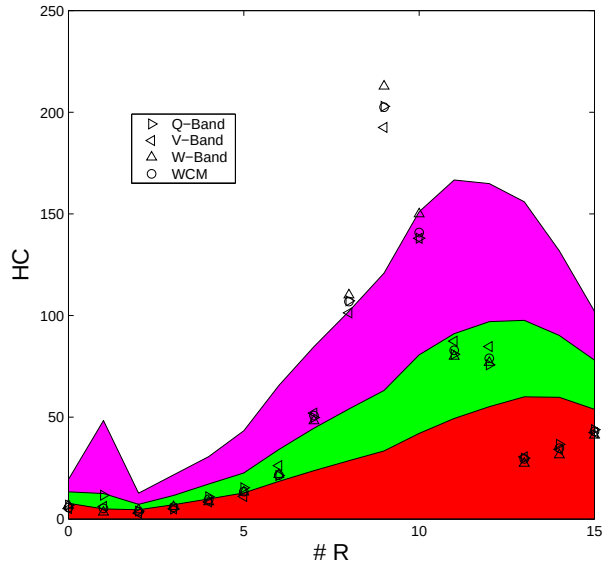

Figure 4.14 Higher Criticism values for the Q, V and W bands, compared to the 3–year WCM values.

$1/f$ noise could affect some of the performed analyses. They suggest several tests to be done using difference maps (year 1 - year 2, year 2 - year 3, etc.) and multi-frequency data.

We have tried to address all those points for *the Spot*. The *a posteriori* analysis is one of the most important issues raised in [171], since it is very difficult to get completely rid of it. Most analyses perform many tests and it is not easy to assess how many of them are followup tests and which is the probability of finding an anomaly by chance. As discussed in section 4.4 a very careful analysis shows that *the Spot* remains statistically significant at least at the 98% confidence level, without using any *a posteriori* statistics.

In addition *the Spot* was proved to remain highly significant no matter which foreground reduction technique was used [44]. These results are confirmed in the present paper. The new foreground reduction used in the 3–year data enhances slightly the significance of our detection. Moreover the multi-frequency analysis of the previous section shows an even flatter frequency dependence of *the Spot*.

As already discussed in previous sections the noise does not affect significantly our wavelet analysis. In fact the coadded 3–year results are very similar to those obtained with the 1–year data of the new data release. No significant cold spot

is observed based on the analysis of the three difference maps (year 1 - year 2, year 2 - year 3, and year 1 - year 3). Moreover Figure 4.11 shows that even the particularly $1/f$ contaminated W4 Difference Assembly shows almost the same result as all the other Difference Assemblies.

CHAPTER 5

Possible detection of a texture

As we have mentioned in previous chapters, recent observations in many cosmological fields tend to support the standard inflationary model which predicts the CMB anisotropies to be a Gaussian and isotropic random field, whereas alternative cosmological models such as non-standard inflation or topological defect models predict non-Gaussian features in the CMB. Unified theories of high energy physics typically predict the production of topological defects [101], [191] after a symmetry-breaking phase transition in the early Universe.

The Wilkinson Microwave Anisotropy Probe (WMAP) 1-year data [17], measured the CMB fluctuations with high accuracy and in a first approach [103], these were found to be consistent with the Gaussian predictions. Further analyses revealed asymmetries or non-Gaussian features which have been confirmed [51], [41], [65], [111], [193] in the 3-year WMAP data [90]. One of these features is the very cold spot in the southern hemisphere [188], [43],[44], [45] whose origin is still unclear.

Here we show that the spot described in the previous chapters could be produced by a topological defect, namely a texture, and find the size and amplitude of the spot and the implied abundance of textures to be consistent with that interpretation.

If confirmed, this detection of a cosmic defect will provide direct information about physics at energies well beyond any conceivable terrestrial experiment, and could affect the cosmological parameters which determine the content, age and evolution of the Universe.

5.1 Introduction

The spot is found at Galactic coordinates ($b = -57°, l = 209°$), and has an angular radius in the sky of $\approx 5°$. It was detected as a significantly non-Gaussian event on the CMB sky convolved with the Spherical Mexican Hat Wavelet (SMHW) [188], [43],[44], [45], an optimal tool for enhancing such features. The first analysis [188] used 15 different wavelet scales and two estimators, skewness and kurtosis. The kurtosis deviates significantly from Gaussian simulations at scales of $\sim 5°$. The spot was identified as the main cause of the deviation from Gaussianity, using the area estimator [43]. It has a flat spectrum, inconsistent with either Galactic foregrounds or the Sunyaev-Zeldovich effect [44]. The spot was confirmed in the 3-year WMAP data [45]. It was shown that, without any *a posteriori* assumption, the probability of such a high deviation in Gaussian simulations is around 1.85%. While the statistical significance is not conclusive, the cold spot is clearly an unusual feature, and a number of radical explanations have already been proposed [181], [96], [98], [25].

In this chapter we consider the possibility that the spot may be due to a cosmic texture [183]. Textures were proposed in 1989 as one of a zoo of possible defects which might have formed at symmetry breaking phase transitions in the early Universe. The idea that such defects seeded the formation of large scale structure was pursued at that time as an alternative to the standard inflationary paradigm, until it was decisively refuted in the mid 1990s. Nevertheless, it remains of great interest to search for cosmic defects, quite independently of their role in structure formation, since their observation would provide direct information about physics at the unification scale.

5.2 Textures

A texture forms whenever a continuous global non-Abelian symmetry is spontaneously broken [183]. If the broken symmetry is *local*, *i.e.*, gauged, the texture describes the vacuum structure and it is not of interest to observations in the late Universe. However, if the broken symmetry is of the simpler, *global* variety then cosmic texture forms, leading to interesting observable effects in the late Universe, and especially in the CMB sky. The standard model of particle physics includes both types of textures: the electroweak vacuum is a three-sphere and

hence supports local textures. Pions are the Goldstone bosons associated with the breaking of an approximate global symmetry relating the up and down quarks, which would be exact if their masses were zero. The example given below is a generalization of this case, illustrating the point that texture formation does not require fundamental Higgs fields.

In theories like string theory, which are based on local symmetries, global symmetries are not expected to be exact. However, in some extra-dimensional setups, especially those involving branes and large extra dimensions, *approximate* global symmetries do emerge naturally from gauge symmetries, and these can behave, for cosmological purposes, just like fundamental global symmetries [184].

One specially interesting class of models are theories of a continuous family symmetry, in particular SU(3), which is a natural choice since there are three families of elementary particles. In this case, the symmetry *cannot* be gauged, because it would then be anomalous. Furthermore, it is quite natural for this symmetry to be spontaneously broken at the GUT scale, in which case global texture is potentially observable in the CMB sky [100].

As a simple example of global non-Abelian symmetry breking, consider N Dirac fermions coupled to a Yang-Mills theory, with no Higgs fields. In the confining phase, SU(N) chiral symmetry is spontaneously broken. In cosmology, a symmetry-breaking transition would occur in the early Universe, resulting in a random field pattern which would progressively become ordered. As the Universe expands, the gradient energy in the symmetry-breaking field (or order parameter) is redshifted away: the initial, random configuration evolves in a scaling manner where the field progressively orders itself on a scale set by the Hubble horizon. If the vacuum manifold possesses a nontrivial topology (for texture, a nontrivial third homotopy group π_3), then in some regions of space there will be a topological obstruction to field ordering. In such regions, the only way for ordering to occur is for the winding configuration to draw itself together and collapse down to a microscopic scale, so that the field gradients become strong enough to pull the field off the vacuum manifold and over the potential energy barrier. The shrinking down and unwinding processes of texture knots would continue into the late Universe. An unwinding knot would lead to a concentration of stress-energy in spacetime and a time-dependent gravitational potential. CMB photons passing through such a region would receive a

red– or blue–shift with an amplitude set by the fundamental symmetry breaking scale ϕ_0 [183].

5.2.1 CMB spots produced by textures

Unwinding events may be approximated by a spherically symmetric scaling solution [183], on comoving scales $r < \kappa\tau$ where κ is a fraction of unity and τ is the conformal time when the texture unwinds. Such events lead to hot and cold spots on the CMB sky:

$$\frac{\delta T}{T}(\theta) = \pm\epsilon \frac{1}{\sqrt{1+4(\frac{\theta}{\theta_C})^2}}, \tag{5.2.1}$$

with angular separation θ, and parameters,

$$\epsilon = 8\pi^2 G\phi_0^2, \tag{5.2.2}$$

$$\theta_C \equiv 2\sqrt{2}\kappa \frac{(1+z)}{E(z)\int_0^z \frac{d\bar{z}}{E(\bar{z})}} \tag{5.2.3}$$

where $E(z) = \sqrt{\Omega_M(1+z)^3+\Omega_\Lambda}$ (Ω_M and Ω_Λ stand for matter and dark energy density parameters respectively). Following the discussion in [117], we truncate the profile of the temperature beyond its half-maximum by matching its value and derivative to a Gaussian: θ_C is then equal to the standard deviation of the matching Gaussian.

The expected number of hot and cold spots due to textures, with an angular size larger than some θ_C (measured in radians), is given by

$$N_{spot} = \int d\tau \frac{dn}{d\tau} 4\pi(\tau_0-\tau)^2 \int_{\theta_C(\tau_0-\tau)}^{\kappa\tau} 2dr, \tag{5.2.4}$$

where the number of texture unwindings per comoving volume per conformal time is $(dn/d\tau) = \nu\tau^{-4}$, with $\nu \approx 2$ as measured in numerical simulations. Here, τ_0 is the present conformal time and the factor $4\pi(\tau_0-\tau)^2$ is the comoving area of the sphere of currently detected CMB photons at the conformal time τ when the texture unwinds. If the unwinding event is inside the sphere, the photons “fall in" to an outgoing spherical shell of stress-energy and a blue spot is produced. Whereas if the event is outside the sphere, the photons “climb out" of the ingoing shell and a red spot is produced. The upper limit $r < \kappa\tau$ is imposed to account for the finite size of the region described by the single-texture scaling solution, and the factor two accounts for hot and cold

spots. The angular scale subtended by the resulting hot or cold spots is given (in the small angle approximation, and assuming a spatially flat Universe) by $\theta = r/(\tau_0 - \tau)$. If we consider spots larger than some size θ_C, this imposes the lower limit $r > \theta_C(\tau_0 - \tau)$ and the r integral is nonzero only for conformal times $\tau > \tau_0\theta_C/(\kappa + \theta_C)$.

We shall be interested in the regime where $\theta_C \lesssim \kappa$, in which case the integral simplifies to

$$N_{spot} \approx \frac{4\pi}{3}\nu\frac{\kappa^3}{\theta_C^2}. \tag{5.2.5}$$

The number of hot and cold spots of angular radius between θ_C and $\theta_C + d\theta_C$ is just the differential of the previous Equation, namely

$$\frac{dN_{spot}}{d\theta_C} = \frac{8\pi\nu}{3}\frac{\kappa^3}{\theta_C^3}, \tag{5.2.6}$$

It follows that the expected fraction of the sky covered by spots of angular radius greater than θ_C is

$$f_{sky} = \frac{\langle A\rangle}{4\pi} \approx \int_{\theta_C}^{1} d\theta\pi\theta^2\frac{2\nu\kappa^3}{3\theta^3} = \frac{2\pi\nu\kappa^3}{3}\ln(1/\theta_C), \tag{5.2.7}$$

where we approximated the upper limit, where the small angle approximation breaks down, as unity. Setting $\nu = 2$, $\kappa = 0.1$ and $\theta_C = 1^\circ$ we obtain $f_S = 0.017$.

Recent high-resolution simulations of SU(2) textures (performed by N. Turok and V. Travieso) show that the unwinding textures are smaller, and far more abundant, than was observed in low-resolution simulations conducted over a decade ago [1]. The unwinding knots are typically a tenth of the horizon size, hence $\kappa \approx 0.1$. The comoving number density n per conformal time τ scales as, $dn/d\tau = \nu\tau^{-4}$, but with $\nu \approx 2$, far higher than earlier estimates [169].

5.3 Analysis

We perform a Bayesian analysis (e.g. [93]) to give the posterior probability ratio, ρ, for the existence of this kind of texture-template in the combined, foreground–cleaned map (hereafter WCM) of the three–year WMAP data release [90]. Computing the posterior probability ratio, we can find the Hypothesis, H_i, best describing the data, $\mathbf{D}$ through a set of parameters, $\mathbf{\Theta}_i$. In our

[1] Movies are available at http://www.damtp.cam.ac.uk/user/ngt1000/

case the null hypothesis, H_0, describes the data as a Gaussian, homogeneous, and isotropic random field (CMB) plus the noise of the WMAP data. The alternative hypothesis, H_1 describes the data as CMB plus noise and an additional template, $\mathbf{T}$, given by a physical model, in our case a topological texture with parameters ϵ and θ_C.

Bayes' Theorem states:

$$\mathbb{P}(\mathbf{\Theta}|\mathbf{D}, H) = \frac{\mathbb{P}(\mathbf{D}|\mathbf{\Theta}, H)\mathbb{P}(\mathbf{\Theta}|H)}{\mathbb{P}(\mathbf{D}|H)}, \tag{5.3.1}$$

where $\mathbb{P}(\mathbf{\Theta}|\mathbf{D}, H)$ is the posterior probability distribution of the parameters, $\mathbb{P}(\mathbf{D}|\mathbf{\Theta}, H)$ the likelihood, $\mathbb{P}(\mathbf{\Theta}|H)$ the prior and $\mathbb{P}(\mathbf{D}|H)$ the Bayesian evidence. We redefine the notation, being the evidence E, the likelihood L, and the prior Π. The evidence provides normalisation of the posterior and is the average of the likelihood with respect to the prior:

$$E_i = \mathbb{P}(\mathbf{D}|H_i) = \int L_i(\mathbf{\Theta}_i|H_i)\Pi(\mathbf{\Theta}_i)d\mathbf{\Theta}_i, \tag{5.3.2}$$

which naturally incorporates an Occam factor favouring the hypothesis with fewer parameters.

The posterior probability ratio:

$$\rho \equiv \frac{\mathbb{P}(H_1|\mathbf{D})}{\mathbb{P}(H_0|\mathbf{D})} = \frac{E_1}{E_0}\frac{\mathbb{P}(H_1)}{\mathbb{P}(H_0)}, \tag{5.3.3}$$

can be used to decide beween both hypotheses. The alternative hypothesis is favoured when $\rho > 1$ and rejected otherwise. The a priori probability ratio for the two models, $\mathbb{P}(H_1)/\mathbb{P}(H_0)$, is given in our case by the fraction of sky covered by textures.

To compute the Bayesian evidence ratio we need the likelihood and normalised priors. The likelihood function is:

$$L \propto e^{-\frac{\chi^2}{2}}, \tag{5.3.4}$$

where

$$\chi^2 = (\mathbf{D} - \mathbf{T})^T \mathbf{N}^{-1} (\mathbf{D} - \mathbf{T}), \tag{5.3.5}$$

and $\mathbf{N}$ is the generalised noise matrix including CMB and noise. To compute $\mathbf{N}$, the CMB and the noise contributions have to be worked out. The calculation of the latter is straightforward since the number of observations per pixel

is known. In order to obtain the CMB contribution, we calculate the correlation function for the WCM taking into account the pixel and beam effects. As a complementary test we calculate the CMB correlation matrix through 70,000 Gaussian simulations. Comparing our results obtained from the WCM correlation function with those obtained using simulations, the errors are negligible.

As a conservative prior on ϵ, we choose $0 \leq \epsilon \leq 10^{-4}$, the COBE-normalised amplitude [144], [15], [60]. In order to obtain the prior for the scale parameter θ_C we normalise Equation (5.2.6) to unity between θ_{min} and θ_{max}. Photon diffusion would smear out textures smaller than a degree or so, so we set $\theta_{min} = 1^\circ$. At large scales textures are rare: we set $\theta_{max} = 15^\circ$.

Our template fitting is performed in a circular area of 20° radius centered at Galactic coordinates ($b = -57^\circ, l = 209^\circ$). We use the WCM in the HEALPix pixelization scheme [73] with resolution parameter Nside = 64. Since the scale of the cold spot we are interested in is around 5° (diameter of $\sim 10^\circ$) this resolution is good enough and reduces the number of pixels used in the template fitting. Excluding from the analysis the point sources masked in the three year kp0 mask, the total number of pixels considered is 1438. Although the angular size of the cold spot is about 10° we have to consider at least a 20° radius patch to take into account the whole neighborhood for the fit. The Spherical Mexican Hat Wavelet (SMHW) convolves all the pixels in this region and they could contribute in an important way to the detected structure.

Performing the template fitting, we find $\rho \approx 2.5 > 1$, favouring the existence of the texture. The data, the best fit template and their difference are presented in Figure (5.1).

Choosing different extrapolations of the temperature profile of Equation 5.2.1, as an exponential or a SMHW, we obtain $\Delta \ln E$ values between 4.7 and 5.2, which still give $\rho > 1$. The best fit amplitude and scale are $\epsilon = 7.7 \times 10^{-5}$ and $\theta_C = 5.8^\circ$. Marginalising the likelihood, we find $\theta_C = 6.0 \pm 2.6^\circ$ and $\epsilon = 7.5^{+3.9}_{-3.8} \times 10^{-5}$ at 95% confidence. The likelihood decreases fast enough at scales near θ_{min} or θ_{max} that the results do not depend on small variations of those limits, as can be seen in Figure (5.2). The value of ϵ inferred in this way from a single extreme event is biased by the detection of signals with high noise, *i.e.*, large Gaussian fluctuations. To check this we generated 500 Gaussian CMB simulations and added one texture spot to each, with amplitude $\epsilon = 4 \times 10^{-5}$, within the upper limits $\epsilon < 5 \times 10^{-5}$ inferred from the

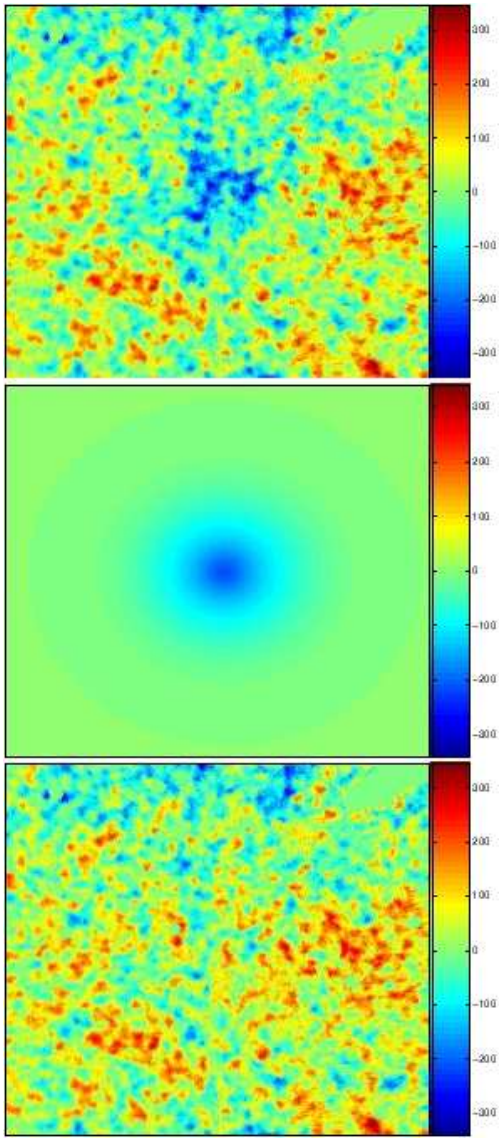

Figure 5.1 Azimuthal projection of a $43^\circ \times 43^\circ$ patch of the WCM, centered at ($b = -57^\circ, l = 209^\circ$) (Top). The best fit texture template is shown in the central panel, and the WCM subtracting the texture template is presented at the bottom. The units shown in the colorbars are μK and the resolution is Nside = 256. The y-axis points to the Galactic north pole. (The template is available on request)

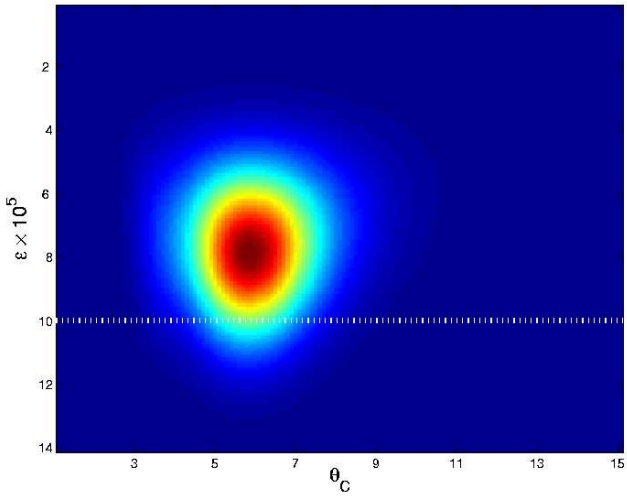

Figure 5.2 Likelihood for the template fit using the analytic formula with Gaussian extrapolation. The prior limit on the amplitude is marked by a dotted white line.

observed CMB anisotropy spectrum [21]. After performing a template fit, we select the spots with high posterior probability ratios, $\rho > 1$. The mean amplitude obtained from these spots is $\epsilon \approx 7.9 \times 10^{-5}$, hence there is significant overestimation. Moreover, a more realistic model of textures would predict some dispersion in the spot strength, with stronger spots caused by asymmetrical, multiple, or moving texture events. Again, selecting the strongest spot would lead to a biased value of ϵ.

The $\rho \approx 2.5$ result favours significantly the texture hypothesis. However, because we selected the spot centre *a posteriori*, we should also test whether prominent Gaussian CMB spots show such high values of ρ. Following the same selection procedure for 1000 Gaussian simulations, we find that prominent CMB spots show typical values of $\rho \approx 0.14 < 1$, and only $\sim 5.8\%$ of the simulations show $\rho > 2.5$. This percentage may decrease by performing an all sky analysis since most of these CMB spots appear in simulations with low kurtosis and as mentioned before the kurtosis of the data show a higher significance [45].

In order to further analyse the CMB signal from textures, we generate 1000 texture plus Gaussian CMB and noise simulations, and repeat the analyses performed on the Gaussian simulations with no textures. Considering that we observe one 5.8° texture in about half the sky (due to the extended Galactic mask), Equation (5.2.6) predicts around 68 hot and cold spots above $\theta_{min} = 1^\circ$. Adopting this phenomenological normalisation, we generate 68 spots per simulation

with the distribution given by Equation (5.2.6) using $\theta_{min} = 1^\circ$ and $\theta_{max} = \infty$ and random sign and position on the sky. The spot profile is as used above, and the amplitude is set to $\epsilon = 4 \times 10^{-5}$.

With textures added to the Gaussian CMB simulations with WMAP noise and beams, we repeat the previously performed skewness and kurtosis analysis [188], [45]. As there are on average the same number of hot and cold spots, the skewness is little affected. However, on the contrary, the kurtosis is increased so the anomalously high kurtosis of the data at scales around 5° is actually compatible with the Gaussian CMB plus textures interpretation (see Figure (5.3)).

It follows from Equation (5.2.6) that the number of spots of scale θ_C or above is $4\pi\nu\kappa^3/(3\theta_C^2) \approx 0.8$ for $\theta_C \approx 5.8^\circ$, consistent with the single observed spot. From the discussion below Equation (5.2.1), the observed texture unwound at $z \sim 6$, after the reionisation of the intergalactic medium and potentially within reach of very deep galaxy or quasar surveys.

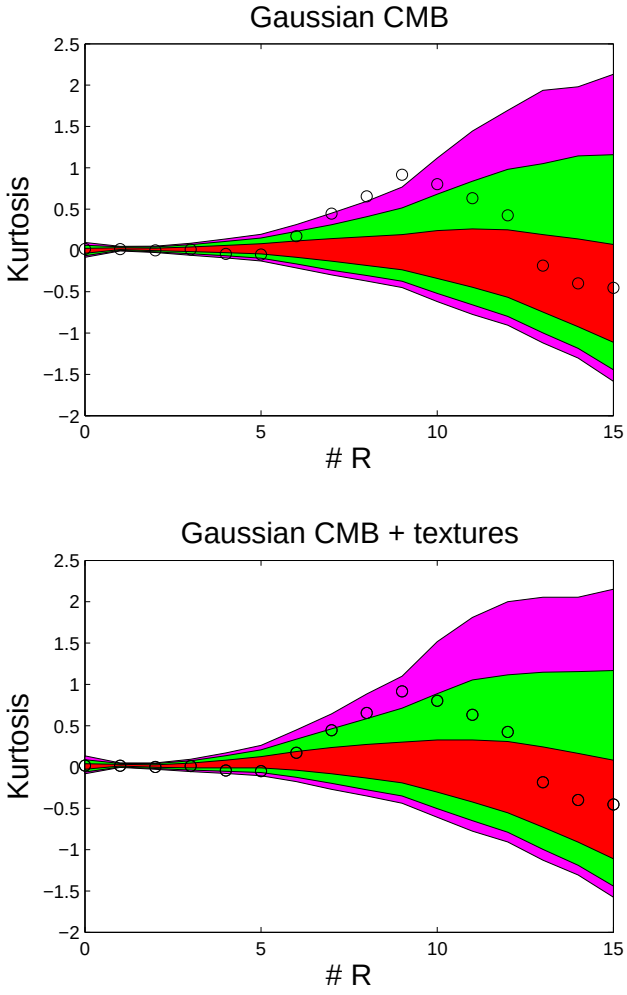

Figure 5.3 Kurtosis values for the 15 considered wavelet scales. The bands represent the 68% (red), 95% (green) and 99% (magenta) acceptance intervals given by 10000 simulations of Gaussian CMB (upper panel) and Gaussian CMB plus textures (lower panel). The WCM data (circles) show deviation from the expected values compared to Gaussian simulations, but are fully consistent with the Gaussian CMB plus textures interpretation at all scales. The scales are ($R_1 = 13.7$, $R_2 = 25$, $R_3 = 50$, $R_4 = 75$, $R_5 = 100$, $R_6 = 150$, $R_7 = 200$, $R_8 = 250$, $R_9 = 300$, $R_{10} = 400$, $R_{11} = 500$, $R_{12} = 600$, $R_{13} = 750$, $R_{14} = 900$ and $R_{15} = 1050$ arcmin)

CHAPTER 6

Conclusions

The detection of a non-Gaussian cold spot in the CMB sky has been presented in this thesis. A method based on spherical wavelets has been applied to the WMAP 1-year and 3-year data in order to study the Gaussianity of the CMB anisotropies. Gaussianity is a key issue to discriminate between different cosmological models. The cold spot is found at Galactic coordinates $b = -57^\circ, l = 209^\circ$ and covers around 10° on the sky. The probability of finding such a spot in Gaussian simulations is anomalously low. A conservative value for this probability is 1.85%. This calculation avoided any *a priori* consideration as discussed in Chapter 4. As the applied method was blind, a hard work has been done to investigate the origin of the anomaly. After discarding instrumental noise and foregrounds we focused on a particular model, cosmic textures. Calculating the posterior probability ratio of that hypothesis over the Gaussian hypothesis, we conclude that the Spot could be the first detection of a topological defect, namely a collapsing texture. If confirmed, this could have a far reaching impact since the inclusion of textures in the cosmological model could affect the present estimation of the cosmological parameters. In addition the detection of a topological defect, provides a unique link to the physics of the early Universe and high energy physics. Other radical explanations have been proposed to explain *The Spot*, such as voids or Sunyaev-Zeldovich effect. However in a work we are currently carrying out, these hypotheses seem to be disfavoured due to the large angular size of *The Spot*, which is incompatible with both hypotheses. Let us summarise the conclusions of each chapter of this thesis.

6.1 Chapter 2

Motivated by the non-Gaussianity found in the WMAP 1-year data using the SMHW, we have performed an analysis of the spots in the SMHW coefficients map, aimed to locate possible contributors in the sky. An extremely cold and big spot is detected. This spot, (*The Spot*), is seen in the SMHW coefficients at scales around 4° (implying a size of around 10° on the sky) and at Galactic coordinates $b = -57^\circ, l = 209^\circ$. The probability of having such spot for a Gaussian model at a particular scale is of only $\approx 0.2\%$, which implies that, if intrinsic, *the Spot* has not been originated by primary anisotropies in the standard scenario of structure formation since standard inflation predicts Gaussian fluctuations in the matter energy density and therefore in the CMB temperature fluctuations. When this spot is not considered in the analysis the rest of the data seem to be consistent with Gaussianity.

In order to identify the source of *the Spot* we have performed several tests related to systematic effects and foregrounds. We have checked that uncertainties in the noise or in the beam response have a negligible effect in our results at the relevant wavelet scales. Looking at the maps corresponding to the different receivers, we see a clear consistency in the area, amplitude and position of The Spot. Hence our detection is not due to any deficient receiver. In relation to the possible foregrounds contribution, we have looked for possible frequency dependences in the amplitude and area of *the Spot*. Again both quantities show a nice consistency with a constant line in the range from 23 to 94 GHz. Whereas the Galactic foregrounds show a very different frequency dependence with respect to the constant behaviour, the SZ effect does not separate much from it in that frequency range. A comparable spot could be produced either by the Coma cluster at a much closer distance, or by several rich clusters at the actual distance of Coma. We have checked that no nearby rich cluster of galaxies is located in the position of *the Spot*.

Finally, intrinsic fluctuations cannot be rejected as the source of *the Spot*. In particular, a massive and distant super-structure could in principle produce a decrement as the one observed through the Rees-Sciama effect [119]. This massive structure (of order of at least $10^{16} M_\odot$) should be placed far enough because otherwise it would have been detected previously. Alternatively, more speculative possibilities are topological defects (monopoles or textures) or non-

standard inflationary scenarios. Even more, a combination of secondary and primary anisotropies, cannot be rejected as the source of our non-Gaussian spot. For instance a possibility could be a combination of the Sunyaev-Zeldovich effect with a Sachs-Wolfe plateau.

6.2 Chapter 3

In this chapter we address the issue of the origin of non–Gaussian behaviours observed in the WMAP data. In particular, a non–zero kurtosis in the distribution of wavelet coefficients was detected in [188] at angular scales ranging from 3° to 5°. This non–Gaussian signal is mainly generated by the presence of a very cold spot in the southern hemisphere, at Galactic coordinates $b = -57^\circ$ and $l = 209^\circ$ [188], [43]. Its dimension ($\approx 8^\circ$) and temperature in wavelet space makes this spot quite exceptional compared to Gaussian CMB simulations: less than 1% of the simulations have spots with similar characteristics.

As a first step, we have verified the robustness of the deviation from Gaussianity in the kurtosis. We have performed a test taking into account the estimators used in that detection (skewness and kurtosis) and the number of consecutive wavelet scales presenting a significant deviation from Gaussianity, namely 4 considering only the southern hemisphere. The significance for the non–Gaussian detection remains still high: we obtained that only 0.69% of the simulations have equal or higher deviation of skewness or kurtosis at any four consecutive scales and in any of the Galactic hemispheres.

Afterwards we studied the morphology of *the Spot* using Elliptical Mexican Hat Wavelets on the sphere. We observed that the maximum amplification of *the Spot* temperature is obtained for almost isotropic Mexican Hat Wavelets, meaning that the shape of the underlying signal is essentially circular. This result does not discard for instance topological defects like textures or a gravitational potential with a circular shape as possible explanations.

Finally, we focus on the possible foreground contamination of *the Spot* region in the clean WMAP maps, considering the SZ effect or bad–subtracted Galactic foregrounds. The SZ effect is clearly discarded by the flat frequency dependence of *the Spot* temperature. The Galactic foregrounds case requires a more detailed analysis, since a hypothetical foreground mixing could provide a flat foreground contribution.

In wavelet space, the contribution of Galactic foregrounds in the region of *the Spot* is extremely low, at least one order of magnitude less than CMB at the Q, V and W bands. The dominating foreground is the free–free emission at all WMAP frequencies except at the W band where free–free is at the same level as dust emission and below the noise level.

If the non–Gaussian analysis is affected by unsubtracted Galactic foregrounds, we would expect that the non–Gaussian detection is more significant at frequencies where the foreground emission is more relevant. But neither the kurtosis nor the area and amplitude of *the Spot* are more significant at the Q band, i.e. the band where the Galactic contribution is higher respect to the V and W bands. In addition we obtain very similar results from CMB maps produced by completely independent foregrounds subtraction techniques (e.g. WCM and TCM).

Because of the large uncertainties in Galactic emission at microwave frequencies, we have even considered the possibility that our templates provide an important underestimate of foregrounds. Nevertheless, the possibility of having a strong and frequency independent foreground residue, which could explain the non-Gaussian nature of *the Spot*, is very unlikely.

According to our knowledge on Galactic emissions, we can conclude that there is no evidence for a relevant contribution of unsubtracted foregrounds in the region of the sky which is responsible for the non–Gaussian detection in wavelet space.

6.3 Chapter 4

In this chapter we repeat the analyses that detected the non-Gaussian cold spot called *the Spot* at ($b = -57^\circ, l = 209^\circ$) in wavelet space in the 1–year of WMAP data, using the recently released 3–year WMAP data. The previous works [188], [43], [32] and [44] found *the Spot* to deviate significantly from the Gaussian behaviour. *The Spot* was detected using several estimators, namely kurtosis, Area, *Max* and HC. This work confirms the detection applying all these estimators to the recently published 3–year WMAP data. At scale R_9, the upper tail probabilities of all these estimators when applied to the 3 year WMAP data are smaller than the corresponding ones for the first year WMAP data. This is mostly due to the improved foreground reduction of the data. We calculate the probabil-

ity of finding such a deviation from Gaussianity considering only skewness and kurtosis since these were initially used in [188] following a blind approach. Therefore excluding followup tests which could be considered as *a posteriori* analyses we obtain a p-value of 1.85%. Moreover, *the Spot* appears to be almost frequency independent. This result reinforces the previous foreground analyses performed in [44]. It is very unlikely that foregrounds are responsible for the non-Gaussian behaviour of *the Spot*. Comparing the WMAP single year sky maps, we conclude that the noise has a very low contribution to our wavelet analysis as already claimed in [188], [43]. The next chapter will be aimed at finding the origin of *the Spot*. As discussed in the introduction several possibilities have been considered, based on Rees-Sciama effects [149],[119], [120] and inhomogenous or anisotropic universes. Also topological defects [183], [59] as textures could produce cold spots. New and more detailed analyses are required in order to answer that question.

6.4 Chapter 5

We have investigated the hypothesis that *the Spot* is due to a cosmic texture and find the abundance, size and amplitude of *the Spot* to be consistent with that interpretation.

Using an analytical approximation of the temperature profile produced by a cosmic texture, we apply a template fit finding a posterior probability ratio favouring the existence of an underlying texture-like template centered at ($b = -57^\circ, l = 209^\circ$) with amplitude around 4×10^{-5} and scale $\sim 5^\circ$. The posterior probability ratio for the most prominent Gaussian spots is higher than the observed one in $\sim 5\%$ of the simulations. This is of an interesting, although not yet compelling, statistical significance.

The symmetry breaking scale corresponding to the observed amplitude is $\phi_0 \approx 8.7 \times 10^{15} GeV$. The existence of textures would not only help to discriminate between different fundamental physical theories of the unification of particles and forces, also the values of the cosmological parameters could be affected significantly.

Further observational tests might refute or strengthen the texture hypothesis. First, if the observed spot is due to a texture, there would be almost no associated CMB polarization. In contrast, if the spot is a rare statistical fluctuation in

the primordial density perturbation, we would expect a correlated polarization signal, namely a preference for a *radial* pattern of CMB polarization around it. On these scales, for adiabatic perturbations with standard recombination, almost half the polarization signal is correlated with the temperature anisotropy [42].

A second important prediction of the texture model is that there should be many smaller spots, with a distribution given by Equation (5.2.6). These would be masked or confused by the background adiabatic, Gaussian signal where it has maximal power, at $\theta \sim 1^\circ - 2^\circ$. Nevertheless, each spot would deviate from the expected polarization-temperature correlation and a combined all-sky measurement might reveal a difference from Gaussian, adiabatic perturbations due to many small texture spots.

The analytical model of texture-induced anisotropies used here is an idealization. A more careful study will require an ensemble of full sky texture CMB maps along the lines of previous works [144], [15], [60], but with far higher resolution to properly represent the non-Gaussianity. Such a study now appears feasible: the prospect that the observed spot, and perhaps other non-Gaussian anomalies, represent the first observations of topological defects in the Universe provides strong motivation.

6.5 Future Work

Many follow up tests have to be performed in order to confirm the possible detection of the texture as discussed in the previous section. Performing an ensemble of full sky texture CMB maps could allow to better compare with the detected deviation from Gaussianity. Moreover, a full sky Bayesian analysis can better determine the posterior probability ratio. Furthermore, analysing the polarization data can confirm or reject the texture hypothesis.

The comparison with other possible explanations such as huge voids or Sunyaev-Zeldovich effect, is already in progress. Both explanations seem to be disfavoured due to the large angular size of *the Spot*.

The Bianchi-like template detected in the WMAP data [25] and mentioned in Chapters 3 and 4 was also related to *the Spot*. A further work to be performed is to check whether *the Spot* is the main cause for this detected template.

CHAPTER 7

Resumen en castellano

7.1 Introducción

La radiación de fondo cósmico microondas (RFCM) es la radiación electromagnética más antigua que recibimos y, por tanto, una herramienta única para estudiar el origen del Universo.

La RFCM es uno de los pilares básicos de la teoría del Big-Bang, formulada en 1948 por George Gamow y sus colaboradores [5]. Según dicha teoría, el Universo se habría originado hace miles de millones de años, partiendo de una temperatura y densidad increíblemente elevadas. La teoría del Big-Bang explicaba la produccíon de núcleos ligeros y su abundancia relativa, así como la expansión del Universo que había sido observada por E. Hubble en 1929 [94]. Además, Gamow predijo la existencia de una radiación isótropa de unos 5 K, que procedería del Universo caliente y primordial. La baja temperatura de dicha radiación sería debida a la expansión del Universo.

Cuando Gamow hizo esta predicción aún no se había detectado la RFCM por lo que es considerada una de las pruebas más convincentes de su teoría. Casi dos décadas más tarde Penzias y Wilson [145] detectaron casualmente la RFCM y R. Dicke, P.J.E. Peebles, P.G. Roll, & D.T. Wilkinson [53] supieron interpretarla como la radiación predicha por Gamow.

Desde el momento en que se produjo este descubrimiento, una gran cantidad de experimentos han sido diseñados para estudiar la RFCM. La primera misión espacial dedicada a este fin, fue la misión COBE (COsmic Background Explorer) de la NASA cuyo satélite se lanzó en 1989. Dos de sus investigadores principales, G.S. Smoot (investigador principal del experimento *Differential Mi-*

crowave Radiometer, DMR) y J. Mather (investigador principal del experimento *Far Infrared Absolute Spectrophotometer*, FIRAS) recibieron el premio Nóbel de física en 2006. COBE-FIRAS demostró que la RFCM tiene un espectro de cuerpo negro casi perfecto [125] correspondiente a una temperatura de $T_0 = 2.725$ K. Restando a los datos esta temperatura media así como una componente dipolar debida a nuestro movimiento local, COBE-DMR detectó unas pequeñas anisotropías en la RFCM, del orden de $\Delta T/T_0 \sim 10^{-5}$ [167], (ver Figuras 1.2 y 1.1) en perfecto acuerdo con las predicciones de la teoría del Big-Bang. El Universo primordial es la fuente ideal de radiación térmica necesaria para producir un espectro de cuerpo negro y además Harrison [85], Peebles & Yu [143], y Zel'dovich [195] predijeron la existencia de inhomogeneidades del orden de $\sim 10^{-5} - 10^{-4}$.

En los años 90 las anisotropías fueron medidas cada vez con mayor precisión a través de experimentos terrestres o de globos aerostáticos. En 2000 los experimentos BOOMERanG [48] y MAXIMA [79] determinaron que la mayor potencia de las fluctuaciones se aprecia a escalas angulares de aproximadamente un grado. Junto a otras observaciones astronómicas estos resultados indicaban que la geometría del Universo es casi plana. En los siguientes años hubo varios experimentos que midieron también las anisotropías con buena resolución como el *Very Small Array* (VSA) [71], *Cosmic Background Imager* (CBI) [163], Archeops, *Arcminute Cosmology Bolometer Array Receiver* (ACBAR) [106], o el *Degree Angular Scale Interferometer* (DASI) [78], que fue el primer experimento en detectar la polarización de las anisotropías.

En 2003 se publicaron los resultados del primer año de observación del satélite *Wilkinson Microwave Anisotropy Probe* (WMAP) [17] de la NASA. Este satélite midió las anisotropías de la RFCM a todo el cielo con gran precisión y resolución. Un análisis detallado de dichas anisotropías permite estimar los parámetros cosmológicos (ver Tabla 1.1) que determinan la edad, geometría y composición del Universo. Estos análisis son por tanto de gran importancia para la cosmología. El modelo que mejor se ajusta a los datos es el modelo estándar, Λ-*materia oscura fría* [171]. Las observaciones de estructura a gran escala y supernovas también concuerdan con este modelo por lo que a veces es denominado como modelo concordante. En él se supone un Universo sin curvatura y con una expansión acelerada causada por la constante cosmológica, Λ, también denominada *energía oscura* por su origen desconocido. Según las observaciones

de supernovas y RFCM la energía oscura representa $\sim$ 74% de la densidad de energía del Universo. La mayor parte de la energía restante se encuentra en forma de materia oscura fría, que es materia no bariónica y no relativista de composición desconocida. La materia oscura no emite ni refleja radiación y no ha sido observada directamente aunque su existencia ha sido probada por sus efectos gravitatorios. Sólo el 4% de la energía del Universo es debida a materia bariónica ordinaria.

Sin embargo la composición y condiciones físicas del Universo primitivo eran muy distintas. Si extrapolamos hacia atrás la expansión del Universo, alcanzamos temperaturas y densidades infinitas hace unos 14 000 millones de años. Esta singularidad es la llamada Big-Bang. Hasta 10^{-43} segundos (tiempo de Planck) después del Big-Bang los efectos cuánticos de la gravedad, que aún no se conocen, son dominantes y por tanto las leyes de la física dejan de funcionar en esta época. A partir de un segundo después del Big-Bang, las leyes de la física funcionan y podemos entender y describir lo ocurrido entonces. El Universo era muy homogéneo e isótropo, siendo su temperatura y presión tan altas que causaron una rápida expansión del Universo y su consiguiente enfriamiento.

Algunas teorías afirman que 10^{-35} segundos después del Big-Bang el Universo pasó por una transición de fase que provocó una expansión exponencial del Universo. Este proceso es conocido cómo *inflación* y sería el causante de que el Universo sea plano, homogéneo e isótropo a gran escala.

Al finalizar la inflación, el Universo estaba formado por un plasma de quarks y gluones. Posteriormente, gracias al enfiramiento debido a la expansión del Universo, se formaron los bariones.

Sin embargo los átomos no se formaron hasta varios miles de años después, ya que radiación y materia estaban interaccionando continuamente impidiendo que se juntaran electrones y protones, y no dejando escapar a los fotones. Cuando la temperatura del Universo bajó hasta $\sim$ 3000 K, la tasa de interacción era suficientemente baja para permitir la formación de átomos y el escape de los fotones. Este desacoplo entre radiación y materia ocurrió unos 375 000 años después del Big-Bang. Los fotones emitidos en ese momento desde todos los puntos de forma isótropa, constituyen la RFCM que recibimos hoy después de viajar por el espacio durante casi 14 000 millones de años.

Como el Universo era en aquella época muy homogéneo e isótropo, medimos

en promedio la misma radiación de fondo en cualquier dirección del cielo observable. Los fotones que observamos fueron emitidos en la *Superficie de Última Dispersión* hace $\approx$ 14 000 millones de años. Las fluctuaciones de densidad presentes en aquel momento, quedaron impresas en la RFCM.

El satélite PLANCK de la agencia espacial europea (ESA) se lanzará el año 2008 y medirá las anisotropías de la RFCM con una precisión y resolución sin precedentes. Además su amplio rango de frecuencias que va desde 30 a 857 GHz permitirá identificar mejor las emisiones contaminantes de la Galaxia. Se espera que la misión PLANCK confirme los resultados de WMAP, mida escalas angulares aún sin explorar y mejore las medidas de polarización.

Las anisotropías de la RFCM se clasifican atendiendo al momento en que se originaron en primarias y secundarias.

- **Anisotropías Primarias**, se generaron en la *Superficie de Última Dispersión*. La física del plasma de bariones y fotones causa estas anisotropías. La presión de radiación de los fotones compite con la atracción gravitatoria de los bariones, creando oscilaciones acústicas. A gran escala domina el efecto Sachs-Wolfe [151] debido a variaciones en el potencial gravitatorio, mientras que a pequeña escala los efectos de amortiguamiento debido al espesor finito de la superficie de última dispersión o a la difusión [164] son los dominantes.

- **Anisotropías secundarias**, se producen entre la superficie de última dispersión y el observador. Son debidas a interacciones de los fotones de la RFCM con gas caliente o potenciales gravitatorios. El efecto gravitatorio se denomina efecto *Sachs-Wolfe integrado* (ISW). Hay dos tipos de efecto ISW el temprano y el tardío. El primero ocurre poco después de que los fotones abandonen la superficie de última dispersión y es debida a la evolución de los potenciales gravitatorios cuando el Universo deja de estar dominado por la radiación para estar dominado por la materia. El ISW tardío se produce por cambios en el potencial cuando la constante cosmológica empieza a gobernar la dinámica de la expansión. Si el ISW es debido a la evolución no lineal de una estructura que colapsa, también se conoce como efecto *Rees-Sciama* [149], [120].

  La *reionización* del Universo después de la recombinación genera electrones libres que interaccionan con los fotones de la RFCM produciendo aniso-

tropías secundarias. Las primeras poblaciones de estrellas de población III y quásares, emiten radiación reionizando el Universo de forma global [72]. La reionización local se produce al formarse cúmulos de galaxias. El gas caliente atrapado en su interior contiene electrones altamente energéticos que distorsionan el espectro de la RFCM al interaccionar con los fotones por efecto Compton inverso [174]. Este efecto es denominado efecto *Sunyaev-Zeldovich térmico* cuando la energía de los electrones es debida a su temperatura y efecto *Sunyaev-Zeldovich cinemático* cuando es debido a la velocidad peculiar del cúmulo.

El efecto *lente gravitatoria* es otro efecto que produce anisotropías secundarias [121]. Es causado por supercúmulos de gran masa que desvían gravitatoriamente la trayectoria de los fotones de la RFCM.

7.1.1 Datos de WMAP

El Wilkinson Microwave Anisotropy Probe (WMAP, [17]) es un satélite de la NASA que fue lanzado en 2001. Está situado en el punto lagrangiano Sol-Tierra, L2 a unos 1.5 millones de kilómetros de la Tierra.

Los radiómetros de WMAP miden temperaturas diferenciales de la RFCM a 5 frecuencias distintas: banda K (22.8 GHz, 1 ensamblaje diferencial), banda Ka (33.0 GHz, 1 ensamblaje diferencial), banda Q (40.7 GHz, 2 ensamblajes diferenciales), banda V (60.8 GHz, 2 ensamblajes diferenciales) y banda W (93.5 GHz, 4 ensamblajes diferenciales).

La resolución angular va desde 0.9 a 0.2 grados y la sensibilidad esta alrededor de 1 mK $s^{1/2}$. La pixelización utilizada para todos los mapas es la *Hierarchical, Equal Area and iso-Latitude Pixelization* (HEALPix, [73])[1], con parámetro de resolución N_{side}.

Los parámetros cosmológicos obtenidos con estos datos se dan en la tabla 1.1.

El equipo de WMAP recomienda utilizar un mapa (WCM, ver Figura 1.4) combinación de los canales Q, V y W pesados por el ruido para análisis cosmológicos, ya que las bandas K y Ka están dominadas por radiación contaminante de la Galaxia.

Desafortunadamente existen muchos tipos de radiación contaminante, que han

[1] http://www.eso.org/science/healpix/

de ser entendidos y sustraídos de los mapas. Una vez hecho esto, el monopolo y el dipolo residual han de ser restados.

7.1.2 Contaminantes

La señal de la RFCM nos llega mezclada con emisiones contaminantes de la Vía Láctea y extragalácticas. Entre las radiaciones contaminantes provenientes de la Galaxia destacan la radiación *sincrotrón*, la radiación de *free-free* y la de *polvo*. La dependencia frecuencial de los contaminantes Galácticos (en un cierto rango de frecuencias), suele expresarse como $T \sim \nu^{\beta}$, donde β se denomina índice espectral.

La radiación sincrotrón se produce cuando los electrones de los rayos cósmicos son acelerados en campos magnéticos y su índice espectral varía entre -2.6 y -3.1. La radiación free-free es emitida cuando chocan electrones e iones. Su índice espectral es -2.15 a frecuencias superiores a 10 GHz. Los granos de polvo interestelar absorben radiación ultravioleta, reemitiendo en el infrarrojo y microondas. Su índice espectral está entre 1.5 y 2.5 en el rango de frecuencias de WMAP.

En la Figura 1.5 se ve la variación con la frecuencia y la intensidad estimada de los contaminantes a las frecuencias de WMAP.

Objetos extragalácticos como quásares, galaxias, núcleos galácticos activos o galaxias que emiten en el infrarrojo, también emiten radiación microondas. Al ser objetos muy lejanos, aparecen como *fuentes puntuales* en los mapas de RFCM. Las más brillantes pueden tener una contribución importante y deben ser excluidas. El equipo de WMAP ha identificado y enmascarado cientos de fuentes puntuales. Recientemente se ha dado un nuevo catálogo de fuentes utilizando métodos basados en ondículas [116].

Para eliminar los píxeles más afectados por contaminación, el equipo de WMAP propone utilizar máscaras. La máscara kp0 es la más conservadora y excluye alrededor del 23% de los píxeles incluyendo unos centenares de fuentes puntuales.

7.1.3 Gaussianidad

La Gaussianidad de las anisotropías de la RFCM es una predicción testable de los modelos inflacionarios más simples [74], [9]. Las fluctuaciones cuánticas de vacío del campo inflacionario tienen una distribución Gaussiana. La inflación amplifica estas pequeñas fluctuaciones de vacío, creando las semillas para la formación de estructura en el Universo. Las anisotropías de la RFCM se relacionan con las fluctuaciones de energía a través de las ecuaciones de Einstein-Boltzmann linearizadas, y por tanto su distribución también es Gaussiana (ver Liddle & Lyth [114]). Incluso en estos modelos puede haber pequeñas desviaciones de la Gaussianidad debido a efectos no lineales de segundo orden. Sin embargo en el modelo estándar estas desviaciones son totalmente despreciables, mientras que en la inflación no-estándar (ver [13]) la no-Gaussianidad es apreciable.

Los modelos de defectos topológicos [191] también producen rasgos no- Gaussianos en la RFCM. Las teorías unificadas de física de altas energías, predicen la producción de defectos topológicos durante una transición de fase con ruptura de simetría, en el Universo primordial. Dependiendo del orden, O(N), de la simetría que se rompe, pueden aparecer distintos tipos de defectos. Las paredes de dominio son membranas dos dimensionales que aparecen al romperse una simetría discreta, de orden 1; si la simetría que se rompe es de orden 2, axial, aparecen cuerdas cósmicas unidimensionales; en el caso de una ruptura de simetría esférica (orden 3) se forman defectos puntuales llamados monopolos, y finalmente las texturas se crean después de romperse una simetría de orden 4. Los defectos topológicos son fenómenos de altísima energía que dejan su huella en la RFCM. Cada defecto produce un tipo de anisotropía característica. Por ejemplo las texturas producen manchas calientes y frías en la RFCM.

Otra predicción de la inflación es la isotropía, homogeneidad y planitud del Universo, debido a la drástica expansión inflacionaria. Topologías no triviales [107] o modelos anisotrópicos del Universo producirían un patrón de anisotropías característico. Por ejemplo un modelo homogéneo y anisótropo con vorticidad, produciría una anisotropía espiral en la RFCM. Las topologías no triviales también podrían generar señales que producen desviaciones de la Gaussianidad e isotropía.

El estudio de la Gaussianidad de la RFCM permite por tanto discriminar entre

distintos modelos cosmológicos.

Como la mayoría de los estudios de no-Gaussianidad son *ciegos*, es decir no dependientes de un modelo concreto, hay que realizar un gran esfuerzo para identificar el origen de una posible desviación de la Gaussianidad ya que hay muchas posibles causas. Además de las no-Gaussianidades primordiales, la mayoría de las anisotropías secundarias son no-lineales y por tanto no- Gaussianas. Lo mismo ocurre con los contaminantes y el ruido instrumental.

En los últimos años con la llegada de las medidas de precisión de la RFCM se han realizado numerosos análisis de Gaussianidad, utilizando infinidad de herramientas matemáticas. Dependiendo de la no-Gaussianidad que se quiera detectar, se deberá usar una u otra herramienta. Algunas de las más usadas son: funcionales de Minkowski, funciones de correlación, bispectro, trispectro, correlaciones de fase y ondículas.

En experimentos anteriores a WMAP no se encontró ninguna desviación de la Gaussianidad que fuese intrínseca. En los datos de WMAP se está debatiendo el origen de varias anomalías, como por ejemplo: alineamientos y simetrías en multipolos bajos; asimetrías en la potencia de las fluctuaciones entre los hemisferios eclípticos; alineamiento de manchas de la RFCM; y la que presentamos en esta tesis, una mancha extraordinariamente fría en el hemisferio sur, *la mancha*, [43], [44], [45], [46]. *La mancha* fue considerada como posible anomalía en [188] y confirmada después por [43], [32], [44] y [45], [46] en los datos del tercer año de medida de WMAP. La herramienta utilizada en estos análisis es la Ondícula Esférica de Sombrero Mejicano (*Spherical Mexican Hat Wavelet*, SMHW) que describimos más abajo.

Todas estas asimetrías, excepto *la mancha*, están relacionadas con el plano eclíptico por lo que se sospecha que puedan ser debidas a un efecto sistemático por determinar.

En esta tesis discutiremos en detalle el posible origen de *la mancha*. Como veremos en el capítulo 6, podría ser la primera detección de un defecto topológico.

Ondículas

Una función se puede expresar mediante una transformada de Fourier como una suma de funciones sinusoidales. Análogamente, con una transformación de ondícula se representa una función como combinación de ondículas, que

son funciones matemáticas diferentes de las sinusoidales. La diferencia fundamental es que las ondículas están localizadas tanto en el tiempo como en la frecuencia mientras que la transformada de Fourier sólo está localizada en frecuencia.

La transformación de ondículas permite dividir una función dada en diferentes componentes, cuya escala coincide con la de la *ondícula hija* que es una copia trasladada y dilatada de una onda finita llamada *ondícula madre*.

Las transformadas de ondículas se pueden agrupar en discretas como la ondícula de Haar [75], y continuas como la ondícula esférica de sombrero mejicano (*Spherical Mexican Hat Wavelet*, SMHW). Actualmente se usan un buen número de ondículas en campos tan diversos como reducción de datos, análisis de imágen, geofísica, óptica, acústica,... y astrofísica.

En los últimos años se han publicado numerosos trabajos sobre la RFCM usando ondículas. Se pueden utilizar en separación de componentes [179], [28], [185],[186], [187],[70], [116], para eliminar ruido instrumental [153], [154], análisis de correlación [189], [130], y estudios de Gaussianidad [139], [92], [4], [10], [11], [126], [128], [193], [190] además de los citados más abajo para el caso particular de ondículas con simetría esférica. Las ondículas incrementan el cociente señal-ruido permitiendo la detección de señales no-Gaussianas débiles. Además permiten localizar la señal no-Gaussiana y conocer su escala angular.

En nuestro caso la ondícula apropiada es la SMHW [6], que es una proyección estereográfica de la ondícula de sombrero mejicano en el plano (ver Figura 1.6).

La SMHW se ha aplicado en estudios de Gaussianidad para los datos de COBE, [29], [31].

En esta tesis, presentamos un análisis de Gaussianidad de los datos de WMAP con la SMHW, escrito en [43], [44], [45], [46]. En otros trabajos como [188], [134], y [32] también se ha utilizado la SMHW.

La SMHW amplifica eficientemente los rasgos no-Gaussianos en la esfera [122]. La ondícula madre de la SMHW es:

$$\Psi_S(y,R) = \frac{1}{\sqrt{2\pi}N(R)}\left[1+\left(\frac{y}{2}\right)^2\right]^2\left[2-\left(\frac{y}{R}\right)^2\right]e^{-y^2/2R^2}, \qquad (7.1.1)$$

donde R es la escala y $N(R)$ la constante de normalización:

$$N(R) \equiv R\sqrt{1+R^2/2+R^4/4}. \qquad (7.1.2)$$

La distancia en el plano tangente, y, se relaciona con el ángulo polar (θ) como: $y \equiv 2\tan\theta/2$. La SMHW es la proyección estereográfica de la ondícula de sombrero mejicano que es a su vez la laplaciana de una Gaussiana.

Por tanto, en esta tesis exponemos un análisis de Gaussianidad de los datos de WMAP realizado con ondículas en la esfera. A continuación presentamos un resumen de los capítulos.

7.2 Capítulo 2

En este capítulo se analiza una mancha extremadamente fría y grande, *la mancha*, en los datos del primer año de observación del satélite WMAP. Este trabajo es una continuación de un artículo anterior [188] en el que se detectaba una desviación de la Gaussianidad con un método basado en la SMHW (ver introducción). Aquí estudiamos las manchas a distintos umbrales en los mapas de coeficientes de ondícula, considerando seis estimadores distintos: número de máximos y mínimos, número de manchas calientes y frías y número de píxeles calientes y fríos. A escalas de la SMHW alrededor de 4° (10° en el cielo), los datos se desvían del comportamiento Gaussiano. El análisis se realiza en todo el cielo, hemisferio norte, hemisferio sur y en cuatro cuadrantes por separado. Demostramos que *la mancha* situada en las coordenadas galácticas ($b = -57^\circ, l = 209^\circ$) es incompatible con la hipótesis de Gaussianidad. Comparando dicha mancha con la más grande de cada una de las 10 000 simulaciones Gaussianas, vemos que para la escala de 5° sólo 0.2% de las simulaciones presentan una mancha igual o más grande que la de los datos. Excluyendo esta mancha del análisis, el resto del mapa sí es compatible con las simulaciones Gaussianas y el exceso de kurtosis encontrado en [188] también desaparece. Finalmente analizamos si *la mancha* podría ser debida a algún tipo de ruido instrumental o emisión contaminante y concluimos que éstos no parecen ser la causa de la detección.

7.3 Capítulo 3

Aquí se estudia en detalle *la mancha* encontrada en el capítulo anterior en los datos del primer año de WMAP. En primer lugar se calcula rigurosamente la significación del exceso de kurtosis detectado en los mapas de WMAP por [188]

tras convolucionarlos con la SMHW. Como vimos en el capítulo anterior este exceso de kurtosis es debido en gran medida a *la mancha*. Confirmamos que la detección es robusta y encontramos que la probabilidad de encontrar esta desviación por azar es 0.69%. Después analizamos la morfología de *la mancha* convolucionando los datos con SMHW con distintas elipticidades. La forma de *la mancha* es casi circular. Finalmente discutimos si la no-Gaussianidad observada podría ser debida a emisiones contaminantes mal sustraídas. Demostramos que la dependencia frecuencial de *la mancha* es muy plana y por tanto no puede ser explicada por el efecto Sunyaev-Zeldovich térmico. Según los conocimientos actuales de los contaminantes Galácticos, los residuos en la región de *la mancha* no pueden afectar significativamente a la detección.

7.4 Capítulo 4

En este capítulo analizamos *la mancha* que habíamos detectado en los datos del primer año de WMAP, con los datos del tercer año de observación de dicho satélite. Con estos nuevos datos volvemos a detectar *la mancha* en la misma posición ($b = -57^\circ, l = 209^\circ$) y tamaño ($\approx 10^\circ$ en el cielo). En este trabajo hemos utilizado diversos métodos y estimadores siempre basados en la SMHW. Analizamos la kurtosis, la temperatura máxima absoluta, el número de píxeles por encima de un umbral dado, el volumen y el *Higher Criticism*. Todos ellos detectan una desviación de la Gaussianidad con una significación ligeramente más alta que la encontrada en los datos del primer año. Este ligero aumento es debido a la nueva técnica para eliminar las emisiones contaminantes de la Galaxia y no a la reducción de ruido instrumental que es despreciable a la escala de *la mancha*. Para evitar análisis *a posteriori* que puedan falsear la significación de la mancha, recalculamos la significación de la kurtosis para los datos del tercer año de WMAP. Esta vez consideramos un test *a priori*, antes de mirar los datos, para skewness y kurtosis que fueron los primeros estadísticos que se usaron en el análisis con la SMHW. Obtenemos que la probabilidad de encontrar una desviación mayor o igual en simulaciones Gaussianas es 1.85%. La dependencia frecuencial de *la mancha* es aún más plana que en los datos del primer año. Por tanto, es improbable que la contaminación Galáctica sea responsable de la desviación de la Gaussianidad.

7.5 Capítulo 5

En este capítulo consideramos la posibilidad de que *la mancha* sea producida por un defecto topológico, una textura. Las teorías unificadas, predicen la formación de defectos en una transición de fase en el Universo temprano. La ruptura de simetría asociada a la transición de fase habría provocado la formación de defectos topológicos altamente energéticos que dejaron su huella en la RFCM. Realizamos un test de hipótesis bayesiano para ver si el perfil de *la mancha* coincide con el perfil analítico aproximado de una mancha generada por una textura. Encontramos un cociente de probabilidades a posteriori favorable a la hipótesis de tener una textura más el campo Gaussiano frente a la de tener solamente un campo Gaussiano. La amplitud y el tamaño de la mancha son consistentes con esta interpretación y el número esperado de texturas también lo es. Para ver como afecta el modelo de texturas a nuestro análisis de kurtosis de los coeficientes de ondículas, simulamos texturas con un perfil analítico que es una aproximación del real y las añadimos a simulaciones Gaussianas. La kurtosis de los datos es ahora totalmente compatible por lo que la anomalía quedaría explicada de esta manera.

7.6 Conclusiones

En esta tesis presentamos la detección de una mancha fría en la RFCM. Hemos aplicado un método basado en ondículas esféricas a los datos de WMAP del primer y tercer año para testar su Gaussianidad. La Gaussianidad es un rasgo clave para discriminar entre distintos modelos cosmológicos. Las coordenadas galácticas de la mancha son $b = -57^\circ, l = 209^\circ$ y su tamaño angular es de unos 10° en el cielo. La probabilidad de encontrar una mancha así en simulaciones Gaussianas es muy baja. Como el test aplicado a los datos era ciego, hubo que realizar un duro trabajo para intentar identificar el origen de la anomalía. Después de descartar el ruido instrumental y los contaminantes galácticos, analizamos un modelo concreto, el de texturas cósmicas. Tras calcular el cociente de probabilidades a posteriori entre el modelo con texturas y el Gaussiano, concluimos que la mancha podría ser la primera detección de un defecto topológico. Por tanto su origen sería debido a una textura colapsando. De confirmarse, este resultado tendría consecuencias importantes, ya que al incluir

texturas en el modelo cosmológico la estimación de los parámetros cosmológicos podría verse afectada. Además la detección de defectos topológicos es de gran importancia para las teorías de física de altas energías y del Universo primitivo. También se han dado otras posibles explicaciones para la mancha como vacíos o cúmulos a través del efecto Sunyaev-Zeldovich. Sin embargo en un trabajo que estamos realizando ahora, estas hipótesis parecen descartarse por la gran escala angular de la mancha que es incompatible con estos dos modelos.

A continuación pasamos a resumir las conclusiones de cada uno de los capítulos de esta tesis:

7.6.1 Capítulo 2

Motivados por la desviación de la Gaussianidad encontrada en los datos del primer año de WMAP usando la SMHW, hemos realizado un análisis de las manchas en los mapas de coeficientes de ondícula. Hemos detectado una mancha extremadamente fría y grande a escalas de $\approx 4^\circ$ con coordenadas galácticas $b = -57^\circ, l = 209^\circ$. La probabilidad de encontrar tal mancha a una escala concreta en simulaciones Gaussianas es de $\approx$ 0.2%, indicando que si es intrínseca sería incompatible con el modelo estándar ya que éste predice fluctuaciones Gaussianas en la RFCM. Si excluimos la mancha de nuestro análisis, el resto del mapa parece ser compatible con Gaussianidad.

Para determinar el origen de la mancha hemos realizado numerosos tests relacionados con contaminación instrumental o galáctica. Comprobamos que los efectos del ruido instrumental y de la antena son despreciables a las escalas a las que aparece la mancha. Además la detección aparece en todos los detectores del satélite. La mancha parece ser independiente de la frecuencia mientras que los contaminantes galácticos presentan una dependencia frecuencial fuerte. Sin embargo no podemos descartar aún el efecto Sunyaev-Zeldovich producido por cúmulos ya que la dependencia frecuencial de éste es más débil que la de los contaminantes galácticos. Una mancha parecida podría ser originada por un cúmulo parecido al de Coma pero a una distancia más cercana, o bien por varios cúmulos ricos a la distancia a la que se encuentra Coma. Sin embargo hemos comprobado que en la dirección de la mancha no se encuentra ningún cúmulo de galaxias.

Concluimos por tanto que las fluctuaciones intrínsecas no pueden ser descar-

tadas como causantes de la mancha. En concreto una estructura muy masiva y distante podría producir una mancha como la observada a través del efecto Rees-Sciama [119]. Esta estructura debería estar muy alejada ya que sino habría sido observada ya. Otras posibilidades serían defectos topológicos (como monopolos o texturas) o inflación no-estándar. Otra posibilidad sería una suma de una fluctuación Gaussiana de RFCM con el efecto Sunyaev-Zeldovich.

7.6.2 Capítulo 3

En este capítulo hemos analizado en primer lugar la robustez estadística de la desviación de la Gaussianidad en la kurtosis de coeficientes de ondícula. Teniendo en cuenta todos los tests realizados, vemos que solo 0.69% presentan una desviación igual o mayor que los datos en 4 escalas consecutivas de un hemisferio cualquiera.

En segundo lugar hemos estudiado la morfología de la mancha usando ondículas elípticas en la esfera. Observamos que la amplificación máxima en temperatura se obtiene para ondículas casi isótropas, por lo que la forma de la mancha subyacente es casi circular. Este resultado no descarta hipótesis como defectos topológicos (como texturas) o potenciales gravitatorios con forma circular.

Por último nos centramos en la posible contaminación Galáctica o de efecto Sunyaev-Zeldovich en la región de la mancha observada. Vemos que el efecto Sunyaev-Zeldovich por si sólo es incompatible con la dependencia frecuencial plana que presenta la mancha. Una combinación de contaminantes galácticos podría dar lugar a una contribución independiente de la frecuencia, por lo que analizamos este caso con más detalle.

En el espacio de coeficientes de ondícula, la contribución de los contaminantes galácticos es extremadamente baja en las bandas Q, V y W. La que más contribuye es la emisión free-free excepto en la banda W donde está al mismo nivel que el polvo aunque por debajo del ruido instrumental.

El hecho de que la kurtosis y el área sean iguales en la banda Q, donde la contaminación residual es más alta que en la V y W, indica que los contaminantes no juegan un papel importante en el origen de la mancha.

Además obtenemos resultados independientes de la técnica utilizada para substraer la contaminación e incluso sobreestimando la contaminación residual es

altamente improbable llegar a explicar la mancha con emisión Galáctica.

7.6.3 Capítulo 4

En este capítulo hemos repetido los análisis realizados con los datos del primer año de WMAP para los datos del tercer año, recientemente publicados. Varios trabajos anteriores [188], [43], [32] y [44] detectaron una mancha no Gaussiana usando distintos estimadores como la kurtosis, el área, *Max* y HC, siempre basados en ondículas en la esfera. Aquí confirmamos la detección aplicando todos estos estimadores a los datos del tercer año de WMAP. La nueva técnica utilizada para restar la contaminación galáctica hace que la significación de la detección sea aún mayor.

Para evitar cualquier consideración *a posteriori* aplicamos un nuevo test para calcular la probabilidad de que la desviación sea debida a una fluctuación estadística del modelo Gaussiano. El valor que obtenemos para dicha probabilidad es 1.85%. Además, la mancha es aún menos dependiente de la frecuencia descartando así la contaminación galáctica como posible explicación. Vemos que el ruido instrumental también es prácticamente despreciable para nuestro análisis. En el siguiente capítulo analizaremos más en detalle el posible origen de la mancha basándonos en un modelo de defectos topológicos.

7.6.4 Capítulo 5

Hemos investigado la posibilidad de que la mancha sea debida a una textura cósmica, encontrando que la escala, amplitud y el número de manchas esperadas son consistentes con esta interpretación.

Usando una aproximación analítica del perfil de temperatura generado por una textura, realizamos un test de hipótesis bayesiano. Calculamos el cociente de probabilidad a posteriori entre el modelo con y sin textura siendo el resultado favorable a la existencia de una textura centrada en $b = -57^\circ, l = 209^\circ$.

Para testar el modelo de texturas a todo el cielo hemos simulado texturas con el perfil analítico y la distribución de escalas teórica. Comprobamos que la kurtosis de los datos que resultaba ser incompatible con las simulaciones Gaussianas, ahora es consistente con las simulaciones con texturas. Además las manchas más pequeñas que se han añadido no introducen nuevas incompatibilidades

con los datos.

Si la mancha es debida a una textura, podemos inferir que la escala de ruptura de simetría es $\phi_0 \approx 8.7 \times 10^{15} GeV$, que es del orden de las predicciones de las teorías unificadas. El redshift al que se encontraría la textura es $z \approx 6$ dentro de los límites de los más profundos muestreos de galaxias.

Futuras observaciones pueden confirmar o refutar esta hipótesis. En primer lugar las texturas apenas producen polarización en la RFCM mientras que si la mancha es debida a una fluctuación Gaussiana, debería verse un patrón radial de polarización. A estas escalas alrededor del 50% de la polarización está correlacionada con la temperatura. Además el modelo de texturas predice muchas manchas pequeñas que no detectamos posiblemente por estar mezcladas con las manchas Gaussianas que alcanzan su potencia angular máxima alrededor de $1^\circ - 2^\circ$. Sin embargo medidas precisas de la polarización a estas escalas podrían revelar una desviación respecto a las predicciones para la correlación entre temperatura y polarización, confirmando la existencia de texturas.

Por otra parte el modelo analítico utilizado aquí es una aproximación por lo que sería deseable realizar un estudio a todo el cielo con simulaciones de texturas a alta resolución para comprobar nuestros resultados.

7.7 Trabajo futuro

Para comprobar la posible detección de una textura hemos de realizar varias pruebas. Utilizando simulaciones de texturas a alta resolución podremos contrastar de manera más exacta la desviación de la Gaussianidad medida en los datos. Además un análisis bayesiano a todo el cielo puede determinar mejor el cociente de probabilidades a posteriori. También un estudio de la polarización puede confirmar o rechazar la detección de la textura.

Estamos trabajando en comparar la hipótesis de la textura con otras como grandes vacíos o el efecto Sunyaev-Zeldovich. Estas alternativas parecen ser menos probables debido al gran tamaño angular de *la mancha*.

El patrón de anisotropías predicho por un modelo de Bianchi que fue detectado en los datos de WMAP [25] también está relacionado con *la mancha*, como discutimos en los capítulos 3 y 4. Otro trabajo a realizar es el estudio de la relación entre *la mancha* y dicho patrón.

References

[1] Abell, G. O., Corwin, H. G. Jr., Olowin, R. P., 1989, ApJS, 70, 1.

[2] Adler R. J., Bjorken J. D., Overduin J. M., 2006, gr-qc/0602102.

[3] Aliaga A.M., Martínez-González E., Cayón L., Argüeso F., Sanz J.L. & Barreiro R.B., 2003, New Astron. Rev., 47, 821.

[4] Aghanim N., Kunz M., Castro P. G. & Forni O., 2003, A&A, 406, 797.

[5] Alpher R.A., Bethe H.A., Gamow G., 1948, Physics Review, 73: 803 - 804.

[6] Antoine J. P. & Vandergheynst, P., 1998, J. Math Phys., 39, 3987.

[7] Baccigalupi C., Bedini L., Burigana C., De Zotti G., Farusi A., Maino D., Maris M., Perrotta F., Salerno E., Toffolatti L., Tonazzini A., 2000, MNRAS, 318, 769.

[8] Banday A.J., Zaroubi S. & Gorski K.M., 2000, ApJ, 533, 575-587.

[9] Bardeen J.M., Steinhardt P.J., Turner M.S., 1983. Phys. Rev. D. 28, 679-693.

[10] Barreiro R. B., Hobson M. P., Lasenby A. N., Banday A. J., Górski K. M. & Hinshaw G., 2000, MNRAS, 318, 475.

[11] Barreiro R. B. & Hobson M. P., 2001, MNRAS, 327, 813.

[12] Barreiro R.B., Hobson M.P., Banday A.J., Lasenby A.N., Stolyarov V., Vielva P., Górski K.M., 2004, MNRAS, 351, 515.

[13] Bartolo N., Komatsu E., Matarrese S. & Riotto A., 2004, Phys.Rep., 402, 103.

[14] Barrow J.D., Juszkiewicz R. & Sonoda D.H., 1985, MNRAS, 213, 917.

[15] Bennett D.P., Rhie S-H.,1993, Astrophys.J. 406, L7.

[16] Bennett C.L., et al., 1996, ApJ, 464, L1.

[17] Bennett C.L., et al., 2003, ApJS, 148, 1.

[18] Bennett C.L., et al., 2003, ApJS, 148, 97.

[19] Benoît A., 2003, A & A, 399, 19.

[20] Bernardi G., Carretti E., Fabbri R., Sbarra C., Poppi S., Cortiglioni S., Jonas J.L., 2004, MNRAS, 351, 436.

[21] Bevis N., Hindmarsh M., Kunz M., 2004, Phys. Rev. D70, 043508.

[22] Bielewicz P., Eriksen H.K., Banday A.J., Gòrski K.M. & Lilje P.B., 2005, ApJ, 635, 750.

[23] Bonaldi A., Bedini L., Salerno E., Baccigalupi C., de Zotti G., 2006, MNRAS, 373, 273.

[24] Bouchet, F. R., Prunet, S., Sethi, S. K., 1999, MNRAS, 302, 663.

[25] Bridges M., McEwen J. D, Lasenby A. N., Hobson M. P., 2007, MNRAS, 377, 1473.

[26] Bromley B.C. & Tegmark M., 1999, ApJ, 524, L79-L82.

[27] Cabella P., Liguori M., Hansen F.K., Marinucci D., Matarrese S., Moscardini L. & Vittorio N., 2005, MNRAS, 358, 684.

[28] Cayón L., Sanz J.L., Barreiro R.B., Martínez-González E., Vielva P., Toffolatti L., Silk J., Diego J.M., Argüeso F., 2000, MNRAS, 315, 757, 761.

[29] Cayón L., Sanz J.L., Martínez-González E., Banday A.J., Argüeso F., Gallegos J.E., Gorski K.M. & Hinshaw G., 2001, MNRAS, 326, 1243.

[30] Cayón L., Argüeso F., Martínez-González E. & Sanz, 2003, MNRAS, 344, 917.

[31] Cayón L., Martínez-González E., Argüeso F., Banday A.J., Gorski K.M., 2003, MNRAS, 339, 1189.

[32] Cayón L., Jin L. & Treaster A., 2005, MNRAS, 362, 826.

[33] Cayón L., Banday A. J., Jaffe T., Eriksen H. K., Hansen F.K., Gorski K. M., Jin J., 2005, MNRAS, 369, 598.

[34] Chiang L.Y., Naselsky P.D., Verkhodanov O.V. & Way M.J., 2003, ApJ, 590, 65.

[35] Chiang L.Y., Naselsky P.D., 2006, IJMP D, 15, 1283-1298.

[36] Chiang L-Y, Naselsky P.D., Coles P., 2007, ApJ, 664, 8.

[37] Coles P., Dineen P., Earl J. & Wright D., 2004, MNRAS, 350, 989.

[38] Coles P., 2005, Nature 433, 248.

[39] Copi C.J., Huterer D. & Starkman G.D., 2004, Phys. Rev. D, 70, 043515.

[40] Copi C. J., Huterer D., Schwarz D. J., Starkman G. D., 2006, MNRAS, 367, 79.

[41] Copi C. J., Huterer D., Schwarz D. J., Starkman G. D., 2007, Phys. Rev D, 75, 023507.

[42] Crittenden R. G., Coulson D., Turok N., 1995, Phys. Rev., D52 5402.

[43] Cruz M., Martínez-González E., Vielva P. & Cayón L., 2005, MNRAS, 356, 29.

[44] Cruz M., Tucci M., Martínez-González E. & Vielva P., 2006, MNRAS, 369, 57.

[45] Cruz M., Cayón L., Martínez-González E., Vielva P. & Jin J., 2007, ApJ, 655, 11.

[46] Cruz M., Turok N. G., Vielva P., Martínez-González E. & Hobson M. P., 2007, to be submitted.

[47] Curto A., Aumont J., Macias-Perez J.F., Martínez-González E., Barreiro R.B., Santos D., Desert F.X., 2006, accepted in A&A.

[48] de Bernardis P., et al., 2000, Nature, 404, 955

[49] de Oliveira-Costa A., Tegmark M., Davies R.D., Gutiérrez C.M., Lasenby A.N., Rebolo R. & Watson R.A., 2004, ApJ, 606, 89.

[50] de Oliveira-Costa A., Tegmark M., Zaldarriaga M. & Hamilton A., 2004, Phys. Rev. D, 69, 063516.

[51] de Oliveira-Costa A., Tegmark M., 2006, Phys. Rev. D, 74, 023005.

[52] Delabrouille J., Cardoso J.-F., Patanchon G., 2003, MNRAS, 346, 1089.

[53] Dicke R. H., Peebles, P. J. E., Roll P. G., Wilkinson D. T., 1965, ApJ, 142, 414.

[54] Dickinson C., Davies R.D., Davis R.J., 2003, MNRAS, 341, 369.

[55] Diego J.M., Martínez-González E., Sanz J.L., Mollerach S. & Martínez V.J., 1999, MNRAS, 306, 427.

[56] Dineen P., Coles P., 2005, submitted to MNRAS (astro-ph/0511802).

[57] Donoho D., Jin J., 2004, Ann. Statist., 32, 962.

[58] Draine B.T., Lazarian A., 1999, ASPC, 181, 133.

[59] Durrer R., 1999, New Astron. Rev., 43, 111.

[60] Durrer R., Kunz M., Melchiorri A., 1999, Phys. Rev. D, 59, 123005.

[61] Eriksen H. K., Hansen F. K., Banday A. J., Górski K. M. & Lilje P. B., 2004, ApJ, 605, 14.

[62] Eriksen H. K., Banday A.J., Górski K.M., Lilje P.B, 2004, ApJ, 605, 14.

[63] Eriksen H.K., Novikov D.I., Lilje P.B., Banday A.J. & Górski K.M., 2004, ApJ, 612, 64.

[64] Eriksen H. K., Banday A. J., Górski K. M., Lilje P. B., 2005, ApJ, 622, 58.

[65] Eriksen H. K., Banday A. J., Górski K. M., Hansen F. K., Lilje P. B., 2007, ApJL, 660, L81.

[66] Ferreira G.F., Magueijo J. & Górski K.M., 1998, ApJ, 503, 1.

[67] Finkbeiner D.P., Davis M., Schlegel D.J., 1999, ApJ, 524, 867.

[68] Finkbeiner D.P., 2003, ApJS, 146, 407.

[69] Freeman P. E., Genovese C. R., Miller C. J., Nichol R. C., Wasserman L., 2006, ApJ, 638, 1.

[70] González-Nuevo J., Argüeso F., López-Caniego M., Toffolatti L., Sanz J.L., Vielva P., Herranz D., 2006, MNRAS, 369, 1603.

[71] Grainge K., et al., 2003, MNRAS, 341, 23.

[72] Gruzinov, A. & Hu, W. 1998, ApJ, 508, 435.

[73] Górski K.M., Hivon E., Banday A.J., Wandelt B.D., Hansen F.K., Reinecke M., Bartelman M., 2005, ApJ, 622, 759.

[74] Guth A.H., Pi S-Y, 1985, Phys.Rev.D, 32, 1899.

[75] Haar A., 1910 Mathematische Annalen, 69, 331.

[76] Hajian A. & Souradeep T., 2003, ApJ, 597, 5.

[77] Hajian A., Souradeep T. & Cornish N., 2005, ApJ, 618, 63.

[78] Halverson N.W. et al., 2002, ApJ, 568, 38

[79] Hanany, S., et al., 2000, ApJ, 545, L5

[80] Hansen F.K., Cabella P., Marinucci D. & Vittorio N., 2004, ApJ, 607, 67.

[81] Hansen F.K., Banday A.J. , Górski K.M., 2004, MNRAS, 354, 641.

[82] Hansen F. K., Branchini E., Mazzotta P., Cabella P., Dolag K., 2005, MNRAS, 361, 753.

[83] Hansen F. K., Banday A. J., Eriksen H. K., Górski K. M., Lilje P. B., 2006, ApJ, 648, 784.

[84] Haslam C.G.T., Stoffel H., Salter C.J., Wilson W.E., 1982, A&AS, 47, 1.

[85] Harrison E.R., 1970, Phys. Rev., D1, 2726 1.

[86] Heavens A.F., 1998, MNRAS, 299, 805-808.

[87] Herranz D., Sanz J.L., Hobson M.P., Barreiro R.B., Diego J.M., Martínez-González E., Lasenby A.N., 2002, MNRAS, 336, 1057.

[88] Herranz D., Sanz J.L., Barreiro R.B., Martínez-González E., 2002, ApJ, 580, 610.

[89] Herranz D., Sanz J. L., Barreiro R. B., LÃşpez-Caniego M., 2005, MNRAS, 356, 944.

[90] Hinshaw G., et.al., 2007, ApJS, 170, 288.

[91] Hobson M.P., Jones A.W., Lasenby A.N., Bouchet F.R., 1998, 1998, MNRAS, 300, 1.

[92] Hobson M.P., Jones A.W. & Lasenby A.N., 1999, MNRAS, 309, 125.

[93] Hobson M.P., McLachlan C., 2003, MNRAS, 338, 765.

[94] Hubble E., 1929, PNAS, 15, 168.

[95] Inoue K. T., Silk J., 2006, ApJ, 648, 23.

[96] Inoue K. T., Silk J., 2007, ApJ accepted.

[97] Jaffe T. R., Banday A. J., Eriksen H. K., Górski K. M., Hansen F. K., 2005, ApJ, 629, 1.

[98] Jaffe T. R., Hervik S., Banday A. J., Górski K. M., 2006, ApJ 644, 701.

[99] Jonas J.L., Baart E.E. & Nicolson G.D., 1998, MNRAS, 297, 977.

[100] Joyce M., Turok N., 1994, Nucl. Phys. B416, 389.

[101] Kibble T.W.B., 1976, J. Phys., A9, 1387.

[102] Kogut A., Banday A.J., Bennett C.L., Górski K.M, Hinshaw G., Smoot G.F. & Wright E.L. 1996, ApJ, 464, 29.

[103] Komatsu E., et al., 2003, ApJ, 148, 119.

[104] Kovac J. M., Leitch E. M., Pryke C., Carlstrom J. E., Halverson N. W., Holzapfel W. L., 2002, Nature, 420, 722.

[105] Kunz M., Banday A.J., Castro P.G., Ferreira P.G. & Gorski K.M., 2001, ApJ, 563, 99.

[106] Kuo C.L. et al., 2002, AAS, 200, 0603.

[107] Lachièze-Rey, M. & Luminet, J.-P. 1995, Phys. Rep., 254, 135.

[108] Land K. & Magueijo J., 2005, Phys. Rev. Lett., 95, 071301.

[109] Land K. & Magueijo J., 2005, MNRAS, 367, 1714.

[110] Land K. & Magueijo J., 2005, MNRAS, 357, 994.

[111] Land K. & Magueijo J., 2007, MNRAS accepted.

[112] Larson D.L. & Wandelt B.D., 2004, ApJ, 613, 85.

[113] Larson D.L. & Wandelt B.D., 2005, Phys. Rev. D, submitted, astro-ph/0505046.

[114] Liddle A.R. & Lyth D.H., 2000, *Cosmological Inflation and Large-Scale Structure*, Cambridge University Press

[115] Liu X., Zhang S.N., 2005, ApJ, 633, 542.

[116] López-Caniego M., González-Nuevo J.,Herranz D., Massardi M., Sanz J.L., De Zotti G., Toffolatti L., Argüeso F., 2007, ApJS, 170, 108.

[117] Magueijo J., 1995, Phys. Rev. D, 52, 689.

[118] Maino D., Banday A. J., Baccigalupi C., Perrotta F., Górski K. M., 2003, MNRAS, 344, 544.

[119] Martínez-González E., Sanz J.L., 1990, MNRAS, 247, 473.

[120] Martínez–González E., Sanz J. L. & Silk J., 1990, MNRAS, 247, 473.

[121] Martínez-González E., Sanz J.L. & Cayón L., 1997, ApJ, 484, 1.

[122] Martínez-González E., Gallegos J.E., Argüeso F., Cayón L., Sanz J.L., 2002, MNRAS, 336, 22.

[123] Martínez-González E., Diego J. M., Vielva P., Silk J., 2003, MNRAS, 345, 1101.

[124] Martínez-González E., 2006, proceedings of the Valencia Summer School "Data Analysis in Cosmology", astro-ph/0610162.

[125] Mather J.C. et al., 1994, ApJ, 420, 439.

[126] McEwen J. D., Hobson M. P., Lasenby A. N., Mortlock D. J., 2005, MNRAS, 359, 1583.

[127] McEwen J. D., Hobson M. P., Lasenby A. N., Mortlock D. J., 2005, IEEE Trans.Signal Process. 55 (2007) 520-529.

[128] McEwen J. D., Hobson M. P., Lasenby A. N., Mortlock D. J., 2006, MNRAS, 371, 50.

[129] McEwen J. D., Hobson M. P., Lasenby A. N., Mortlock D. J., 2006, MNRAS, 369, 1858.

[130] McEwen J.D., Vielva P., Hobson M.P., Martínez-González E. & Lasenby A.N., 2007, MNRAS, 376, 1211.

[131] Mollerach S., Martínez V.J., Diego J.M., Martínez-González E., Sanz J.L. & Paredes S., 1999, ApJ, 525, 17.

[132] Monteserín C., Barreiro R.B., Sanz J.L. & Martínez-González E., 2005, MNRAS, 360, 9.

[133] Moudden Y., Cardoso J. -F., Starck J. -L., Delabrouille J., 2004, astro-ph/0407053.

[134] Mukherjee P. & Wang Y., 2004, ApJ, 613, 51.

[135] Naselsky P.D., Doroshkevich A.G. & Verkhodanov O.V., 2003, ApJ, 599, 53.

[136] Naselsky P., Chiang L.-Y., Olesen P. & Novikov I., 2005, Phys. Rev. D, 72, 063512.

[137] Novikov D., Schmalzing J. & Mukhanov V.F., 2000, A& A, 364, 17-25.

[138] Page et al. 2007, ApJS, 170, 335.

[139] Pando J., Valls-Gabaud D. & Fang L. -Z., 1998, Phys. Rev. Lett., 81, 4568.

[140] Patanchon G., Cardoso J.-F., Delabrouille J., Vielva P., 2005, MNRAS, 364, 1185.

[141] Park C.-G., Park C., Ratra B. & Tegmark M., 2001, ApJ, 556, 852.

[142] Park C.-G., 2004, MNRAS, 349, 313.

[143] Peebles P.J.E., Yu J. T., 1970, ApJ, 162, 815.

[144] Pen U. & Spergel D. N., Turok N., 1994, Phys. Rev. D, 49, 692.

[145] Penzias A.A. & Wilson R.W., 1965, ApJ, 142, 41.

[146] Phillips N.G. & Kogut A., 2001, ApJ, 548, 540-549.

[147] Piacentini et al. 2007, NewAR, 51, 244.

[148] Polenta G., et al., 2002, ApJ, 572, 27.

[149] Rees M.J., Sciama D.W., 1968, Nature, 217, 511.

[150] Rubiño-Martín et al., 2006, MNRAS, 369, 909.

[151] Sachs, R.K. & Wolfe, A.M., 1967, ApJ, 147, 73.

[152] Santos M.G. et al., 2002, Phys. Rev. Lett., 88, 241302.

[153] Sanz J. L., Argüeso F., Cayón L., Martínez–González E., Barreiro R. B. & Toffolatti L., 1999a, MNRAS, 309, 672.

[154] Sanz J. L., Barreiro R. B., Cayón L., Martínez–González E., Ruiz G. A., Díaz F. J., Argüeso F., Silk J. & Toffolatti L., 1999b, A&AS, 140, 99.

[155] Sanz J. L., Herranz D., Martínez–González E., 2001, ApJ, 552, 484.

[156] Savage R. et al., 2004, MNRAS, 349, 973.

[157] Schlegel D.J., Finkbeiner D.P., Davis M., 1998, ApJ, 500, 525.

[158] Schmalzing J. & Gorski K.M., 1998, MNRAS, 297, 355.

[159] Schwarz D.J., Starkman, G.D., Huterer D. & Copi C.J., 2004, Phys. Rev. Lett., 93, 1301.

[160] Seljak U., 1996, ApJ, 463, 1.

[161] Seljak U. & Zaldarriaga M., 1996, ApJ, 469, 437.

[162] Shandarin S.F., Feldman H.A., Xu Y. & Tegmark M., 2002, ApJS, 141,1.

[163] Sievers J.L., et al., 2001, AAS, 199, 3402

[164] Silk J., 1968, ApJ, 151, 459.

[165] Slosar A. & Seljak U., 2004, Phys. Rev. D, 70, 083002.

[166] Smith S. et al., 2004, MNRAS, 352, 887.

[167] Smoot, G.F. et al., 1992, ApJ, 396: L1-L5.

[168] Snowden S. L., Egger R., Freyberg M. J., McCammon D., Plucinsky P. , Sanders W. T., Schmitt J. H. M. M., Truemper J., Voges W., 1997, ApJ, 485, 125.

[169] Spergel D. N., Turok N. G., Press, William H., Ryden B. S., 1991, Phys. Rev. D, 43, 1038.

[170] Spergel D. N. et al., 2003, ApJS, 148, 175

[171] Spergel D.N. et al., 2007, ApJS, 170, 377.

[172] Stolyarov V., Hobson M. P. , Ashdown M. A. J., Lasenby A., 2002, MNRAS, 336, 97.

[173] Sunyaev R.A., Zeldovich Y.B., 1970, ASS, 7, 3.

[174] Sunyaev R.A., Zeldovich Y.B., 1972, CoASP, 4, 173.

[175] Taylor, J.E., Moodley, K, Diego, J.M., 2003, MNRAS, 345, 1127.

[176] Tegmark, M., Efstathiou, G., 1996, MNRAS, 281, 1297.

[177] Tegmark, M., de Oliveira-Costa, A., 1998, ApJ, 500, 83.

[178] Tegmark M., de Oliveira-Costa A., Hamilton A., 2003, Phys.Rev. D68, 123523.

[179] Tenorio L., Jaffe A.H., Hanany S., Lineweaver C.H., 1999, MNRAS, 310, 823.

[180] Tojeiro R., Castro P.G., Heavens A.F., Gupta S., 2006, MNRAS, 365, 265.

[181] Tomita K., 2005, Phys. Rev. D, 72, 10.

[182] Turok N., 1989, Phys. Rev. Letters, 63, 2625.

[183] Turok N. & Spergel D. N., 1990, Phys. Rev. Letters, 64, 2736.

[184] Turok N., 1996, Phys. Rev. Lett. 76, 1015.

[185] Vielva P., Martínez–González E., Cayón L., Diego J. M., Sanz J. L. & Toffolatti L., 2001a, MNRAS, 326, 181.

[186] Vielva P., Barreiro R. B., Hobson M. P., Martínez–González E., Lasenby A. N., Sanz J. L. & Toffolatti L., 2001b, MNRAS, 328, 1.

[187] Vielva P., Martínez–González E., Gallegos J. E., Toffolatti L. & Sanz J. L., 2003, MNRAS, 344, 89.

[188] Vielva P., Martínez-González E., Barreiro R.B., Sanz J.L. & Cayón L., 2004, ApJ, 609, 22.

[189] Vielva P., Martínez-González E. & Tucci M., 2006, MNRAS, 365, 891.

[190] Vielva P., Wiaux Y., Martínez-González E., Vandergheynst P., 2007, submitted to MNRAS, astro-ph/0704.3736.

[191] Vilenkin A. & Shellard E.P.S., 1994, *Cosmic Strings and Other Topological Defects*, Cambridge University Press.

[192] Watson R.A., Rebolo R., Rubiño-Martín J.A., Hildebrant S., Gutiérrez C.M., Fernández-Cerezo S., Hoyland R.J. & Battistelli E.S., 2005, ApJ, 624, L89.

[193] Wiaux Y., Vielva P., Martínez-González E. & Vandergheynst P., 2006, Phys. Rev. Lett., 96, 151303.

[194] Wu J.H.P., Balbi A., Borrill J., Ferreira P.G., Hanany S., Jaffe A.H., Lee A.T., Rabii B., Richards P.L., Smoot G.F., Stompor R. & Winant C.D., 2001, Phys. Rev. Lett., 87, 1303.

[195] Zel'dovich Y.B., 1972, MNRAS, 160, 1.